

Susanne Klungland Stokkevåg

# Oxidation of Methanol to Formaldehyde (MTF) over Silver Catalyst

Master's thesis in Industrial Chemistry and Biotechnology

Supervisor: Hilde Johnsen Venvik

June 2020

NTNU  
Norwegian University of Science and Technology  
Faculty of Natural Sciences  
Department of Chemical Engineering



Norwegian University of  
Science and Technology



Susanne Klungland Stokkevåg

# **Oxidation of Methanol to Formaldehyde (MTF) over Silver Catalyst**

Master's thesis in Industrial Chemistry and Biotechnology  
Supervisor: Hilde Johnsen Venvik  
June 2020

Norwegian University of Science and Technology  
Faculty of Natural Sciences  
Department of Chemical Engineering







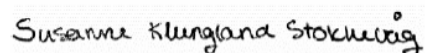
## Preface

This thesis is a cumulation of my master's degree in chemical engineering at NTNU in Trondheim, Norway. The work presented in this thesis was performed at NTNU from January to June 2020, and some results are from the specialization project from the fall of 2019.

First of all, I would like to thank my supervisor, Hilde Johnsen Venvik, for your guidance and helpful advices thought the project. I would also like to thank my co-supervisors; Rune Lø-deng, at SINTEF, and Jia Yang, at NTNU, for all your help with this thesis. A special thank you goes to co-supervisor and Ph.D. student Stine Lervold for your helpful advices and guidance for both lab work and writing, whenever needed. I would also like to thank the people in the catalysis department for their help and training.

## Declaration of compliance

I declare that this is an independent work according to the exam regulations at the Norwegian University of Science and Technology.



Susanne Klungland Stokkevåg

Trondheim, Norway  
June 26, 2020

## Abstract

The work performed in this thesis had a goal to contribute to the understanding of the methanol to formaldehyde reaction, and the silver interactions in these conditions. Silver particles, net and annular were treated in different conditions, and characterized in XRD, EBSD and SEM. The annular silver were also used as a catalyst in methanol oxidation experiments, with a goal of investigating external mass transfer limitations.

Silver particles and net were calcined in air at 650 °C, which resulted in surface restructuring by formation of a smoothed surface with facets. On the particles, pinholes were also formed and they were observed to increase with increasing time on stream. These pinholes were not observed on the silver net. The extensive restructuring were not seen on particles calcined in hydrogen, nitrogen or methanol and water, and suggest that atomic oxygen is required for activating the silver surface for extensive restructuring. The crystallite sizes were measured through XRD, and showed that there is almost no change when the particles are exposed to these conditions, and TEM showed that the unused particles are single crystals. For the net, the crystallite size does however increase when calcined in air. This indicates structural differences where the silver bulk of the net is easier affected by the conditions.

The extensive restructuring, with pinhole formation, were also seen on silver used in the MTF reaction. The difference in size for annular silver were also small, indicating high mechanical stability. Two methanol oxidation experiments diluted in helium were further performed over annular silver, and compared to an identical experiment in nitrogen. The conversions for all three experiments deviated from each other, which could indicate that there are external mass transfer limitation in the system. Because of the different results of the two helium experiment, another reaction should be performed to determine this. Highly corrugated surfaces with protrusions were observed, where the amount increased with increasing temperature. An attempt to develop a pretreatment approach of silver for EBSD was also conducted on unused particles and annular silver. TDue to the corona situation, the approach was not optimized.

## Sammendrag

Arbeidet som er utført i denne master oppgaven hadde som mål å bidra til forståelsen av metanol til formaldehyd reaksjonen, og sølv interaksjonene i disse forholdene. Sølvpartikler, nett og annulær ble behandlet i ulike forhold, og karakterisert i XRD, EBSD og SEM. Det annulære sølvet ble også brukt som katalysator i metanol oksidasjons eksperiment, med et mål om å undersøke for eksterne masseoverføringsbegrensninger.

Sølvpartiklene og nettet ble kalsinert i luft ved 650 °C, som resulterte i dannelse av en glatt overflate med fasetter. På partiklene ble også huldannelse observert, og antall hull ble observert til å øke med økende eksponeringstid. Disse hullene ble ikke observert på overflaten til nettet. Denne omfattende restruktureringen ble ikke observert på partikler som ble kalsinert i hydrogen, nitrogen eller metanol og vann, som foreslår at atomisk oksygen er nødvendig for å aktivere sølvoverflaten for omfattende restrukturering. Krystalitt størrelsene ble estimert gjennom XRD, og viste at det nesten ikke er noen endringer for partiklene når de er eksponert i disse forholdene. TEM viste også at partiklene er enkrystaller. Krystalitt størrelsen til nettet ble derimot endret ved eksponering i luft. Dette indikerer at bulken til nettet blir lettere påvirket av forholdene.

Den omfattende restruktureringen, med huldannelse, ble også observert på sølv brukt i MTF reaksjonen. Forkjellen i krystalittstørrelse for annulærsølv var også liten, som indikerer høy mekanisk stabilitet. To metanol oksidasjons eksperiment, over annulærsølv, ble utført i helium og sammenlignet med et identisk eksperiment i nitrogen. Omsetningene avviket for alle tre eksperimentene, som kan indikere at det er eksterne masseoverføringsbegrensninger i systemet. På grunn av de ulike resultatene fra de to helium forsøkene, burde det derimot utføres enda et eksperiment i helium for å fastslå dette. Ekstensive restrukturering ble også observert på disse prøvene, og restrukturering ble videre observert til å øke med økende temperatur. Et forsøk på å utvikle en metode for prøvepreparering av sølv til EBSD ble utført på partiklene og annulærsølv. På grunn av corona situasjonen ble metoden ble derimot ikke optimalisert.

# Contents

<b>1. Introduction</b>	<b>1</b>
<b>2. Theory</b>	<b>2</b>
2.1. Formaldehyde Production . . . . .	2
2.2. Silver Catalyst . . . . .	4
2.2.1. Silver and Oxygen Interactions . . . . .	6
2.2.2. Catalytic Activity . . . . .	7
2.3. Mass Transfer . . . . .	8
2.4. Catalyst Characterization . . . . .	9
2.4.1. X-Ray Diffraction . . . . .	9
2.4.2. Scanning Electron Microscopy . . . . .	14
2.4.3. Electron Backscatter Diffraction . . . . .	14
2.5. Analytical Techniques . . . . .	15
2.5.1. Light Microscope . . . . .	15
2.5.2. Gas Chromatography [29] . . . . .	15
2.6. Catalytic Activity [30] . . . . .	16
<b>3. Experimental Section</b>	<b>18</b>
3.1. Health, Environment and Safety . . . . .	18
3.2. Experimental Set-ups . . . . .	18
3.2.1. Calcination Set-up . . . . .	19
3.2.2. Methanol to Formaldehyde Set-up . . . . .	19
3.3. Experiments . . . . .	21
3.3.1. Calcination . . . . .	21
3.3.2. Methanol Oxidation . . . . .	21
3.4. Analytical Equipment and Characterization Techniques . . . . .	22
3.4.1. X-Ray Diffraction . . . . .	22
3.4.2. Scanning Electron Microscopy . . . . .	24
3.4.3. Electron Backscatter Diffraction . . . . .	24
3.4.4. Gas Chromatography . . . . .	25
3.5. Calculations . . . . .	26
<b>4. Results and Discussion</b>	<b>27</b>
4.1. Catalyst Characterization . . . . .	27
4.1.1. Unused Catalyst . . . . .	27
4.1.2. Oxygen Interactions . . . . .	37
4.1.3. Hydrogen, Nitrogen and Methanol/Water Interactions . . . . .	41
4.1.4. Methanol Oxidation . . . . .	44
4.2. Catalytic Activity . . . . .	51
<b>5. Conclusion</b>	<b>58</b>
<b>Appendices</b>	<b>I</b>

A. Reactor Details	I
B. X-Ray Diffraction	II
C. Scanning Electron Microscopy	V
D. Activity Calculations	IX
E. Risk Assessment	XII

## Abbreviations

CEM= Controlled Evaporation and Mixing

CO= Carbon Monoxide

EBSD= Electron Backscatter Diffraction

FCC= Face Centered Cubic

FDS= Fixed Divergence Slit

GC= Gas Chromatography

GLC= Gas Liquid Chromatography

GSC= Gas Solid Chromatography

H<sub>2</sub>= Hydrogen

H<sub>2</sub>O= Water

LGV = Linear Gas velocity

LPSD= Linear Position Sensitive Detector

MeOH= Methanol

MTF= Methanol to Formaldehyde

N<sub>2</sub>= Nitrogen

NTNU= Norwegian University of Science and Technology

PSD= Position Sensitive Detector

SEM= Scanning Electron Microscopy

TOF= Turnover Frequency

TOS= Time on Stream

XRD= X-Ray Diffraction

## List of Figures

2.1. Illustration of the commercial methanol to formaldehyde process [4]. . . . .	3
2.2. Illustration of a heterogeneous catalyst surface with defects [8]. . . . .	4
2.3. Face-centered cubic low index planes: (a)-fcc(100), (b)-fcc(111), (c)-fcc(100) [9].	5
2.4. Reaction scheme for the formation of the different oxygen species [10]. . . . .	6
2.5. Constructive diffraction of X-rays, where the direction is given by Bragg's law [19].	9
3.1. Image of the three different silver catalysts that were used in the experiments. From the left: Particles, a quarter of the silver net and annular silver that has been cut to fit the reactor. . . . .	19
3.2. Images of the calcination set-up (a) and MTF set-up (b), including the gas chroma- tograph (left) and the computer used to control the reaction. . . . .	20
3.3. Correct sample preparation for XRD where soft clay were used to get the correct sample height. . . . .	23
4.1. Comparison of the diffraction patterns of unused particles, net and annular silver.	27
4.2. SEM images of unused silver particles ((a) and (b)), unused silver net ((c) and (d)), and unused annular silver ((e) and (f)), at different magnifications. . . . .	29
4.3. Images of unused silver particles, molded in epoxy, after first (a) and second (b) step of the polishing. . . . .	33
4.4. Light microscope images of annular silver grinded and polished to observe the surface (a) and the bulk (b). . . . .	34
4.5. SEM images of unused particles (a) and annular silver (b), molded in epoxy. . .	35
4.6. Images of Kikuchi bands from the bulk of unused annular silver. . . . .	36
4.7. Diffraction pattern of particles calcined in air, at 650 °C for 5 to 45 h, compared to unused silver particles. . . . .	37
4.8. SEM images of particles calcined in air for 5 h ((a) and (b)) and 45 h ((c) and (d)) at 650 °C, at different magnifications. . . . .	38
4.9. Diffractograms of unused silver net and net calcined in air for 45 h at 650 °C. . .	39
4.10. SEM images of the net after calcined in air for 45 h. at 650 °C. . . . .	40
4.11. Diffractograms of particles calcined in hydrogen (2 % and 100 %) and nitrogen for 19 h, and methanol and water for 24 h, all at 650 °C. . . . .	41
4.12. SEM images of particles calcined for 19 h in hydrogen at low (2 %) ((a) and (b)) and high (100 %) concentration ((c) and (d)), 19 h nitrogen ((e) and (f)), and 24 h in methanol and water ((g) and (h)), at different magnifications. . . . .	42
4.13. X-ray diffractogram of particles used for the MTF reaction in the lab and in the industry. . . . .	44
4.14. SEM images of particles after methanol oxidation ((a) and (b)), with a catalyst bed temperature of 642 °C and TOS of 48 h, and the top ((c) and (d)) and bottom ((e) and (f)) layer of the catalyst bed used for methanol oxidation in the industry.	45
4.15. X-ray diffractogram of used and unused annular silver. . . . .	46
4.16. SEM images of annular silver used for several MTF reactions at temperatures between and TOS from. . . . .	47

4.17. SEM images of annular silver after methanol oxidation in helium. The top images ((a) and (b)) represents the first experiment, and the bottom ((c) and (d)) the second experiment. Both were performed at 600 °C with an initial flow rate of 250 Nml/min. The component flows can be seen in Table 3.3. . . . . .	48
4.18. SEM images of annular silver after methanol oxidation in nitrogen at 540 °C ((a) and (b)), 560 °C ((c) and (d)), 580 °C ((e) and (f)) and 600 °C ((g) and (h)). . . . .	50
4.19. Methanol (a) and oxygen (b) conversion, and formaldehyde (c) and carbon dioxide (d) selectivity for the three methanol oxidation experiments plotted versus TOS. All experiments were performed with an inlet flow of 250 Nml/min at 600 °C and with a TOS of 4 days. Two were diluted in helium, and the last in nitrogen.	52
4.20. Catalyst bed temperature for the three methanol oxidation experiments plotted versus TOS. All experiments were performed with an inlet flow of 250 Nml/min at 600 °C and with a TOS of 4 days. Two were diluted in helium, and the last in nitrogen. . . . .	53
4.21. Conversion and selectivity results for adjustment of total flow and oxygen concentration in feed, for the second helium ((a) and (b)) and the nitrogen ((c) and (d)) experiment. . . . .	55
4.22. Carbon error plotted versus methanol conversion for the three methanol oxidation experiments. . . . .	56
4.23. Catalytic activity for the four annular silver samples used for formaldehyde synthesis in nitrogen. All samples were exposed to a TOS of 96 h and total inlet flow of 250 Nml/min. The temperatures were 540, 560, 580 and 600 °C. . . . .	57
A.1. Details for the reactor employed when performing methanol oxidation experiments in the MTF set-up. . . . .	I
B.1. X-ray diffractogram of unused particles from autumn 2019. . . . .	II
B.2. X-ray diffractogram of particles calcined in air for 5 h, from autumn 2019. . . . .	II
B.3. X-ray diffractogram of particles calcined in air for 5 h by previous student, from autumn 2019. . . . .	III
B.4. X-ray diffractogram of particles calcined in air for 24 h by previous student, from autumn 2019. . . . .	III
B.5. X-ray diffractogram of particles calcined in air for 45 h, from autumn 2019. . . . .	IV
B.6. X-ray diffractogram of particles calcined in hydrogen (2 %) and argon for 19 h, from autumn 2019. . . . .	IV
C.1. SEM images of particles after 5 h calcination in air at 650 °C. . . . .	V
C.2. SEM images of particles after 24 h calcination in air at 650 °C. . . . .	VI
C.3. SEM images of particles after 24 h calcination in air at 650 °C. . . . .	VII
C.4. SEM images of net after 45 h calcination in air at 650 °C. . . . .	VII
C.5. SEM images of annular used in methanol oxidation in nitrogen at 600 °C, TOS of 4 days. . . . .	VIII
D.1. Catalytic activity for the first helium experiment, with changes in linear gas velocity (a) and oxygen concentration in feed (b). . . . .	IX
D.2. Temperature profile through the reactor, measured during experiment. . . . .	X



## List of Tables

3.1. The different purities and sizes of the silver particles, silver net and annular silver, and the companies providing them. . . . .	18
3.2. Conditions for the calcination experiments, including catalyst type. . . . .	21
3.3. Component flows fed to the reactor. The first column is the standard 250 Nml/min feed, the two next columns represents the change in total flow, and the last two the halving and doubling of the oxygen concentration. . . . .	22
3.4. Details of the parameters used in the Rietveld refinement in Topas. Parameters marked with "-" represents inputs, and "+" represents refined parameters. The structural properties were obtained from the databases in Diffrac.Eva and PDF-4+. . . . .	23
3.5. Example of an emission profile added to the Rietveld refinement. The profile is updated regularly, and several were therefore used in the refinements. All the values in the table are inputs. . . . .	24
3.6. Detailed approach for grinding and polishing of silver after molding. The goal was to obtain a flat surface so that EBSD could be conducted. . . . .	25
4.1. Crystallite sizes for both unused silver and silver exposed to varying conditions. The sizes are calculated from both the Scherrer equation (SE) and through Rietveld refinement (RR), and are reported in nm. . . . .	30
4.2. $R_{wp}$ - and GOF-values, from the Rietveld refinement, for the different samples. . . . .	32
D.1. Feed analysis for the first methanol oxidation experiment performed in helium. . . . .	IX
D.2. Feed analysis for the second methanol oxidation experiment performed in helium. . . . .	X
D.3. Feed analysis for the methanol oxidation experiment performed in nitrogen. . . . .	X

# 1. Introduction

Formaldehyde is a reactive chemical with versatile applications. It can be used as building block for various chemicals, and has become important in industrial applications like aviation, automotive and pharmaceuticals [1].

Formaldehyde is produced from methanol, and the first heterogeneously catalyzed synthesis, performed in 1867, was conducted by using a heated platinum spiral [2]. In 1923 a high-pressure synthesis, the BASF process, was developed and allowed industrial production of formaldehyde from methanol. This process used a gauze made from silver wire, which is now mostly replaced by a shallow catalyst bed of silver particles [1]. The process can involve partial oxidation and dehydrogenation with air, steam and excess methanol, in the presence of silver crystals or silver gauze at 600-720 °C, or oxidation with excess air using a modified iron-molybdenum-vanadium oxide catalyst in 250-400 °C [3].

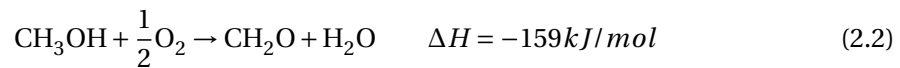
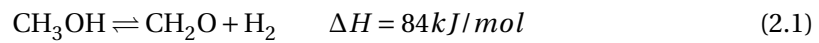
The industrial silver-based methanol to formaldehyde synthesis yields 90-92 % selectivity towards formaldehyde [4]. The understanding of the catalytic system and reactions are essential to be able to improve this, and an important factor to the understanding of silver's catalytic activity, is its interactions with oxygen [2]. This project has focused on the silver-based formaldehyde synthesis and has performed investigations of the interactions between silver and oxygen, hydrogen and nitrogen, as well as performed MTF reactions to investigate for external mass transfer limitation. Three silver catalysts have been studied; particles, net and annular silver, and characterized in XRD and SEM. An attempt to develop a suitable pretreatment approach for EBSD were also performed on the particles and annular silver.

This thesis is an extension of a specialization project that was written in the autumn of 2019. Experiments performed during this semester are also described in this thesis, and their results are used for comparative analyses.

## 2. Theory

### 2.1. Formaldehyde Production

Formaldehyde is the simplest of the aldehydes, and is an important metabolic product in plants and animals. It is formed by photochemical processes of organic material in the atmosphere, or when organic material is incompletely combusted. It is therefore often found in combustion gases from among others, heating plants and automotive vehicles. Formaldehyde is also an important industrial chemical that is used in the manufacture of adhesives, resins and aqueous solutions [1].



The synthesis is mainly based the reactions presented above; dehydrogenation (2.1) and partial oxidation (2.2) of methanol. Formaldehyde production is accounting for about 35 % of the worlds methanol consumption and is thereby one of the largest methanol applications. Industrial production is often performed in a single reactor over a silver-based catalyst, where the endothermic dehydrogenation reaction is supplied by the heat generated from the partial oxidation [4]. Development of the synthesis has resulted in another pathway, using metal oxides from iron, molybdenum and/or vanadium and excess air, which is competing with the silver-based synthesis [1][5].

The industrial process for silver-based formaldehyde production is carried out in adiabatic conditions, at about 890 K and atmospheric pressure. Methanol is vaporized and mixed with air to get a mixture outside the explosion limit. The mixture is further heated to reaction temperature and passed through a shallow catalyst bed. The products are immediately quenched, and after separation in a distillation column, methanol is recycled to the vaporizer [4]. To avoid undesirable reactions, like thermal decomposition of formaldehyde to hydrogen and carbon monoxide, and obtain adiabatic conditions, good temperature control is essential. This is mainly achieved by adding steam to the feed, using excess methanol and regulating the methanol/oxygen ratio [1][4]. Addition of water also removes reaction heat, as a result of its large heat capacity, and thereby prevents sintering [6]. Near complete methanol conversion and 90-92 % selectivity towards formaldehyde is achieved in the industry, which means that 8-10 % of the feedstock is non-selectively oxidized to carbon dioxide and water or carbon dioxide and hydrogen, as seen from Reaction 2.3-2.9 [7]. An illustration of the industrialized process is presented in Figure 2.1.

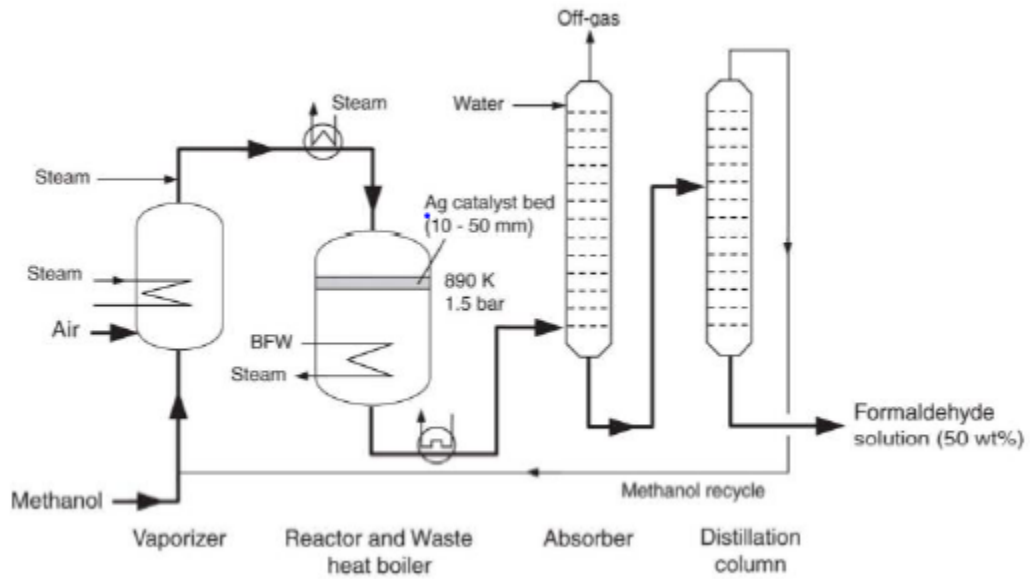
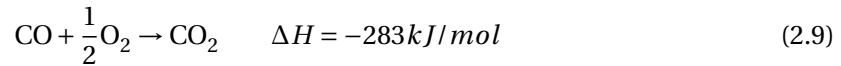
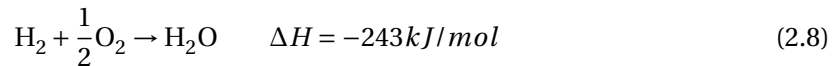
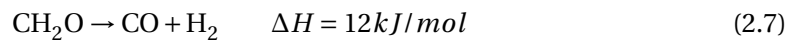
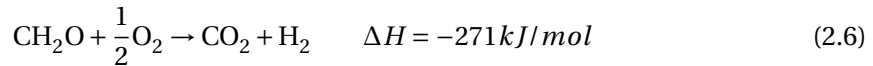
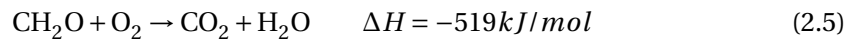
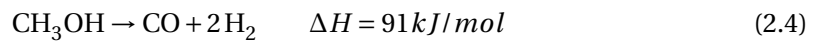
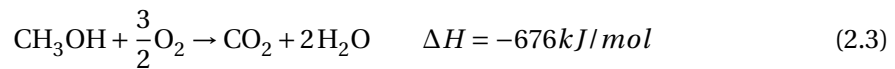


Figure 2.1: Illustration of the commercial methanol to formaldehyde process [4].

The methanol to formaldehyde synthesis involves a complex reaction network. In addition to Reaction 2.1 and 2.2, the following reactions can also occur [5]:



(2.10)

## 2.2. Silver Catalyst

In the silver-based formaldehyde synthesis, solid silver catalyzes a reaction between gaseous reactants, making it a heterogeneous catalyzed system. The reaction occurs on the silver surface, where there are active sites with varying reactivity. The difference in reactivity comes from local variation on the catalyst surface like terraces, steps and kinks, shown in Figure 2.2. The active sites adsorb reactants differently, and will thereby form and/or break different bonds, leading to varying products and product selectivities [8]. The driving force of heterogeneously catalyzed systems are gradients of chemical potential at the phase interfaces. The composition and shape of the catalyst is therefore sensitive to gas/liquid phase compositions [2].

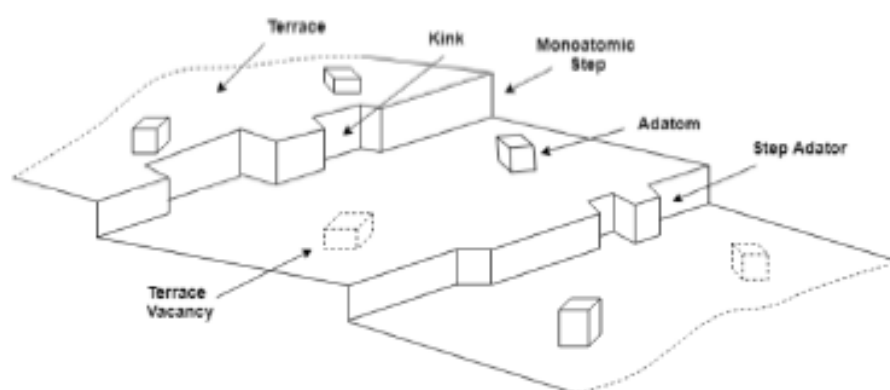


Figure 2.2: Illustration of a heterogeneous catalyst surface with defects [8].

Silver is a polycrystalline metal with face-centered cubic (fcc) structure. The geometry and structure of the crystal surface plays an important role when it comes to reactivity in catalysis. The surface consists of different planes that are described by its normal vector;

$$\mathbf{H} = hx + ky + lz \quad (2.11)$$

The letters  $h$ ,  $k$  and  $l$  are the Miller indices, which is the notation system for planes in a crystal lattice. To indicate the relevant surfaces, the Miller indices are often written in combination with the metal, for instance  $\text{Ag}(110)$  [8]. The building blocks of a surface structure, and the simplest fundamental planes are the low index planes. The low index planes of the fcc structure are presented in Figure 2.3. For high index planes, one or more of the Miller indices are larger than one. These planes do often have open structures and are known to facet at equilibrium. Faceting is when arrays of low index planes that are separated by steps are formed [9].

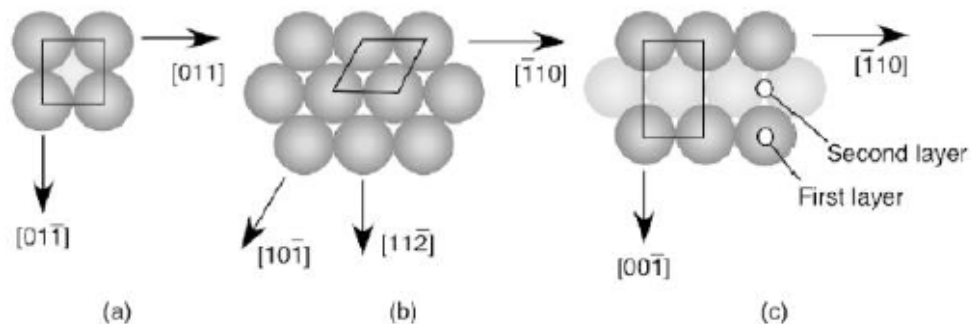


Figure 2.3: Face-centered cubic low index planes: (a)-fcc(100), (b)-fcc(111), (c)-fcc(100) [9].

The driving force of surface processes and phenomena in heterogeneously catalyzed systems, are minimization of the surface free energy. This is for instance lowered by exposing the most densely packed surfaces of polycrystalline metals, or cover surfaces with substances that reduces it, for instance oxygen [8]. Oxygen is known to adsorb selectively on open crystal structures, like Ag(110), which has high sticking coefficients [11]. The morphological changes that are made to lower the surface free energy can result in annealing of dislocations and grain boundaries, refaceting and sintering [2].

To attain a thermodynamically favorable structure, morphological restructuring of the silver catalyst occurs above the Tamman temperature (642 K). These changes involve pinhole formation and refaceting to enhance low index planes, and are linked to the silver lattice's ability to incorporate hydrogen and oxygen at elevated temperature [2][5]. There are several theories about the formation of pinholes. They were believed to be formed from a reaction between hydrogen and oxygen in the silver bulk and, to some extent, function as a compensation of surface smoothing and surface area reduction of sintered particles. Experiments does however show that they are present on silver treated in oxygen, exclusively. The main reason for pinhole formation is therefore believed to be oxygen dissolution and recombination along defects or in the bulk [5].

### 2.2.1. Silver and Oxygen Interactions

The complete methanol to formaldehyde reaction mechanism is not known. There is however a consensus that the interactions between oxygen and silver are essential in understanding the catalytic activity of silver. Experiments have shown that methanol adsorbs reversibly on silver without oxygen present, whereas it adsorbs dissociatively on silver that is pretreated by oxygen [7]. Very little dehydrogenation is therefore observed to occur in the absence of oxygen. Further research has proved that there can be three species of atomic oxygen present in the system. They have been identified as  $O_\alpha$ ,  $O_\beta$ , and  $O_\gamma$ , and their formations are dependent on silver morphology and reaction conditions [10]. The species exhibit different thermal stabilities, locations and silver-oxygen bindings, and can thereby lead to varying methanol conversion and formaldehyde selectivity [7]. Their pathways and roles are however still under debate [5][10]. Figure 2.4 visualizes the different oxygen species and their interactions with electrolytic silver at 923 K, as proposed by Waterhouse et al.

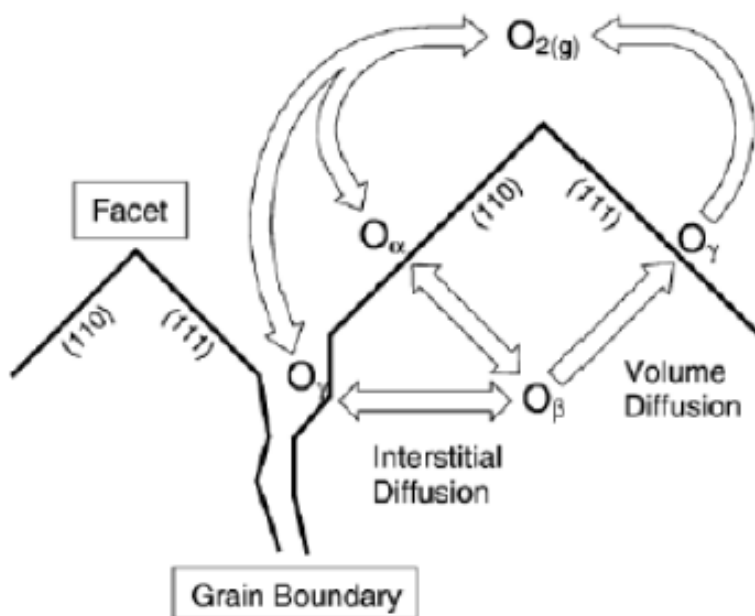


Figure 2.4: Reaction scheme for the formation of the different oxygen species [10].

The  $O_\alpha$  species is identified as a weakly adsorbed surface oxygen that chemisorbs on the low index planes of silver ((110 and (111)). It has been related to partial oxidation of methanol to formaldehyde, and oxidation of methanol and formaldehyde to carbon dioxide. At elevated surface coverage,  $O_\alpha$  diffuses into grain boundaries and the silver bulk and forms bulk-dissolved oxygen ( $O_\beta$ ). This oxygen species is associated with bulk restructuring at temper-

atures above 773 K [5].  $O_\gamma$  is a strongly chemisorbed oxygen species that is formed from volume diffusion of  $O_\beta$  through the faceted surface at elevated temperatures ( $>900$  K). This species can also be formed in the grain boundaries by oxygen chemisorption on reconstructed Ag(111) planes.  $O_\lambda$  is associated with dehydrogenation of methanol to formaldehyde and hydrogen, or formaldehyde and water [7]. This species can also diffuse and substitute for silver lattice atoms, leading to stress and thereafter failure and possibly reduction of the crystallite size [11]. Adsorbed hydrogen atoms are also suspected to diffuse and react with oxygen in the bulk [12].

Another theory is that only one oxygen species is active in the reaction mechanism. Wachs and Madix claimed that this is the  $O_\alpha$  species [13]. Their model has further been used to develop a microkinetic model for methanol oxidation to formaldehyde, and formaldehyde oxidation to carbon dioxide [14]. More recent models also indicate that the surface oxygen promotes formaldehyde through methoxy intermediates, and that oxygen dissociation is the most critical step [15].

### 2.2.2. Catalytic Activity

In the MTF reaction, both the selectivity towards formaldehyde, and the methanol conversion is reported to increase with the temperature. This is unexpected as formaldehyde is thermodynamically unstable, and the intermediate in complete oxidation to carbon dioxide. The increasing selectivity is a result of the participation of both the dehydrogenation and partial oxidation of methanol (Equation 2.1 and 2.2), which mainly occurs at high and low temperatures, respectively, and the thermal stability of  $O_\alpha$  and  $O_\gamma$ . Ultra-high vacuum (UHV) experiments have shown that the carbon dioxide selectivity is at maximum just before  $O_\alpha$  desorbs from the surface, meaning that  $O_\gamma$  is the dominant oxygen species in the temperature range used in the formaldehyde synthesis. This has also been confirmed by thermal desorption spectroscopy [2].

Surface defects, including the pinholes that are formed through high temperature and oxygen induced restructuring, are active for adsorption of oxygen. Experiments have shown that reactions at temperatures below 650 K are enhanced by the surface defects created from their formation [2][11]. This occurs as a result of more oxygen being able to diffuse into the silver lattice, as grain boundary defects are formed [6]. These defects are necessary for diffusion of oxygen from the bulk to the silver surface at temperatures between 673 and 873 K [11]. The structural changes also leads to the formation of  $O_\gamma$ . At elevated temperature ( $>900$  K), this oxygen species diffuses to Ag(111) surfaces, leading to recrystallization that further enables the catalyst to be active during the whole temperature range used for the MTF synthesis [2][6]. Oxygen adsorption on Ag(111) planes also stabilizes the surface, leading to lower surface free energy and subsequent crystal growth [2].



### 2.3. Mass Transfer

In a heterogeneously catalyzed reaction, the performance of the reactor can be affected by the mass transfer of reactants to the catalyst surface. Mass transfer is dependent on factors like the loading of catalyst, reactor type and temperature. It can be divided into external- and internal mass transfer, which has different mechanisms and different ways of being assessed [16]. If mass transfer limits a reaction, it can cause determination of wrong reaction rate, reaction order and activation energy. [17].

External mass transfer occur when reactants are transported from the gas phase to the catalyst surface. Eventual limitation can be due to a stagnant film close to the catalyst surface, and several methods can be used to investigate its existence. One method is through varying the linear gas velocity, as this can affect the thickness of an eventual stagnant film and thereby also affect the mass transfer [16]. The stagnant film concept is not applicable in cases where laminar flows are used, and other methods like changing inert gas, diffusivity or total pressure can then be employed [17][16]. One way of changing the diffusivity, without affecting the kinetics, is to increase the inert concentration of the feed while sustaining the partial pressure of the reactants [17]. If the conversion changes after employing the mentioned methods, external mass transfer limitation exist in the system [16][17][18].

Internal mass transfer involves diffusion of reactants from the catalyst surface into the pores. Too wide or narrow pores can lead to collision of molecules with each other or the pore walls. This would lead to internal mass transfer limitation, and its existence in a system can be determined by performing experiments with varying particle sizes [16][17]. In the reactor that is employed in this thesis, the stagnant film theory is not dominant, and it is therefore only performed investigations of external mass transfer limitation.

## 2.4. Catalyst Characterization

To achieve the wanted yield or selectivity in a catalytic reaction, it is important to understand the catalyst and its structure and composition. The catalyst is therefore often characterized using varying techniques depending on structure and the desired information. The goal of the characterization is to examine the catalyst properties, preferably *in situ*, and several microscopic, spectroscopic and diffraction techniques can be used to obtain the information. In this thesis XRD, SEM and EBSD were used to examine how the silver morphology changed when treated in different conditions at elevated temperature.

### 2.4.1. X-Ray Diffraction

X-ray diffraction (XRD) is one of the most used technique for catalyst characterization. It can be used for both qualitative and quantitative analyses of crystalline material and are often used to measure particle size and identify crystallographic phases present inside a catalyst.

X-rays has wavelengths in the Ångström range, and are energetic enough to penetrate solids and probe their internal structure [8]. In the diffractor, an analyte is bombarded with high-energy electrons. The X-rays can be emitted from two processes, that creates either  $K_{\alpha}$ - or  $K_{\beta}$ -radiation [19].  $K_{\beta}$  is often removed, as it is the weaker radiation, by employing monochromators or filters.  $K_{\alpha}$  can be emitted as both  $K_{\alpha 1}$ - and  $K_{\alpha 2}$ -radiation, and can be seen as overlapping diffraction peaks, that is more severe for higher  $2\theta$  angles. The wavelengths of these emissions are too close for one of them to be removed by filters, and a monochromator is therefore needed. In cases where this is relevant,  $K_{\alpha 2}$ -radiation is removed as this is the weakest emission [20].

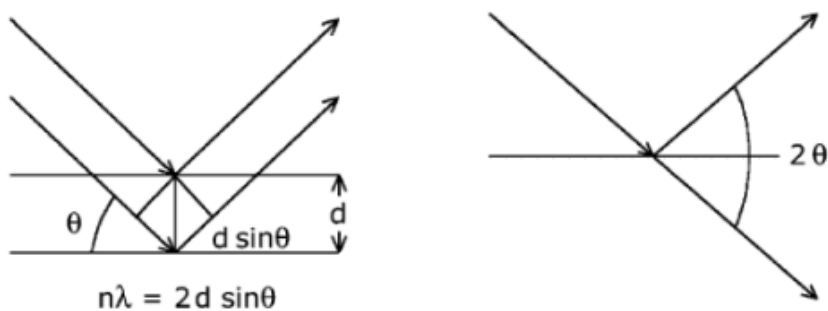


Figure 2.5: Constructive diffraction of X-rays, where the direction is given by Bragg's law [19].

Diffraction occurs when atoms in a periodic lattice, scatter X-ray photons. Powdered samples have particles that are oriented varying ways, and when the orientation corresponds to the angle of the beam, an image of the diffraction lines will be formed. The sample can be rotated to increase the number of particles contributing to the diffraction pattern [19]. A per-

fect crystal will give narrow diffraction spots, and ideal shapes are Gaussian and Lorentzian distributions. Eventual line broadening is a result of microstrain and size, in addition to instrumental factors. Strain broadening comes from lattice imperfection, like defects, dislocations and vacancies that causes atoms to deviate from their ideal positions. Size broadening occurs when the crystal does not contain enough planes to cancel the phase shifts caused by a beam angle away from the Bragg angle [20]. Diffraction from a crystal is described by the Bragg relation;

$$n\lambda = 2d\sin\theta; \quad n = 1, 2, \dots \quad (2.12)$$

where  $n$  is the order of reflection,  $\lambda$  the wavelength,  $d$  the distance between two lattice planes, and  $\theta$  the angle between the incoming X-rays and the normal to the reflecting lattice plane. When this relation is fulfilled, constructive interference can occur. The lattice spacings can be calculated by measuring the angles,  $2\theta$ , when constructively interfering X-rays leave the crystal [8].

One of the limitations with XRD is that it is a bulk analysis, meaning that it does not detect eventual changes on the surface. Another limitation is that the sample needs to possess a crystalline structure to obtain clear diffraction peaks. When conducting this technique, it can therefore not be concluded that there are not any other phases than the ones detected present. However, this limitation causes the width of the diffraction peaks to carry information about the reflecting planes dimensions. The following equation, the Scherrer formula, is frequently used to relate crystallite size to line width:

$$L = \frac{K\lambda}{\beta\cos\theta} \quad (2.13)$$

$L$  is a measure for the dimension of the particle in the direction perpendicular to the reflecting plane,  $K$  is a constant (often equal to 1),  $\lambda$  the X-ray wavelength,  $\beta$  the peak width, at full width at half maximum (FWHM) or integral breadth (IB), and  $\theta$  the angle between the beam and the normal on the reflecting plane [8]. The equation provides an estimate of the size from the ratio of two averages that are weighed by the particle volumes, and not by surface area or number. Instrumental factors and internal strain, who also contribute to peak broadening, are not taken into account in this equation [19].

Rietveld refinement is another method that can be used to determine the crystallite size of a sample. As oppose to the Scherrer equation, who analyses a peak at the time, the Rietveld refinement analyses the whole diffraction pattern. In addition, it includes the contributions from both the microstructure and the instrument. The refinement involves modeling of a diffraction pattern with a goal of getting it as similar as possible to the relevant measured

pattern [23]. The modeling is performed by calculating the profile and background, based on instrumental and structural properties, and fitting them to the measured pattern by refining some of the structural parameters. The modeled diffractogram can then, when finished, be used to obtain structural and microstructural information about the sample [22] [23].

Equation 2.14 defines how the intensities of the diffraction spots at position  $i$ ,  $y_{calc,i}$ , are calculated in the Rietveld refinement.

$$y_{calc,i} = \sum_p (S_p \sum_{s(p)} (|F_{calc,s,p}|^2 \Phi_{s,p,i} Corr_{s,p,i})) + Bkg_i \quad (2.14)$$

The first sum includes all crystalline phases,  $p$ , in the pattern, and the second includes the Bragg reflections,  $s$ , of the phases,  $p$ , at the position  $i$ . Further,  $S_p$  represents a scaling factor,  $|F_{calc,s,p}|^2$  the reflection intensities,  $\Phi_{s,p,i}$  the profile function,  $Corr_{s,p,i}$  various correction factors, and  $Bkg_i$  the observed background at position  $i$  [21].

The peak shape in a diffraction pattern is a function of instrumental parameters like slit size and radiation source, and sample parameters like defects and strain/stress. It varies with  $2\theta$ , and in some cases with hkl-indices [23]. A convolution of appropriate functions, like pseudo-Voigt-, Pearson VII- or fundamental parameter functions are frequently used to adapt the shape of the profiles during modeling. The latter is the most common and includes both specimen and instrument contributions, and uses a physical intuitive model that gives information about the microstructure of the sample, i.e size and strain. The source emission profile and thermal displacement can also contribute to the profile shape. The former is applicable in cases where diffractometers employing broad-band filters, for instance metal  $K\beta$  filters, are used. An emission profile is then added to the model for better description of the shape, and to permit use of data without  $K\alpha_2$  stripping [20]. Thermal displacement is caused by atomic, thermal movement that decreases the scattered intensities. This can be adjusted by using constraints, which are exact mathematical conditions that reduces the amount of refineable parameters [24] [20]. The peak position must also fit well to the observed pattern before starting the refinement. Deviations in  $2\theta$  can be a result of sample displacement from the  $2\theta$  circle center and zero offset. Both can be corrected by employing internal standards, and are easily adjusted in the relevant software [23].

When a sample is prepared for XRD analysis, the powder is placed in a flat plate sample holder. If the crystallites are not spherical, they tend to align in preferred orientation(s) which can lead to incorrect intensities in the diffraction pattern [21] [23]. This effect can be reduced by introducing preferred orientation functions in the modeling. Two methods that are frequently used are the PO March-Dollase method where a preferred-orientation vector is added and refined, and PO Spherical Harmonics where a normalized symmetrical spherical harmonic function with an order from 2 to 8 can be chosen, depending on the amount of refined coefficients needed to obtain the wanted result. Examples of properties that are in-

cluded to describe the crystals are spacegroup, lattice parameters and site occupations. The spacegroup is related to atom position within the cell and the cell symmetry, lattice parameters to the dimension of the unit cell, and site occupancies represents the atomic positions [20].

The background in a powder diffraction pattern comes from, among others, the sample environment, incoherent scattering, inelastic scattering and thermal diffuse scattering [21]. In Rietveld refinement, it can either be modelled by a function of several refinable parameters or estimated through linear interpolation of chosen points between the peaks, followed by subtraction. Both methods work well when the peaks resolve to the baseline. The latter is flexible, but cumbersome, while the former is entirely empirical, and refining the parameters will not help if the function does not describe the background well [23].

The difference between the calculated and measured patterns can be observed both through a difference profile plot and numerically, by R values. There are two R values that can be calculated to determine how good the fit is; the weighted-profile- ( $R_{wp}$ ) and the statistically expected ( $R_{exp}$ ) R value .

$$R_{wp} = \frac{\sum w_i (y_i(obs) - y_i(calc))^2}{\sum w_i (y_i(obs))^2}^{1/2} \quad (2.15)$$

$$R_{exp} = \frac{(N - P)}{\sum w_i y_i(obs)}^{1/2} \quad (2.16)$$

In Equation 2.15 and 2.16,  $w_i$  represents the weight, and  $y_i(obs)$  and  $y_i(calc)$  the observed and calculated intensities.  $N$  and  $P$ , in Equation 2.16, represents the number of observations and the number of parameters, respectively. The number of observations is determined by the number of steps in the profile, which depends on the amount of reflection overlap involved, number of steps across the peak and the counting time. The parameters are structural properties that can be refined. The goal is to get  $R_{wp}$  close to  $R_{exp}$ , and for both to be as low as possible, preferably below 5 % [25]. The goodness of fit (GOF) is another parameter that is often used to describe the fit. It is defined as  $R_{wp}$  divided by  $R_{exp}$ , and the desired GOF-value is 1 [23].

Too many refined parameters can lead to incorrect results, and it can thereby be difficult to know when the fit is good enough. A refined background is also likely to contribute to the  $R_{wp}$  value, and comparison of R values from different XRD patterns can thereby be misleading. For these reasons, the difference profile plot is the best tool for optimizing the fit [23].

The Double-Voigt approach is often used for calculation of crystallite sizes when employing the Rietveld refinement. This method is a convolution based line profile analysis where the Gaussian and Lorentzian components of two Voigt functions are refined with a goal of obtaining microstrain and size. This is a flexible and simple approach that is easy to implement, requires a small amount of refineable parameters and can distinguish between background and profile tails. The simplicity of this approach is however also its main disadvantage, as microstructural effects are not related to profile broadening from Gaussian or Lorentzian components through any physical law. For the calculation, it is considered that the crystallites consists of cells and columns along the scattering direction. The volume weighted mean column length is used since the power of a columns scattering is dependent on its volume.

$$L_{Vol,IB} = \frac{K}{\beta_{Voigt}CS_LCS_G} \quad (2.17)$$

In equation 2.17,  $L_{Vol,IB}$  represents the volume weighted mean column length,  $K$  the Scherrer constant,  $\beta_{Voigt}$  the peak width of the convolution, based on integral breadth, and  $CS_L$  and  $CS_G$  the Lorentzian and Gaussian component type convolutions, respectively. The convolutions does not have any direct physical interpretation. Integral breadth is chosen for the calculations because its evaluation is approximately independent on the distribution on shape and size. Further, the Scherrer constant is often assumed equal to 1 [20].

### 2.4.2. Scanning Electron Microscopy

Electron microscopy is a technique used to determine the structural properties of samples. An electron beam between 100 and 400 keV is sent towards an analyte, and several types of electrons are scattered. These can be detected and will provide varying information about the sample, like crystallography and morphology [8].

Scanning electron microscopy (SEM) detects the yield of either backscattered- or secondary electrons using a narrow electron beam over the analytes surface. Secondary electrons come from the surface area and have mostly low energies (5-50 eV), while backscattered electrons originate from deeper within the sample. The latter therefore also carries information about the composition of the sample. The pictures obtained from SEM contains contrasts because of the composition and topology of a surface [8]. The analytes in SEM needs to be conductive, and gold is frequently used as eventual coating [26].

### 2.4.3. Electron Backscatter Diffraction

Electron backscatter diffraction (EBSD) is a characterization technique that is used to analyze crystalline and polycrystalline materials. It is often used in combination with SEM, and can determine morphology and size of grains, crystallographic relationship between phases, crystal structure and crystal orientations [26]. The analyte in EBSD needs to be conductive, have grains with diameters larger than 10 nm, can not have excessive surface strains, and have a flat surface [26].

The samples are analyzed using a stationary, high-energy electron beam that illuminates a depth of approximately 20 nm. The detector, comprised of a phosphorous screen, collects the backscattered electrons that has undergone coherent Bragg scattering, and to allow more electrons to be diffracted, the sample is tilted 70 ° from the beam. The detected electrons forms a diffraction pattern made up of Kikuchi bands, which are characterized as arrangements of bright, parallel and regular bands on a steep background, where their intersections form zone axes. Kikuchi bands can be considered to be a gnomonic projection of the crystal lattice, and the band widths are, according to Braggs law (Equation 2.12), related to the distance between the lattice planes. [26].

To obtain crystallographic information, like the orientation and crystal phase, orientation imaging microscopy (OIM) can be performed. This technique utilizes the EBSD pattern of the relevant sample to construct a crystal orientation map. The map is obtained by programming the specimen stage or electron beam to move, so that different points on the sample is analyzed [27].

## 2.5. Analytical Techniques

### 2.5.1. Light Microscope

Light microscope is a basic instrument that is frequently used in the food industry and material science. It uses a light beam for visualization of an objects fine details, and the source is often a halogen or tungsten lamp. The beam is focused through or onto the object by employing a series of glass lenses. Some of the light is absorbed, creating an image of microstructural details. The image can be enlarged through convex objective lenses that gives magnifications from x10- x1000. The resolving power depends on the type of objective lenses, and the its area for light passage. The image that is formed can be observed both through a camera and through binocular eyepieces [28].

### 2.5.2. Gas Chromatography [29]

Chromatography are separation techniques that are based on separation of components by distribution in two phases; a mobile- and a stationary phase. The separation can occur in a column or on a sheet, and are caused by the difference in the components equilibrium distribution in the phases. This causes the components to use different velocities from injection to detection, and the time they use is referred to as the retention time. To obtain good separation of the relevant components, knowledge about chromatography and the conditions affecting it is important. The separation is dependent on the size of the sample, temperature, pressure, type of mobile and stationary phase and the diameter and length of an eventual column.

Gas chromatography (GC) is a chromatographic method that employs an inert gas as the mobile phase. The stationary phase is either an adsorbent (GSC) or a nonvolatile liquid (GLC), and the analyte needs to be stable at the relevant temperatures, and volatile. The technique is often used to separate, determine the purity, and sometimes identify the components in a mixture, and is often combined with mass spectroscopy. In a GC, the evaporated sample is carried by the mobile phase through a column. After separation, the sample passes through a detector, and a chromatogram will be generated. Some advantages with GC are its high resolution, low detection limit and rapid analyses. The analyses can also be automated by a computer that controls the injections, separations and data processing.

The goal of the GC columns are to obtain successful and efficient separation of the mixtures, and the most common are preparative-, analytical- and capillary columns. The preparative columns are used when isolation of components after the separation is desired. They are designed to separate large sample volumes, has inner diameters from 1-2 cm and a packing material with 20-30 % stationary phase. Analytical columns are frequently used for quantitative and qualitative analyses, and has inner diameters of 2-6 mm and lengths of 1-5 m. These are packed with a material including up to 10 % stationary phase. Capillary columns



are used for separation of complex mixtures. The stationary phase covers the wall of the column (wall-coated open tubular column), and they have inner diameters of 0.2-0.7 mm and lengths of 10-100 m.

The detectors used in GC can be split into two groups; mass- and concentration-sensitive detectors. The latter requires thorough control of the gas velocity when performing quantitative analyses. Two commonly used detectors are the flame ionisation- and thermal conductivity detector (FID and TCD). The latter is concentration sensitive, and one of the oldest GC detectors. The streams flowing to/from the column goes through the detector, over their respective heated filaments. Gases with high thermal conductivity, like hydrogen or helium, are employed and will absorb the heat from the filaments. When the different components are eluted, the filaments will have different resistance, and a peak will be registered. Every change in the composition of the carrier gas is detected. The detector is also non-destructive and universal, but has low sensitivity.

## 2.6. Catalytic Activity [30]

Activity and selectivity are parameters that are often used to determine the performance of a catalyst during reaction. There are several ways to express activity, for instance through rate of reaction, turnover frequency (TOF) and/or conversion. In this thesis the latter is employed, and it is defined as the amount of reactant consumed over the total amount of reactants supplied. High conversion leads to high activity, at the given conditions, and one way of calculating it is presented in Equation 2.18.

$$X_i = \frac{y_{i,in}F_{tot,in} - y_{i,out}F_{tot,out}}{y_{i,in}F_{tot,in}} \quad (2.18)$$

$X_i$  represents the conversion of reactant  $i$ ,  $y_{i,in}$  and  $y_{i,out}$  the component mole fractions in and out of the system, and  $F_{tot,in}$  and  $F_{tot,out}$  the total flows in and out of the system. By assuming that all reactants are converted to products, and that the inlet and outlet streams to/from the system are different, the inert can be used to express the total flow. The following equation for conversion can then be obtained.

$$X_i = 1 - \frac{y_{i,out}y_{inert,in}}{y_{i,in}y_{inert,out}} \quad (2.19)$$

Selectivity gives information about which product is favored in the reaction(s). It is defined as amount of product formed over amount of product stoichiometrically possible. There are several ways of calculating the selectivity. Formaldehyde selectivity can for instance be calculated as a function of the total amount of methanol converted (Equation 2.20) or as a function

of total amount of carbon produced (Equation 2.21).

$$S_{CH_2O} = \frac{F_{tot,out} y_{CH_2O,out}}{F_{tot,in} y_{CH_3OH,in} - F_{tot,out} y_{CH_3OH,out}} \quad (2.20)$$

$S_{CH_2O}$  represents the formaldehyde selectivity,  $F_{tot,in}$  and  $F_{tot,out}$  the total flows in and out of the system and  $y_{i,in}$  and  $y_{i,out}$  the component mole fractions in and out of the system.

$$S_{CH_2O} = \frac{y_{CH_2O,out}}{y_{CH_2O} + y_{CO_2}} \quad (2.21)$$

## 3. Experimental Section

### 3.1. Health, Environment and Safety

All experiments and characterization techniques were performed at NTNU's laboratories at Gløshaugen in Trondheim. The main risks connected to them are the explosive and toxic gases used at high temperatures. To ensure safe work environment, training were required to gain access to the labs, appropriate protective gear were used at all times, and leak tests were performed before each experiment, using a leak test spray. In the MTF set-up, a gas detector was also used for leak testing, and it was kept in the rig at all times. This setup also contains controllers, safety valves and a proper ventilation system, making the risks of the experiments acceptable.

There were also other ongoing experiments in the lab during the time period of this project, and risks connected to these were also taken into account. An assessment covering the risks connected to all experiments and characterization techniques were conducted and can be seen in Appendix E.

### 3.2. Experimental Set-ups

The analyses and experiments in this thesis were performed on silver particles, silver net and annular silver, and their properties are presented in Table 3.1. The particles were used as received, while the silver net were cut into four pieces, and the annular silver were cut to fit the reactor (reactor details can be presented in Appendix A). Treatment of the silver were performed in a calcination - and a MTF set-up, and they are explained in Section 3.2.1 and 3.2.2, respectively.

Table 3.1: The different purities and sizes of the silver particles, silver net and annular silver, and the companies providing them.

	Particles	Net	Annular
Provided by	K.A. Rasmussen	Yara	Goodfellow
Purity	99.99 %	99.99 %	99.95+ %
Size	Fractions of 0.25- 0.50 mm	0.19 mm diame- ter	10.0 mm diameter, 2 cm height

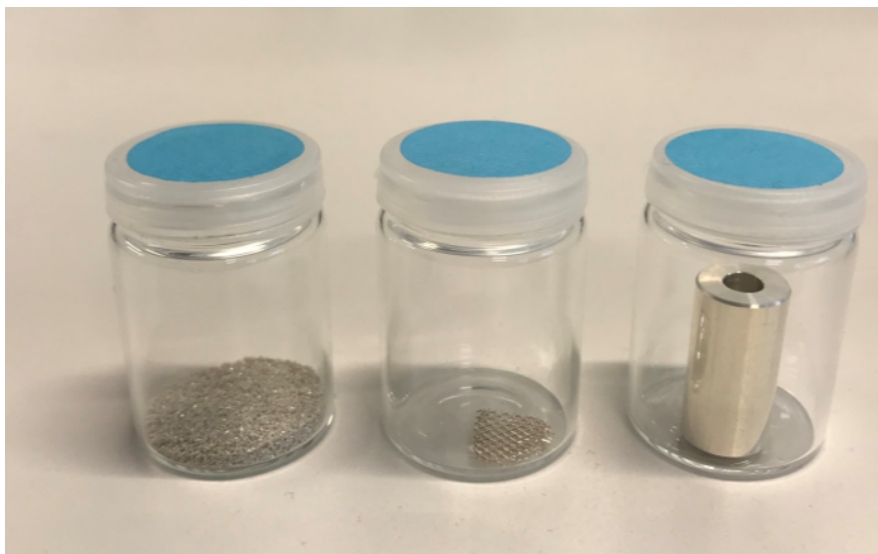


Figure 3.1: Image of the three different silver catalysts that were used in the experiments. From the left: Particles, a quarter of the silver net and annular silver that has been cut to fit the reactor.

### 3.2.1. Calcination Set-up

In the calcination set-up, a quartz calcination reactor is placed in an isolated oven where the temperature is measured by a thermocouple (N-type). The inlet gas flow is fed from gas cylinders, through one or more pipelines, and can be regulated from 0-120 ml/min by a rotameter. The outlet gas goes through a water seal before it is ventilated. The relevant temperature program is set by an Eurotherm.

### 3.2.2. Methanol to Formaldehyde Set-up

In the MTF set-up, a quartz fixed bed reactor is placed in an isothermal oven that uses two eurotherms to control the reaction temperature. The formaldehyde solution and methanol and water mixture are held in containers that are pressurized with helium to ensure high enough pressure for transportation to the reactor. Four high pressure pipe lines (1/4 ") lead the gases from gas cylinders to the reactor; one line is for synthetic air (10-500 Nml/min), one for carbon monoxide or hydrogen (1-100 Nml/min) and two for nitrogen and helium (4-200 and 30-1500 Nml/min). Liquid- and mass flow controllers are employed to feed the liquids and gases to the system. These are controlled digitally through the LabVIEW v.13 software, but there are also pressure valves and regulators connected to each pipeline for manual control. An evaporator is used to evaporate and mix the reactor feed under controlled conditions (a CEM evaporator). The product gases are sent through a water seal and to a gas chromatograph, and to avoid condensation, the pipelines are covered with electric heating bands. Both

the temperature of the gases send to the GC and the temperature in the reactor are monitored using thermocouples (K-type).

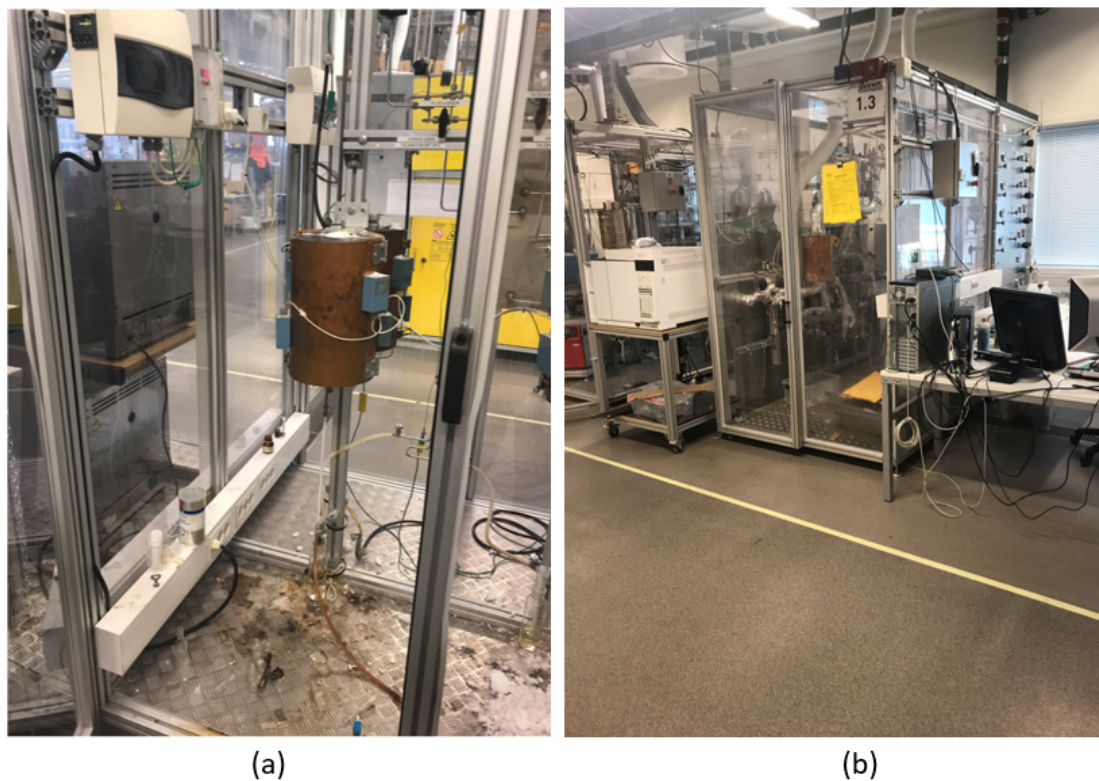


Figure 3.2: Images of the calcination set-up (a) and MTF set-up (b), including the gas chromatograph (left) and the computer used to control the reaction.

### 3.3. Experiments

#### 3.3.1. Calcination

Calcination experiments were performed to treat silver in conditions relevant to the MTF reaction. Calcination of both silver particles and silver net were performed, and the conditions are presented in Table 3.2.

Table 3.2: Conditions for the calcination experiments, including catalyst type.

N	Ramping rate [°C/min]	Temperature [°C]	Duration [h]	Atmosphere	Catalyst type
1	10	650	5	Air	Particles
2	10	650	45	Air	Particles
3	10	650	45	Air	Net
4	10	650	19	Hydrogen (2 %) and argon (98 %)	Particles
5	10	650	19	Hydrogen	Particles
6	10	650	19	Nitrogen	Particles

The catalyst (1.0 g of particles, 0.6 g of net) was added to a calcination reactor, which was further placed in the oven. After leak testing, the relevant gas flow was adjusted to 100 ml/min, and the program was run. The catalyst bed was heated from room temperature to 650 °C with a rate of 10 °C/min and was then held isothermal for 5 to 45 hours.

#### 3.3.2. Methanol Oxidation

Two methanol oxidation experiments were performed in the MTF set-up. Both were conducted over annular silver (2 cm, 13.29 g), with an initial total flow of 250 Nml/min, temperature of 600 °C and reaction duration of 4 days. The goal of the experiments were to check for mass transfer limitations by performing them in two different inert gases, helium and nitrogen, as described by Beretta et. al [18]. In addition, the total flow were adjusted, to 150 and 350 ml/min, and the oxygen concentration in the feed were halved and doubled. Because of problems with the software controlling the flows, both experiments were conducted in helium and data from a previous nitrogen experiment were obtained. The component flow of the reactants are presented in Table 3.3. Oxygen were added as air and the methanol/oxygen ration were 1.34. The temperature at different vertical positions in the reactor were measured regularly to observe how it changed and to detect eventual gas phase reactions. Other experiments were performed in the set-up prior to the methanol oxidation, and calibration of the flow controllers were therefore already performed.

Table 3.3: Component flows fed to the reactor. The first column is the standard 250 Nml/min feed, the two next columns represents the change in total flow, and the last two the halving and doubling of the oxygen concentration.

	250 Nml/min (standard)	150 Nml/min (Low LGV)	350 Nml/min (High LGV)	250 Nml/min (Half O <sub>2</sub> )	250 Nml/min (Double O <sub>2</sub> )
Inert	167	99.9	233	185	130
Air	36.6	22.0	51.3	18.3	73.3
Methanol and water	3.01	1.80	4.21	3.01	3.01

### 3.4. Analytical Equipment and Characterization Techniques

#### 3.4.1. X-Ray Diffraction

XRD was used to measure the crystallite sizes of silver before and after being exposed to the conditions presented in Table 3.2. XRD was performed using a D8 DaVinci diffractometer that uses a copper anode, and contains a thin Nickel-film that removes  $K_{\beta}$ -radiation. The samples were analyzed using a program for crystalline samples that measures from 35-105 °, at  $2\theta$  angles with a fixed V6 slit, which means that 6 mm of the sample is illuminated at all angles. The particles were crushed, using a mortar, to obtain a homogeneous sample with grains less than 10  $\mu\text{m}$ . To obtain a representable diffractogram, the height of the sample needs to match the height of the sample holder (see Figure 3.3). Further, the Diffrac.Suite EVA 5 and Diffrac.Suite Topas 5 softwares were used to analyze the results. The former were used to calculate the crystallite size through the Scherrer equation, where a Scherrer constant of 0.89 was employed, and the latter through Rietveld refinement. The refinement parameters that were used are presented in Table 3.4, and the emission profile in Table 3.5.

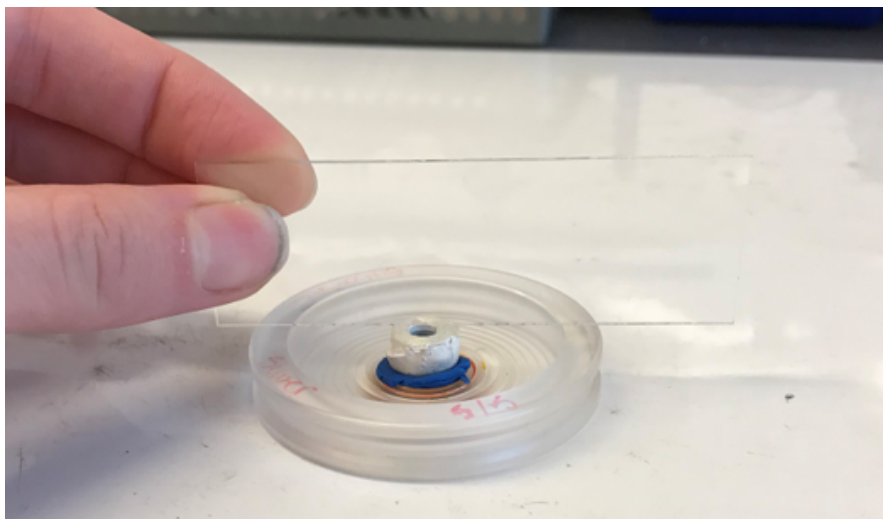


Figure 3.3: Correct sample preparation for XRD where soft clay were used to get the correct sample height.

Table 3.4: Details of the parameters used in the Rietveld refinement in Topas. Parameters marked with "-" represents inputs, and "+" represents refined parameters. The structural properties were obtained from the databases in Diffrac.Eva and PDF-4+.

	Refinement parameters
Emission profile	Table 3.5
Background	
+ Chebyshev polynomial	Order 10+
Instrument	
- Primary radius	280
- Secondary radius	280
- Point detector	-
- Receiving slit	-
- FDS shape	-
- Linear PSD	Y
- LPSD angle range	3
- FDS angle	As chosen
- Full axial model	Y
- Source length	12
- Sample length	12
- RS length	12
- Prim soller	2.5
- Sec soller	2.5
- N beta	30
- Simple axial model	-
Corrections	
- Zero error	-0.1042
+ Sample displacement	-0.2550
- LP factor	"0"
Peak shape function	FP
Structural properties	
- Spacegroup	225, Fm-3m
+ Lattice parameter (Å)	4.0853
- Site occupancies, (x, y, z)	(0, 0, 0)
Preferred orientation(s)	
+ PO spherical harmonics	Order 4-8
Thermal displacement	Biso



Table 3.5: Example of an emission profile added to the Rietveld refinement. The profile is updated regularly, and several were therefore used in the refinements. All the values in the table are inputs.

Area	Wavelength (Å)
0.0158	1.535
0.5767	1.540596
0.0759	1.541058
0.2407	1.544410
0.0867	1.544721
0.0012	1.476682
0.0016	1.392524
0.0015	1.488469

### 3.4.2. Scanning Electron Microscopy

SEM was conducted to observe how the different experiment and calcination conditions affected the silver surface. A Hitachi S-3400N instrument was employed, and an acceleration voltage of 15 keV, with about 5 mm working distance and 40 % probe current were used for these analyses. The silver samples were mounted to the sample holder using carbon tape, and the pictures were taken with a speed of 40 seconds.

### 3.4.3. Electron Backscatter Diffraction

The goal of EBSD was to gain information about grain orientations of the particles and the annular silver. In order to do so, an approach for the preparation of silver for this technique was also developed. The samples were prepared by molding, followed by grinding and polishing. Both hot mounting in phenolic resin with carbon filler (8.00 g) and molding in epoxy (7.14 g of Epofix resin and 0.86 g of Epofix hardener) were performed to determine the most suited material for the grinding and polishing required to obtain a flat surface. A recommended approach for grinding and polishing of noble metals were employed, and the samples were washed in water between each step. A light microscope, Zeiss Axio, were used to check the sample for scratches, so it could be determined if more polishing would be necessary. Before conducting EBSD, the conductivity of the samples were increased by covering them in aluminium foil, and the particles were additionally coated with two layers of carbon. The latter were performed by Yingda Yu at the department of material technology at NTNU. The details for the grinding and polishing of the molded samples are presented in Table 3.6, and the approach were obtained from Buehler [31].

Table 3.6: Detailed approach for grinding and polishing of silver after molding. The goal was to obtain a flat surface so that EBSD could be conducted.

Step	Grinding 1	Grinding 2	Grinding 3	Grinding 4	Polishing 1	Polishing 2
Surface	SiC Foil #500	SiC Foil #1200	SiC Foil #2000	SiC Foil #4000	MD-Mol	MD-Nap
Abrasive type	-	-	-	-	DiaPro Mol R 3 $\mu$ m	DiaPro Nap 1/4 $\mu$ m
Lubricant type	Water	Water	Water	Water	-	-
Speed (rpm)	150	150	150	150	150	150
Force (N)	20	20	20	20	20	15
Time (min)	01:00	01:00	01:00	01:00	03:00	02:00

#### 3.4.4. Gas Chromatography

The gas chromatograph, Agilent Technologies 7890A, was used to analyse both the feed and product streams in the MTF set-up. The injection of the samples are regulated by an automatic valve system. The GC uses two columns to separate the gases; a PLOT molsieve 5A column for the light gases (hydrogen, helium, nitrogen, oxygen, carbon monoxide and methane), and a WCOT CP-sil 5 CB column for separation of water, carbon dioxide, methane, methanol, formaldehyde and formic acid, through their different boiling points. The gases are further detected by a thermal conductive detector (TCD), and the peak area and mole percentage of each component is observed via Agilent ChemStation. The GC ran continuously through both methanol oxidation experiments, and its results were analysed in Microsoft Excel. Helium and nitrogen were used as internal standards for the activity calculations.

The GC was calibrated for formaldehyde after the methanol oxidation experiments. This was performed by co-supervisor and involved injection of a solution with known formaldehyde concentration.

### 3.5. Calculations

To validate the methods of detection and the MTF set-up, mass balances of the system were conducted, and used to calculate the error of selected components. Because of systematic errors like simplifications and gas leakages, a limit of 5 % is acceptable. An example of carbon error is shown in Equation 3.1, where  $n$  represents a stoichiometric factor.

$$E_C = \frac{F_{tot,out} \sum n_{yC,out} - F_{tot,in} \sum n_{yC,in}}{F_{tot,in} \sum n_{yC,in}} \quad (3.1)$$

If the carbon error is above 5 %, the activity calculations will be incorrect, and calibration of the GC would be necessary. Since there are only two carbon products in the experiments performed in this thesis, formaldehyde and carbon dioxide, their selectivities can be calculated through Equation 2.21 if the error from the mass balance is too high.

## 4. Results and Discussion

### 4.1. Catalyst Characterization

#### 4.1.1. Unused Catalyst

The diffraction patterns from the unused particles, net and annular silver are presented in Figure 4.1. It is observed that measuring from 35-105° yields six sharp and narrow peaks, which is an indication of highly crystalline fcc silver. Some line broadening is however seen, and this can be a result of instrumental parameters and possibly size- and strain broadening. The peaks are also splitted, as a result of  $K_{\alpha 1}$ - and  $K_{\alpha 2}$ -radiation, and the split is clearer at higher angles. The fcc structure and Miller indices of the samples were confirmed in Diffrac.Eva, where it was also confirmed that the samples are pure silver. The Miller indices are included in Figure 4.1, and shows that there are both high- and low index planes in the samples.

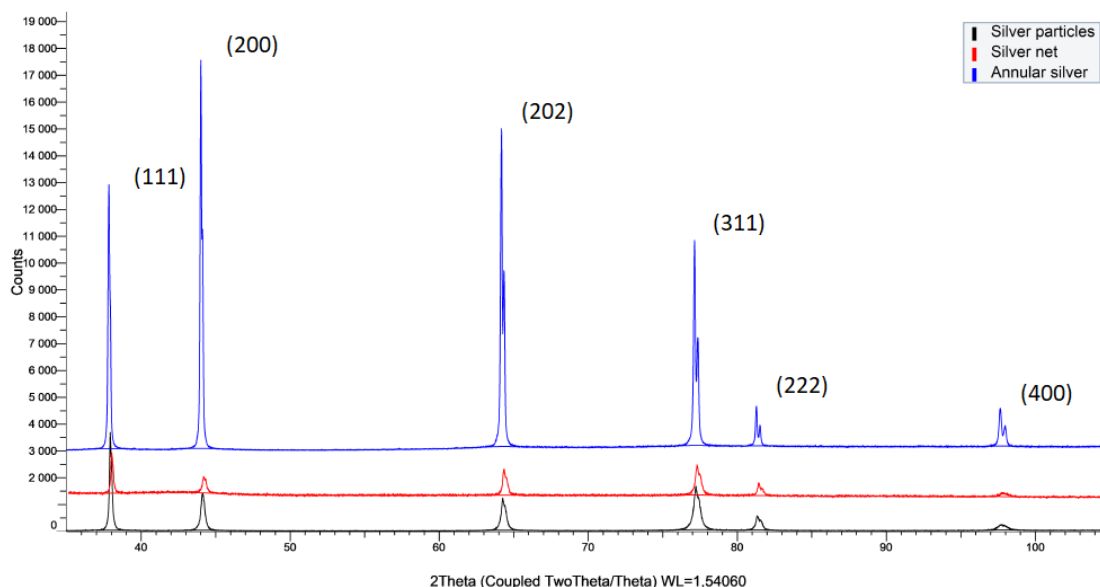


Figure 4.1: Comparison of the diffraction patterns of unused particles, net and annular silver.

Compared to the particles and annular silver, the diffraction pattern of the net has significantly more noise, which can be due to insufficient data. From Figure 4.1 it is also observed that the peaks of the annular silver are considerably higher than the remaining, indicating that the annular silver is more crystalline than the particles and net. These results also show that there are structural differences between the catalysts, which were as expected since they are provided by different companies and have different properties (see Table 3.1). The sample

displacements of the net and annular silver differed from the estimated offset (-0.225), and were 0.26 and -1.10, respectively. This is a result of incorrect preparation where the samples did not match the height of the holder. The displacement is removed in Figure 4.1 so that the diffraction patterns could be compared.

SEM images of the unused silver at different magnifications are presented in Figure 4.2, where it is seen that there are topological differences between the samples. The images visualize that the particles have rough surfaces with facets and terraces, resulting in large surface areas, also observed in previous analyses [7]. They also have small amounts of pinholes that most likely has been formed during production. Further, the images visualize that the net and the annular silver have similar surfaces. Both have highly corrugated surfaces, but to a less extent than the particles. They also have lines that probably has been formed under production or carving. Images taken in SEM are limited by the resolution of the instrument and their magnification, that causes them to not represent the entire surface. The images that are presented in this thesis are therefore chosen to give an overview of the different surfaces, and more images are attached in Appendix B.

The crystallite sizes obtained from both the Scherrer equation and the Rietveld refinement are presented in Table 4.1. When employing the Scherrer equation, the sizes were calculated for two peaks, peak 1 and 4 (see Figure 4.1) to check if the size would vary with the chosen peak, as this would indicate strain. Some of the samples were also reproduced to validate the approaches.

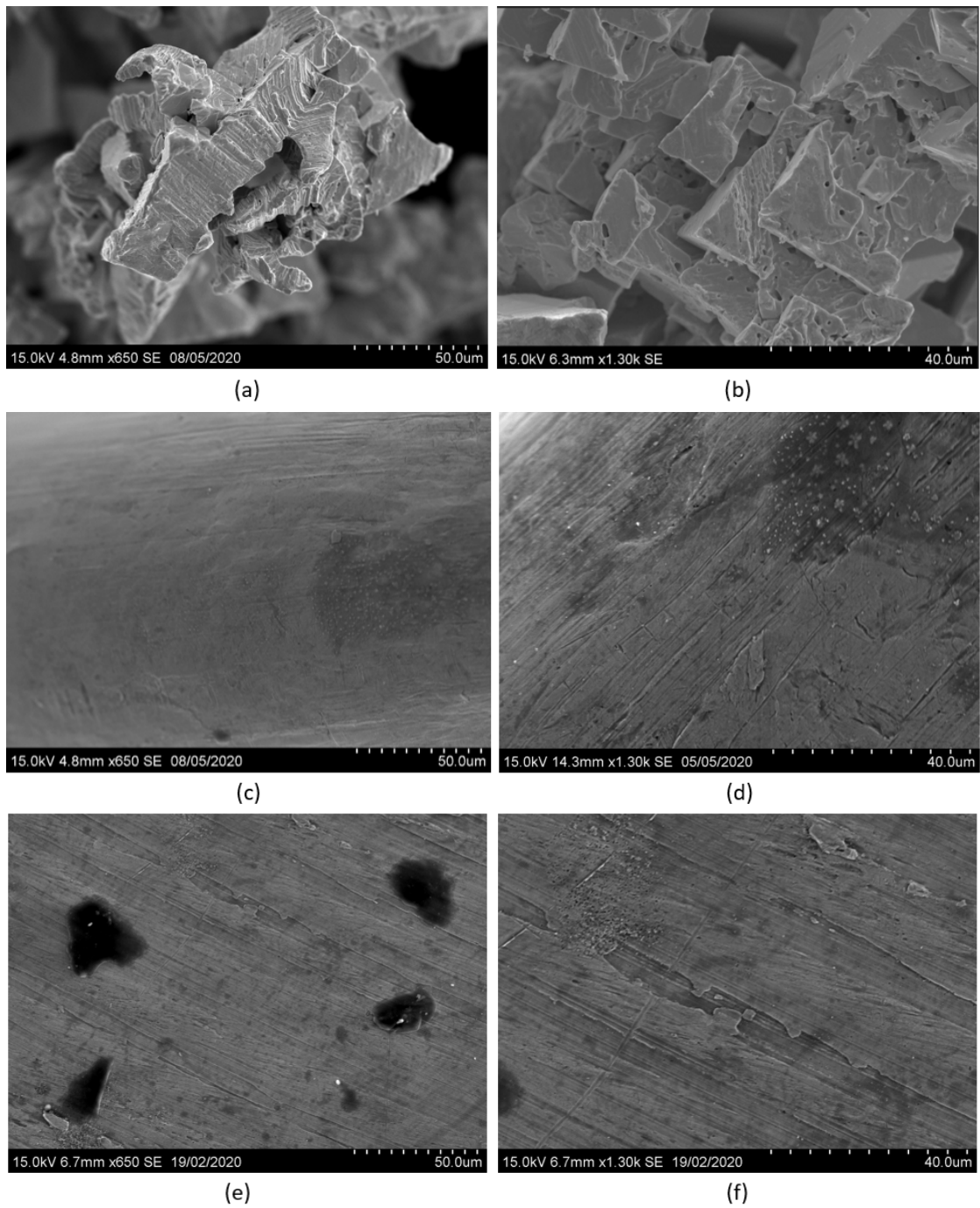


Figure 4.2: SEM images of unused silver particles ((a) and (b)), unused silver net ((c) and (d)), and unused annular silver ((e) and (f)), at different magnifications.

Table 4.1: Crystallite sizes for both unused silver and silver exposed to varying conditions. The sizes are calculated from both the Scherrer equation (SE) and through Rietveld refinement (RR), and are reported in nm.

N	Sample	Initial analyses			Reproduced analyses		
		Size from peak 1 (SE)*	Size from peak 4 (SE)*	Size from RR*	Size from peak 1 (SE)	Size from peak 4 (SE)	Size from RR
1	Unused particles	46	26	37	46	24	35
2	5 h in air	51	29	47	46	31	47
3	5 h in air**	53	29	84	-	-	-
4	24 h in air**	50	29	70	49	29	48
5	45 h in air	44	25	36	48	28	43
6	19 h in H <sub>2</sub> (2.00 %)	44	27	41	44	30	44
7	19 h in H <sub>2</sub> (100 %)	-	-	-	45	24	34
8	19 h in N <sub>2</sub>	-	-	-	44	24	31
9	24 h in MeOH/H <sub>2</sub> O**	45	31	47	-	-	-
10	MTE, lab**	-	-	-	45	28	42
11	MTE, industry, top**	-	-	-	44	25	39
12	MTE, industry, bottom**	-	-	-	37	24	28
13	Unused net	60	51	41	-	-	-
14	45 h in air	60	51	120	-	-	-
15	Unused annular	-	-	-	51	46	102
16	Used annular**	-	-	-	54	46	93

\* Results from experiments that were performed for the specialization project autumn 2019.

\*\* These samples were obtained from a previous student and co-supervisor and were used for comparative analyses.

From Table 4.1, it is seen that the crystallite sizes calculated from peak 4 are smaller than for peak 1, and that the difference is smaller for the silver net and annular silver than the particles. This indicates that there is strain present in the samples, and that it is more severe for the particles. The strain could have occurred during production, but for the particle it could also have come from the crushing during sample preparation for XRD. It is further observed that the results from the Scherrer equation and the Rietveld refinement differs from each other.

This was expected since the latter includes both instrumental factors and strain in its calculations. By reproducing the diffraction patterns it was also seen that the calculation methods gives stable results, as the measured sizes are approximately unaltered. The Scherrer equation is as mentioned an approximation, and the sizes that are calculated from it are therefore treated as indications. The Scherrer constant of 0.89 is also applicable for spherical particles, and for a more accurate result a value for cubic particles should have been used. The Double-Voigt approach, performed through Rietveld refinement is also simplified, but as it includes the whole pattern in its calculations, these results are more reliable and it was therefore chosen to use these when discussing the changes seen in Table 4.1.

Another factor that could have affected the sizes are if the particles were not small enough after being crushed in the mortar. This could have led to a diffraction pattern that is textured, meaning that there is not enough particles to generate a representable pattern. In such cases it would be incorrect to employ functions correcting for preferred orientation, which is done in the calculations performed in this thesis. Preferred orientation was also employed when estimating the crystallite sizes of the net and annular silver, as the fit in the difference profile plot was not good enough prior to introducing the functions.

Complications with characterization of silver through XRD has been reported, and the problem is believed to be its coarse grain structure. There are therefore few estimates of the crystallite size of electrolytic silver in the literature [5]. A previous student has done similar experiments, including calculation of the crystallite size from the Scherrer equation. The sizes of unused silver particles, particles calcined in nitrogen for 24 hours and a 24 h methanol and water calcination, were 37.5, 37.9 nm and 37.9, respectively [32]. It is not specified which peak the sizes are calculated from, but it is however observed that they are in the same range as the results obtained from the experiments in this thesis.

The  $R_{wp}$ - and GOF-values visualize how good the fit in the Rietveld refinement is, and the values from the refinement performed in this thesis are presented in Table 4.2. It is seen that all  $R_{wp}$ -values, except for the net (entry 10 and 11), are above 10, and all GOF-values are relatively close to 1. This means that the fits can potentially be further optimized. The difference profile plots did however show that they were good enough for the calculations performed in this thesis, and the refinement was therefore stopped.



Table 4.2:  $R_{wp}$ - and GOF-values, from the Rietveld refinement, for the different samples.

N	Sample	$R_{wp}$ *	GOF*	$R_{wp}$	GOF
1	Unused particles	16.2	1.35	18.3	1.61
2	5 h in air	16.4	1.47	15.7	1.31
4	24 h in air**	17.3	1.30	16.5	1.38
5	45 h in air	17.0	1.44	16.9	1.47
6	19 h in H <sub>2</sub> (2.00 %)	16.1	1.32	17.5	1.44
7	19 h in H <sub>2</sub> (100 %)	-	-	19.2	1.68
8	19 h in N <sub>2</sub>	-	-	18.0	1.55
9	24 h in MeOH/H <sub>2</sub> O**	14.7	1.35	-	-
10	MTF lab**	-	-	15.9	1.34
11	MTF industry, top**	-	-	16.4	1.59
12	MTF industry, bottom**	-	-	15.2	1.27
13	Unused net	5.71	1.11	-	-
14	45 h in air	5.72	1.22	-	-
15	Unused annular**	-	-	10.4	1.71
16	Used annular**	-	-	11.8	1.69

\* Results from experiments that were performed for the specialization project.

\*\* These samples were obtained from a previous student and co-supervisor and were used for comparative analyses.

Based on the  $R_{wp}$ - and GOF values, the crystallite sizes from the Rietveld refinement should be reliable. However, they do not comply with the SEM images of the unused particles, which reveals sizes that are larger than the ones presented in Table 4.1. Per Erik Vullum at SINTEF did therefore perform focused ion beam (FIB) and transmission electron microscopy (TEM) on the particles delivered by K. A Rasmussen. The characterization was performed on a less faceted particle, and the result visualized a single crystal without grain boundaries, except for a thin twin, which means that the more faceted particles are probably also single crystals. Further, bright field TEM showed that there are inclusions and dislocations everywhere on the sample that destroys the lattice coherence. The distance between them are a few tens of nm, which means that these are the causes of the XRD peak broadening. None of the broadening for the unused particles is therefore because of the crystallite size, and the sizes presented in Table 4.1 represents the sizes between the inclusions and dislocations and not the entire particle. TEM was also performed on used particles (explained in Section 4.1.4.), and showed that their crystallite sizes complied with the sizes measured by XRD. This result suggests that the inclusions and dislocations destroying the lattice coherence of the unused particles, are not present when they are used, at these conditions. The sizes are however still estimations, and XRD characterization with a more advanced instrument could be used for more accurate results.

As the size of unused particles is unknown, the change in size can not be determined when particles are exposed to these conditions. Some trends can however be seen. Table 4.1 visualize that there are almost no changes in the crystallite sizes of the particles when exposed to the different conditions. This can be because the changes are more evident on the surface, and longer exposure might be required to detect changes when employing XRD, which is a bulk technique. There is a significant difference in size for the net, which can be because its diameter is smaller than the particles and annular, and the silver bulk could thereby be more affected by the conditions. The difference in size for the annular silver is also minor and can be because it has higher mechanical stability, where the silver bulk is not significantly affected by the conditions. XRD is also mainly used for powdered samples, and might not be an optimal characterization technique for the net and annular silver. As the diffusion and transport mechanisms in silver is not known, determination of the reason for the increasing and decreasing crystallite sizes could require more experiments. Further discussion of the changes in sizes for the different conditions are presented in the following subchapters.

Before conducting EBSD, two materials were tested for the grinding and polishing required to obtain a flat surface. The first sample were hot mounted in phenolic resin. When the approach presented in Table 3.6 was tested, this material did not sustain the particles, and most of the sample disappeared during the first step of the grinding. It was thereby observed that the phenolic resin was not suited for these conditions.

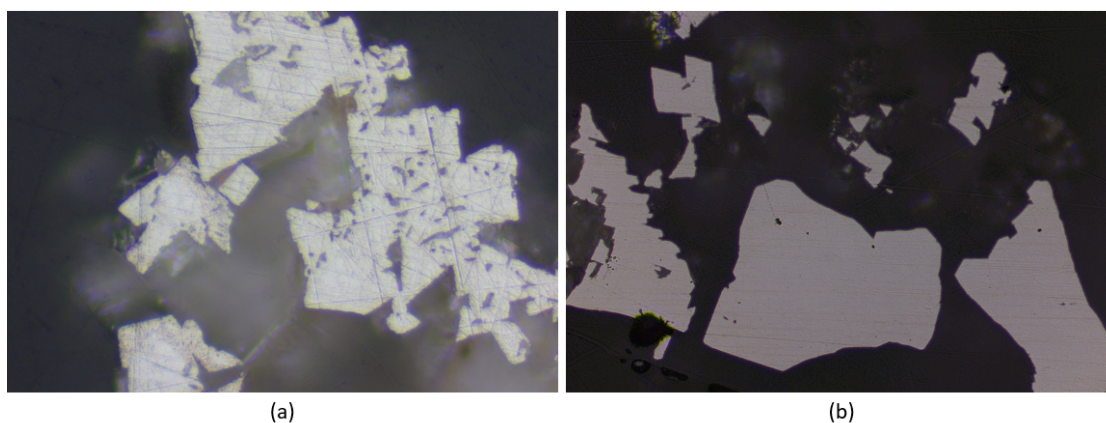


Figure 4.3: Images of unused silver particles, molded in epoxy, after first (a) and second (b) step of the polishing.

Before the grinding and polishing of the sample molded in epoxy was started, the force pushing the sample towards the surface was reduce by 5 N in every step. This was to ensure that the silver would not be grinded away, as it did for the hot mounted sample. After performing the first step of the polishing, the sample was studied in a light microscope. The images revealed that scratches were present on the surface of the sample, which confirmed that more polishing was necessary before conducting EBSD. After the final step of the polishing, an-

other analysis in light microscope was performed. Some scratches were still observed, but the quantity was less than after the former step. This could indicate that additional polishing is required before conducting EBSD, but it was however decided to perform a test. The images taken in the light microscope can be seen in Figure 4.3.

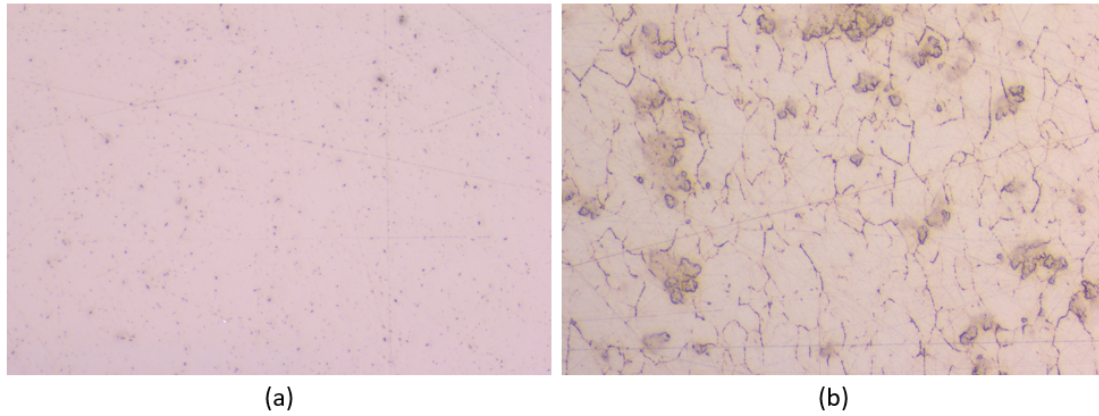


Figure 4.4: Light microscope images of annular silver grinded and polished to observe the surface (a) and the bulk (b).

An annular silver sample was cut in half and molded in epoxy with a goal of performing EBSD on both the silver surface and the bulk. The samples were grinded and polished using the same approach as the particles, and images taken in light microscope is presented in Figure 4.4. It is seen that the sample surfaces has scratches, similar to the particles, which is another indication that the approach in use is not good enough. The annular silver that were polished to observe the surface, were not polished enough and had too much epoxy above the silver. It was therefore decided to not perform further preparation of this sample. The remaining samples, were wrapped in aluminium foil and studied in SEM. SEM images of the molded particles (a) and annular silver (b) are presented in Figure 4.5.

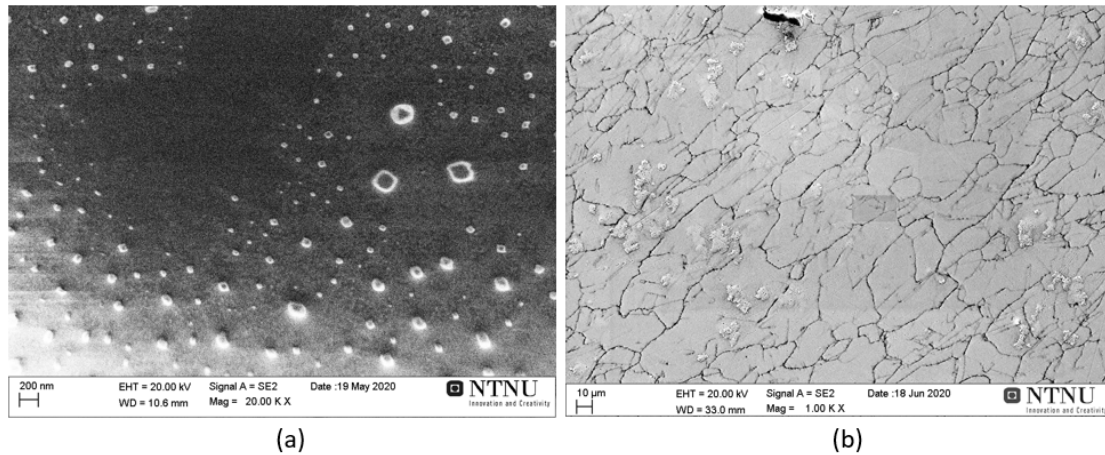


Figure 4.5: SEM images of unused particles (a) and annular silver (b), molded in epoxy.

When EBSD was conducted on the particles, the epoxy became unstable under the high-energy electron beam, and the sample was thereby unable to produce Kikuchi bands. An attempt to improve the stability was performed by adding another coating layer, with half of half carbon and gold. The sample became more stable, but was still unable to produce Kikuchi bands. As the unused particles are single crystals, it is possible that their weak signals could have been blocked by the coating. The scratches observed through light microscope could also have affected the signal, and adding vibration polishing to the approach could be a possible solution to remove them.

When analyzing the annular silver in EBSD, Kikuchi bands were observed, and images are presented in Figure 4.6. The signal is weak, but evident Kikuchi bands and zone axis can be seen. Because of the scratches inflicted during grinding and polishing, a crystal orientation map could not be constructed. It is thereby clear that the preparation approach in this thesis is not thorough enough to obtain a flat surface. Vibration polishing should be included in further work, and another solution could also be to perform ion milling on the samples. Due to the Corona situation, optimization using these approaches were not conducted.

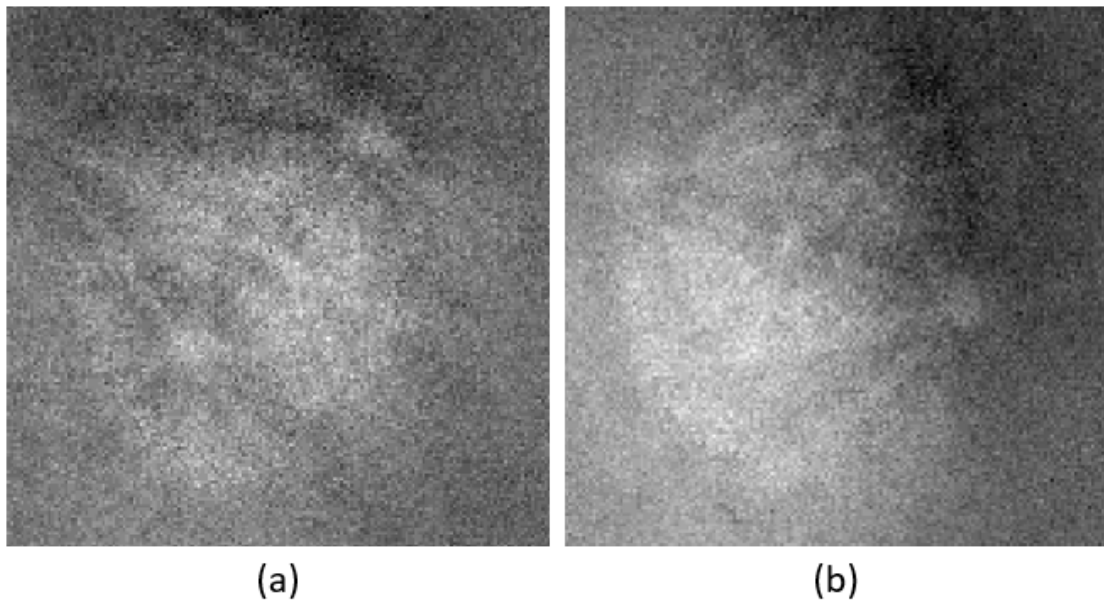


Figure 4.6: Images of Kikuchi bands from the bulk of unused annular silver.

#### 4.1.2. Oxygen Interactions

Oxygen is known to lead to restructuring of the silver surface, and to observe this effect it was decided to perform calcination experiments in air, on both the particles and the net. The diffractograms of these samples are compared to unused particles in Figure 4.7, where it is seen that the peak widths and positions remain approximately unaltered.

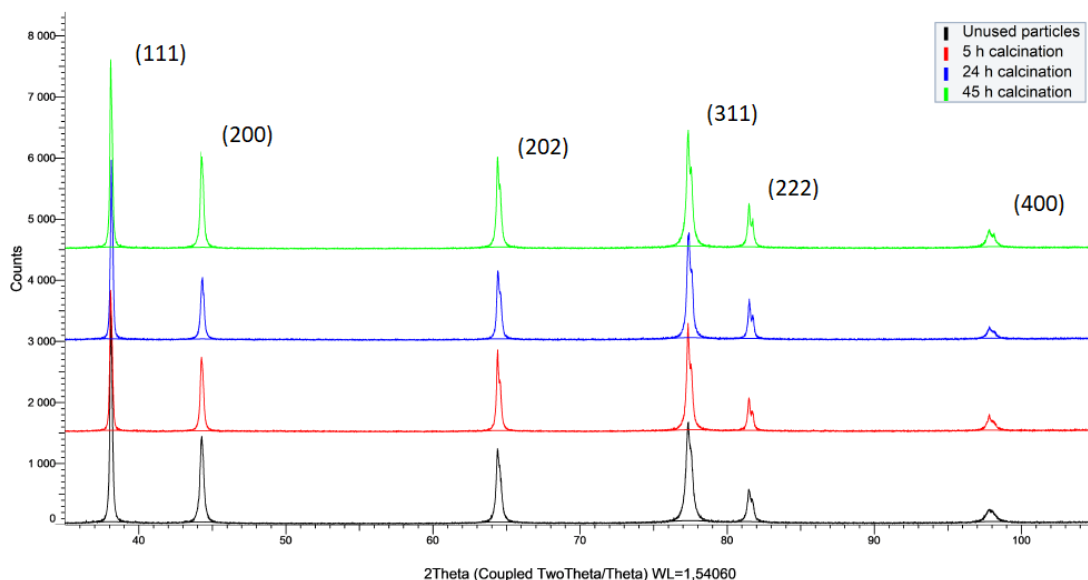


Figure 4.7: Diffraction pattern of particles calcined in air, at 650 °C for 5 to 45 h, compared to unused silver particles.

When comparing the crystallite sizes of the oxygen calcined particles (Table 4.1, entry 2-5), it is observed that there are almost no changes, but a trend can however be seen. The size increases from calcination for 5- to 24-hours, but between 24 and 45 hours it starts to decrease. The reason for the initial increase in size can be that aggregated silver incorporates oxygen and thereafter restructure to attain a thermodynamically favored structure, with densely packed surfaces, that lowers the surface free energy and increases the size. Increasing size in these conditions does also comply with literature [2]. The decrease in size can be due to stress and disruptions that over time leads to failure and reduction of the size. There are also theories of oxygen diffusing and substituting silver in the silver lattice, which eventually leads to a reduction of the size [11]. More experiments are however needed to determine the cause of the decreasing crystallite size. The sizes are, again, indications and more experiments and analyses should be conducted to determine if they give a reliable image of the differences. The size of the particles calcined for 24 h (Table 4.1, entry 4) decreased when the diffractogram was reproduced. This can be because the sample was prepared incorrectly prior to the first analysis, and had particles that were too large. It is also suspected that this is the reason for the large size estimated for the 5 h calcined sample (Table 4.1, entry 3).

SEM images of the particles after calcination in air for 5 and 45 hours are presented in Figure 4.8. These visualize that treating silver at high temperatures in air leads to severe changes of the morphology. This was as expected as oxygen is present at temperature above Tamman temperature. The changes are a result of oxygen dissolution which further leads to surface restructuring to attain a thermodynamically favorable structure. The morphological changes involve refaceting, smoothing and pinhole formation, and complies with litterature and previous experiments [2] [6]. These results also support that oxygen might be the cause of the pinhole formation, but more experiments are needed to determine the reason for their occurrence.

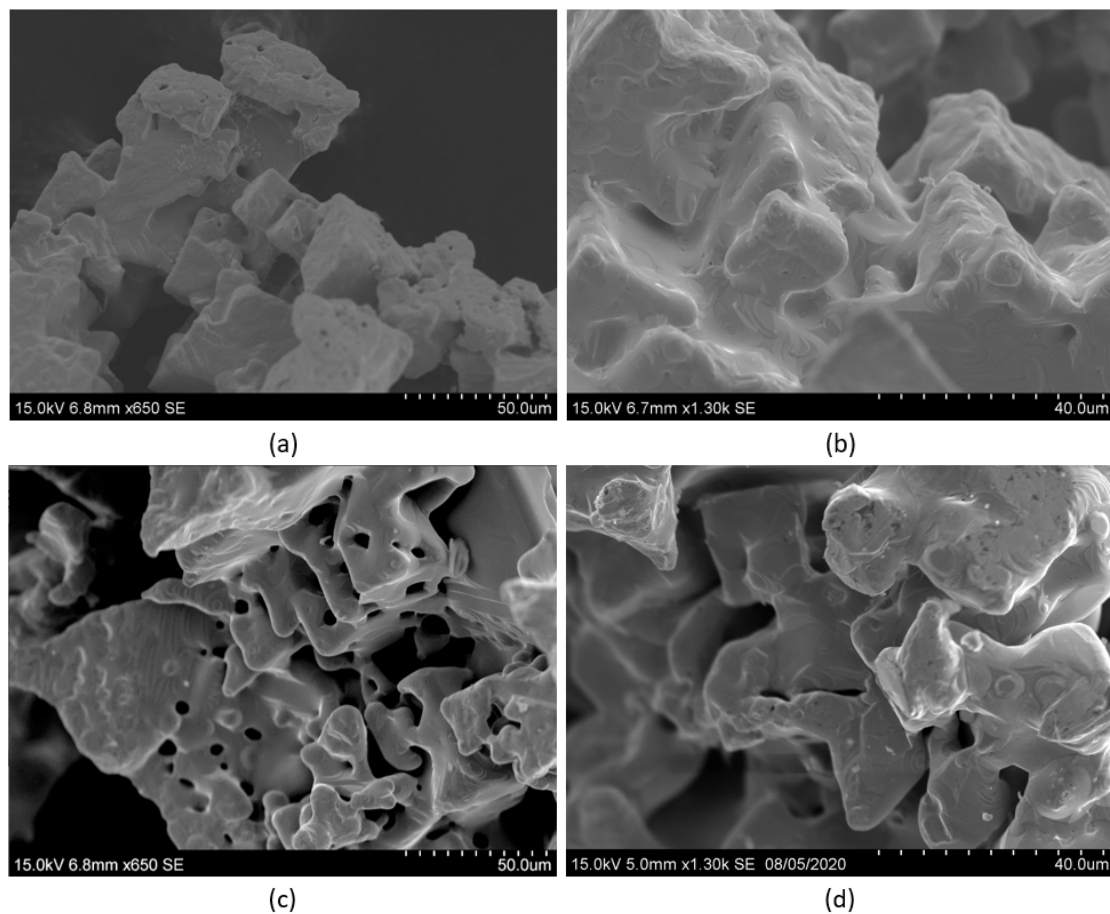


Figure 4.8: SEM images of particles calcined in air for 5 h ((a) and (b)) and 45 h ((c) and (d)) at 650 °C, at different magnifications.



To get an overview of the structural changes, and determine whether the hole formation increased with time, a systematic approach was conducted. This involved choosing four different locations on the relevant sample, and thereafter increase the magnification and take five pictures within the chosen area. By doing this it was seen that the changes were more extensive for the silver that were calcined for 45 hours. It is thereby observed that the morphological changes and the number of pinholes increases with time exposed in air, which also complies with previous experiments [5]. The images used for the systematical approach are attached in Appendix B.

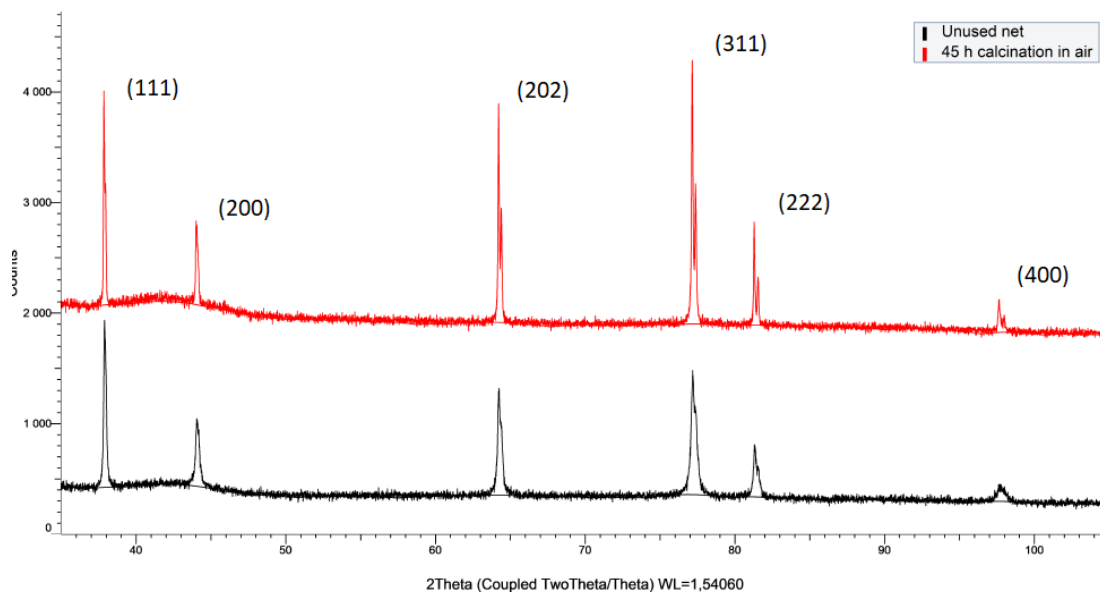
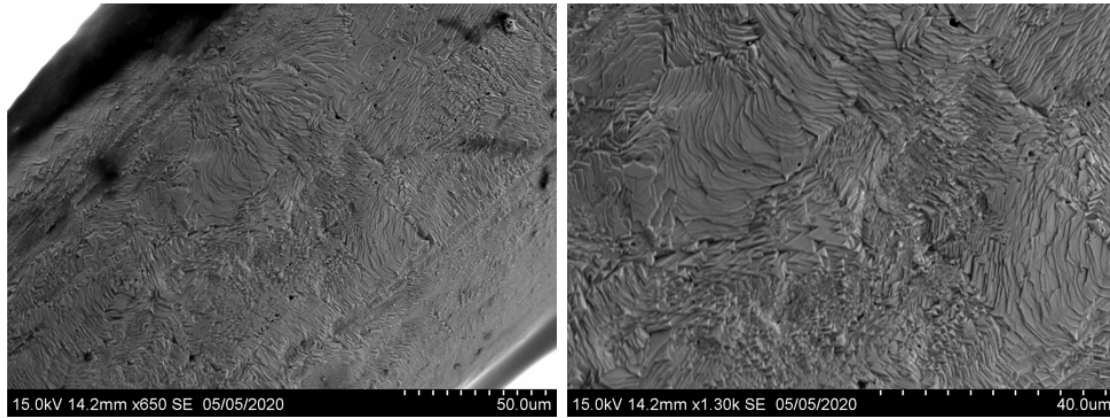


Figure 4.9: Diffactograms of unused silver net and net calcined in air for 45 h at 650 °C.

The crystallite sizes that were measured for the silver net (Table 4.1, entry 10 and 11), shows high dependence on the calculation method. When the Scherrer equation is employed, no change in size observed, while it is large when the Rietveld refinement has been performed. This can indicate that XRD, which is mainly used for powdered samples, might not be an optimal characterization technique for the net. The  $R_{wp}$  and GOF-values does however show that the fits in Rietveld refinement are relatively good and should give trustworthy results. A change in crystallite size when exposed to these conditions were also expected, and complies with literature [2]. The diffractogram of the calcined net (Figure 4.10) shows a difference in peak widths, compared to unused net, which can be due to phase restructuring in the bulk. This could also indicates that there are some changes in the crystallite sizes, as indicated by the Rietveld refinement.





(a)

(b)

Figure 4.10: SEM images of the net after calcined in air for 45 h. at 650 °C.

SEM images of the used silver net are presented in Figure 4.10. It is observed that these conditions led to severe restructuring of the surface by facet formation. There are minor indications of pinhole formation on the surface, but not to the same extent as for the particles. The restructuring is, as for the particles, a result of oxygen dissolution followed by surface restructuring to attain a thermodynamically favorable structure [2] [6]. The lack of pinhole formation was however unexpected and more experiments are needed to determine the reason for their absence.

#### 4.1.3. Hydrogen, Nitrogen and Methanol/Water Interactions

Since hydrogen is present as a product in the methanol to formaldehyde reaction, it was decided to analyze the effect it has on the silver morphology at both high and low concentration. In addition, a calcination experiment in nitrogen was performed to observe the temperature effect exclusively, as nitrogen is assumed to be inert towards silver. A sample that has been calcined in methanol and water for 24 h was also obtained from a previous student, and characterized for comparative analysis.

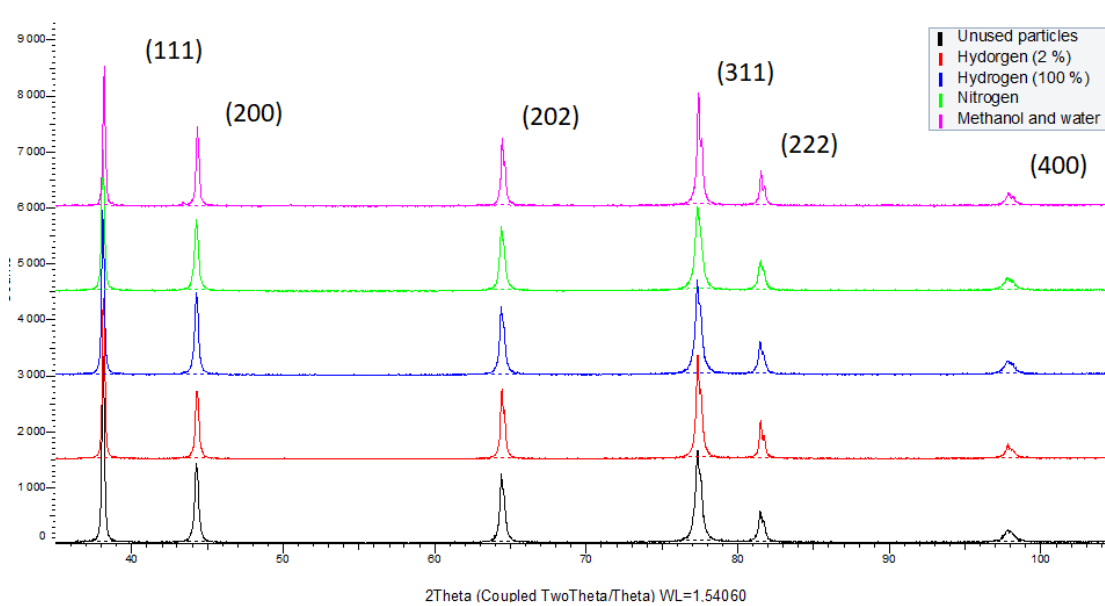


Figure 4.11: Diffractograms of particles calcined in hydrogen (2 % and 100 %) and nitrogen for 19 h, and methanol and water for 24 h, all at 650 °C.

The diffractograms of the samples are presented in Figure 4.11, where it is seen that the peak widths and positions remain approximately the same when exposed to these conditions. Further, it is seen that the crystallite sizes are also relatively similar (Table 4.1, entry 6-9). When employing the Rietveld refinement, the size of the particles exposed to lower hydrogen concentration (2 %) is larger than the 100 % hydrogen calcined sample. These differences are however assumed to be insignificant since neither the Scherrer equation or the Rietveld refinement has given accurate images of the crystallite sizes.

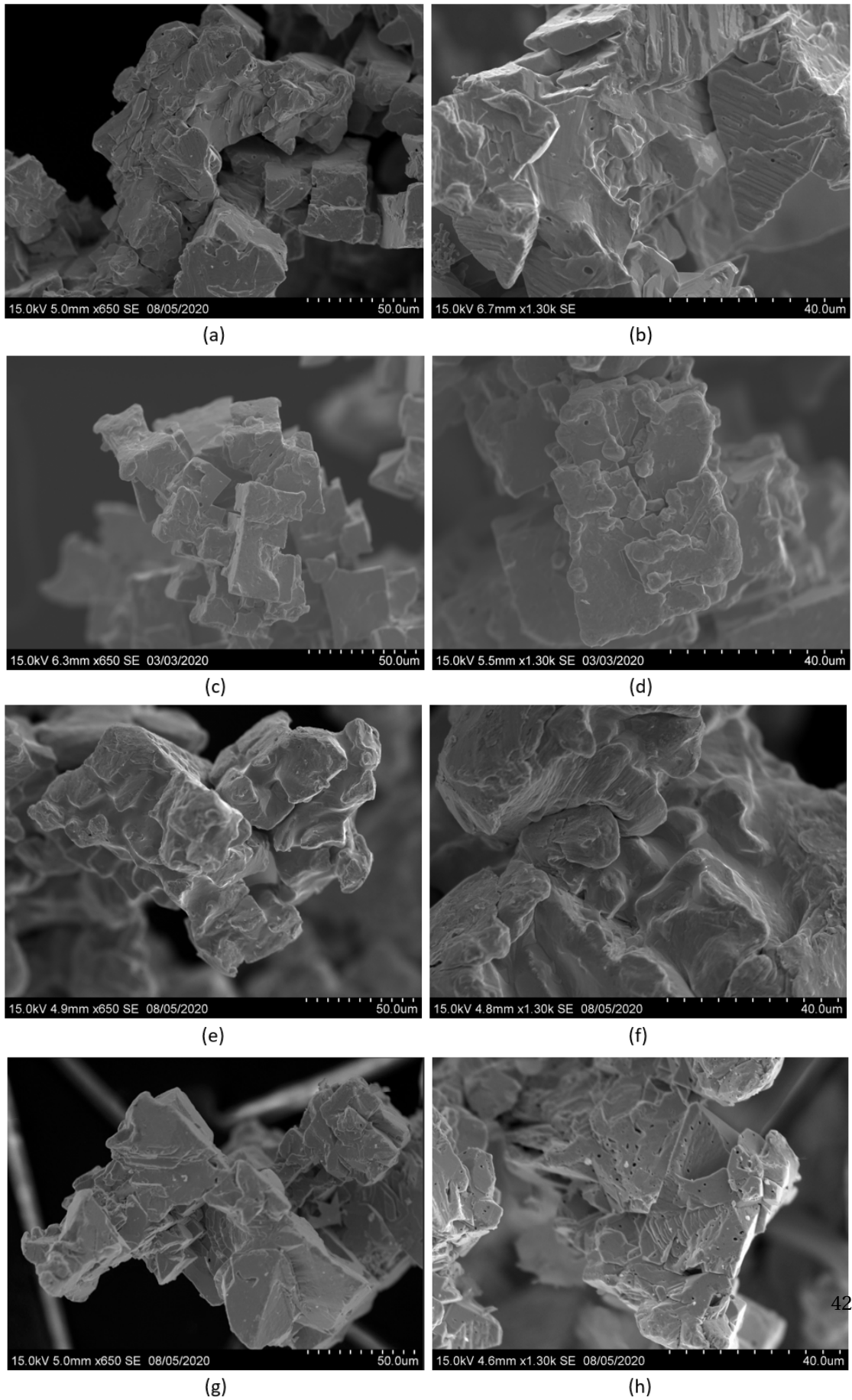


Figure 4.12: SEM images of particles calcined for 19 h in hydrogen at low (2 %) ((a) and (b)) and high (100 %) concentration ((c) and (d)), 19 h nitrogen ((e) and (f)), and 24 h in methanol and water ((g) and (h)), at different magnifications.

Figure 4.12 presents SEM images of the samples at different magnifications. From these it can be seen that the 2 % hydrogen sample have a faceted surface that is very similar to unused particles, and contains small pinholes. The 100 % hydrogen calcined sample is also very similar to unused silver, but has a more smoothed surface. The difference between these samples were unexpected, and could be a result of feed gas impurities or trace amounts of subsurface oxygen, that hydrogen might react with [5]. The images does however show that hydrogen alone can not activate the surface for the extensive restructuring that oxygen can. As the surfaces of these samples are very similar to unused particles, it also indicates that hydrogen can act as an inert towards silver at these conditions. More experiments with longer exposure should however be conducted to confirm this.

Images of the particles calcined in nitrogen visualize a smoothed surface that resembles the particles calcined in 100 % hydrogen. The smoothing observed on these samples were unexpected, and it could be possible that this difference only occurred on the small amount of sample that were analyzed. The methanol and water calcined particles resembles the surface of the unused particles and the hydrogen (2 %) calcined particles. This is another indication that atomic oxygen needs to be present for recrystallization to occur.

The surfaces of these samples have some differences, but these are insignificant in comparison to the severe restructuring that is observed on the samples calcined in air. Similar observations, in comparable conditions, have also been observed in previous analyses [5].

#### 4.1.4. Methanol Oxidation

Characterization of particles used for formaldehyde synthesis by a previous student, and in the industry were performed for comparative analysis. The former had a TOS of 48 h, total flow of 750 Nml/min, catalyst bed temperature of 642 °C and mol% CH<sub>3</sub>OH/H<sub>2</sub>O/O<sub>2</sub>/N<sub>2</sub> of 8/11/3/78. For the latter, particles from both the top and bottom of a silver bed, provided by K. A. Rasmussen and Dynea, were characterized. All the diffractograms are presented in Figure 4.13, where it is seen that the peak widths and positions remain approximately unchanged.

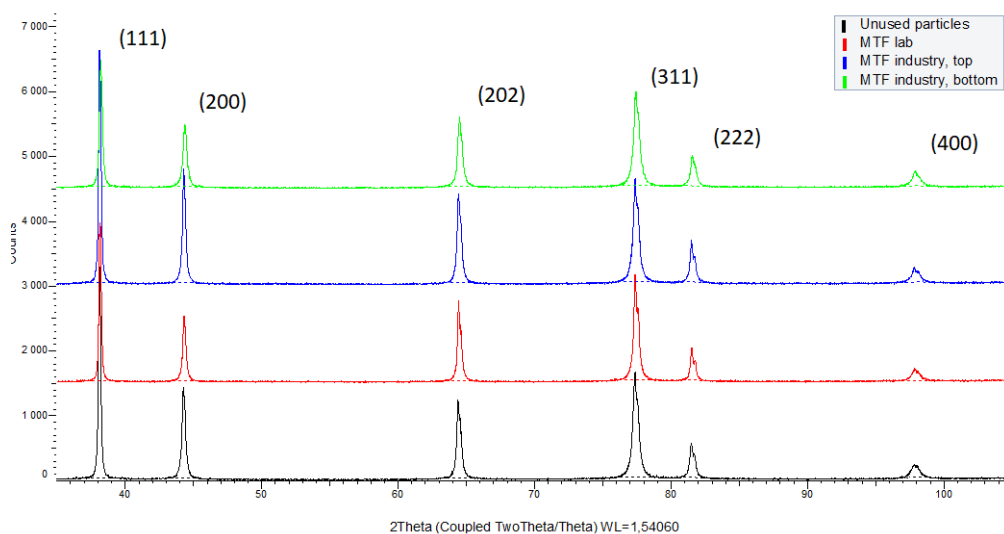


Figure 4.13: X-ray diffractogram of particles used for the MTF reaction in the lab and in the industry.

The particles used for formaldehyde synthesis in the lab has varying surfaces (Figure 4.14 (a) and (b)), which can be because the sample contain particles from various positions in the catalyst bed. Some particles are similar to the unused silver, while others contain pinholes and smoothed and recrystallized surfaces that are similar to the oxygen calcined samples. The restructuring is again a result oxygen dissolution followed by of lowering of the surface free energy, and complies with litterature and previous experiments [2][6]. The crystallite size (Table 4.1, entry 10), are similar to the air calcined samples, which indicates that there could be some changes when exposed to these conditions. Pinhole formation is also observed on both samples used for formaldehyde synthesis in the industry, but extensive refacetting and surface smoothing is only seen on the particles from the top layer. It is clear that they have been exposed to rougher conditions than the bottom layer, where the particles are relatively similar to the hydrogen and nitrogen calcined particles (see Figure 4.12). The crystallite sizes (Table 4.1, entry 11 and 12) are small, which was unexpected as they have been exposed to rough condition for a long time.

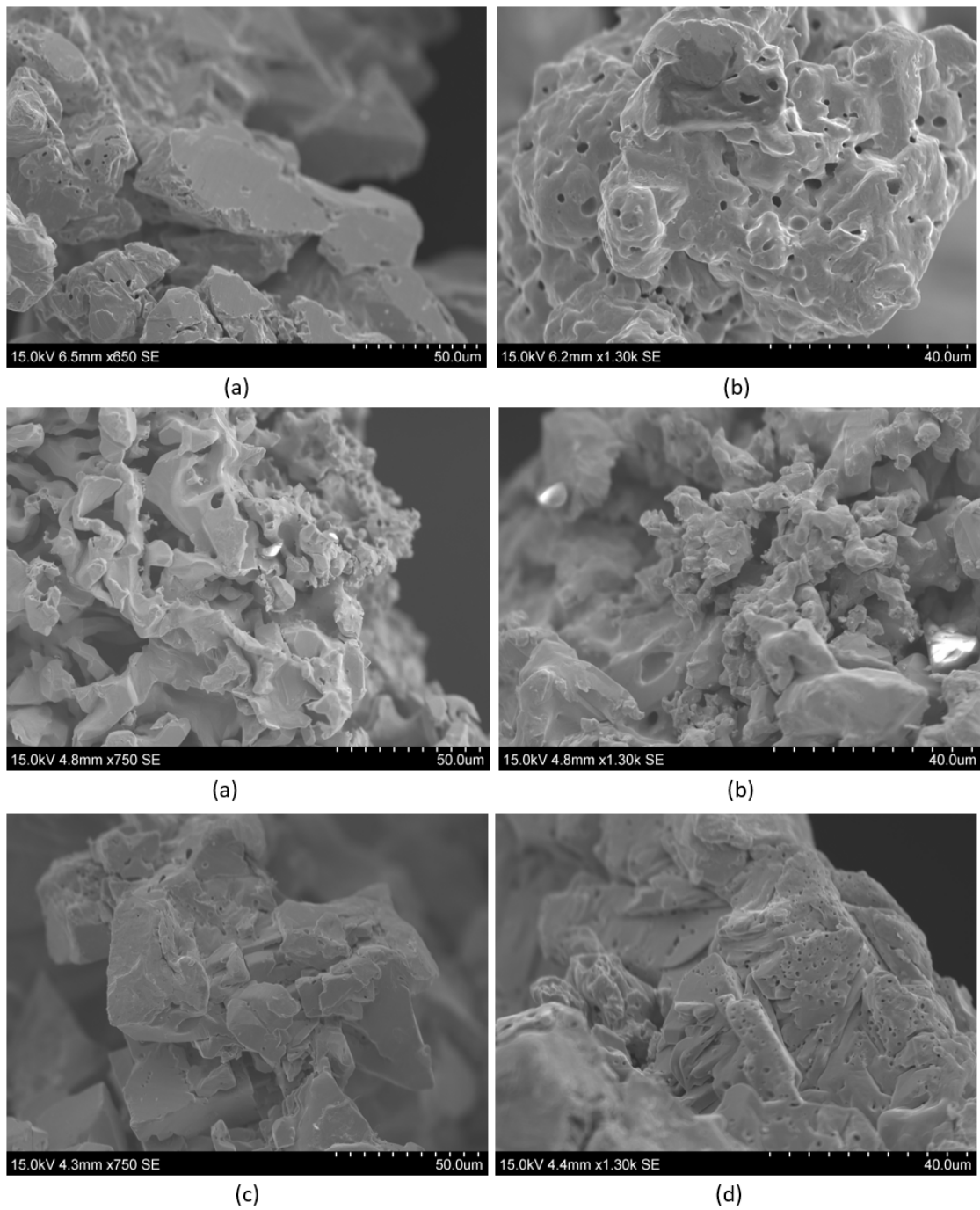


Figure 4.14: SEM images of particles after methanol oxidation ((a) and (b)), with a catalyst bed temperature of 642 °C and TOS of 48 h, and the top ((c) and (d)) and bottom ((e) and (f)) layer of the catalyst bed used for methanol oxidation in the industry.

Per Erik Vullum performed TEM on one particle used for formaldehyde synthesis in the lab and one from the top layer in the industry. The results showed the samples are very similar, and that both has transformed into an unknown oxide. As both samples are old, it is not unlikely that they could have oxidized, and there are also theories of oxygen being trapped in the silver structure [11]. The diffraction patterns from XRD were checked for signs of silver oxides, but this could not be found. The color of the particles does also indicate that the samples are pure silver, as silver oxides would have a dark brown/black color. TEM further shows that the crystallite sizes are between 10-50 nm and 5-30 nm for the lab and industry exposed particles, respectively, which complies with sizes calculated in this thesis. These results indicate that the defects destroying the lattice coherence of the unused particles are not present in the used particles, making these sizes more reliable. However, the XRD characterization in this thesis were employed on a routine instrument, and a more advanced instrument should be used when employing the Rietveld refinement.

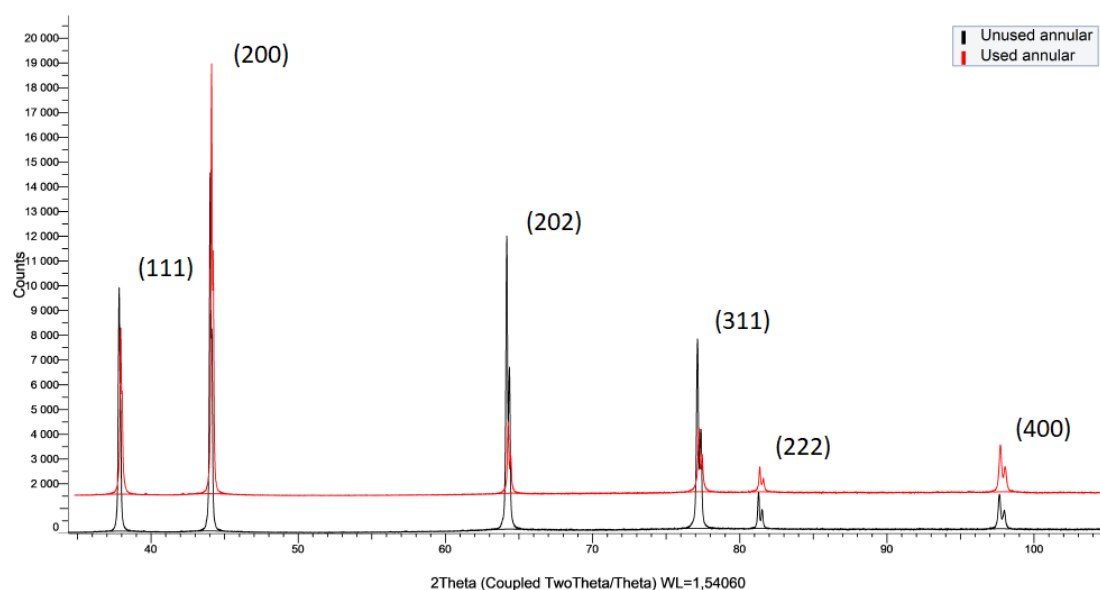


Figure 4.15: X-ray diffractogram of used and unused annular silver.

Annular silver used for several MTF reactions at temperatures between 570-690 °C and TOS from 1-15 days were obtained from a previous student [33], and characterized in SEM and XRD. The diffractogram of the sample is compared to unused annular silver in Figure 4.15, and it is observed that the peak widths remain approximately unaltered. Table 4.1, entry 15 and 16, shows that there is a small change in size between these samples. As the used annular sample has been exposed to rough conditions, this result indicates that the annular silver has high mechanical stability. The small change in size could be a result of recurring stress and disruptions from the reactions, or possibly oxygen substituting for silver in the lattice [11]. SEM images of the used catalyst at different magnifications are presented in Figure 4.16. It is evident that the catalyst has been exposed to rough conditions, and has restructured to a

smoothened surface with extensive pinhole formation. This result complies with the literature, and occur because of oxygen dissolution followed by recrystallization to a thermodynamically favored structure.

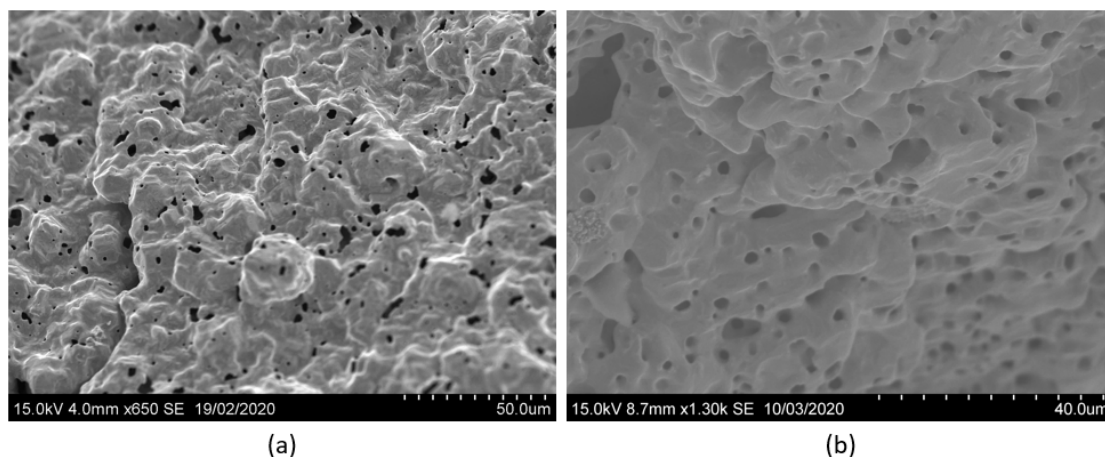


Figure 4.16: SEM images of annular silver used for several MTF reactions at temperatures between and TOS from.

Two methanol oxidation experiments were performed with a goal of determining if external mass transfer limits the MTF reaction, and more details are presented in Section 4.2. The images in Figure 4.17 visualizes the annular silver after the first ((a) and (b)) and second ((c) and (d)) helium experiment. It is observed that both the samples has undergone severe restructuring, compared to unused annular silver seen in Figure 4.2. The surfaces are very similar, and contain pinholes and highly corrugated surfaces, with protrusions, as a result of reduction of the surface free energy. The correlations to catalytic activity can be seen in Section 4.2.

Four annular silver samples used for methanol oxidation in nitrogen were also received from co-supervisor. The conditions are the same as the experiments performed in this thesis, except for the inert gas, and they were exposed to different temperatures; 540, 560, 580 and 600 °C. The samples were characterized in SEM with a goal to observe the temperature effect on the topology. All samples has, like the helium samples in Figure 4.17, undergone restructuring by formation of pinholes and highly corrugated surfaces with protrusions. Further, it can be seen that silver exposed to the lowest temperature (Figure 4.18, (a) and (b)) is less restructured than the remaining. On the sample exposed to 560 °C ((c) and (d)), protrusions are observed on large parts of the surface. At 580 °C ((e) and (f)) more of these protrusions are formed and on parts of the surface and they have migrated into larger protrusions with terraces, steps and kinks. A large amount of these defects are also observed on the surface of the sample exposed to the highest temperature ((g) and (h)). It is also observed that the surface of this sample is very similar to the annular silver used for methanol oxidation in helium. As the morphology differs for the four samples, it is clear that varying temperature, under otherwise



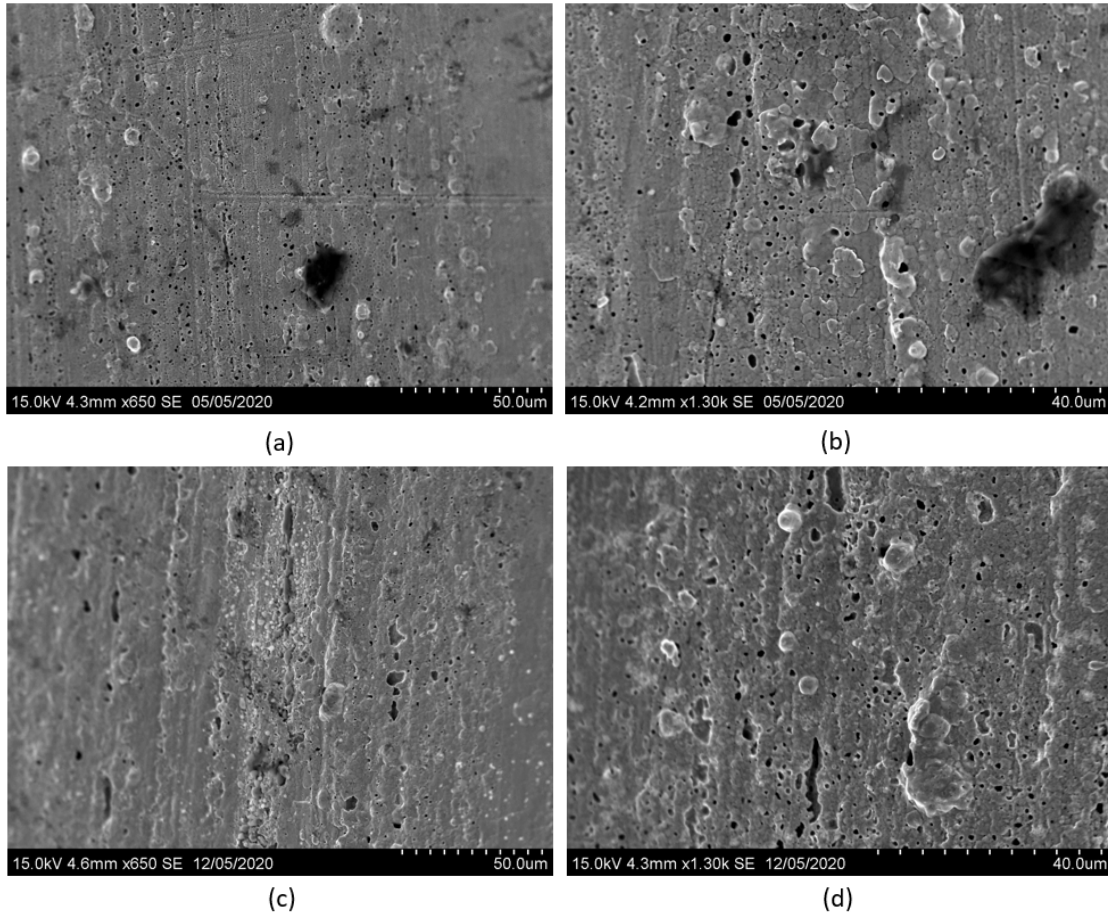


Figure 4.17: SEM images of annular silver after methanol oxidation in helium. The top images ((a) and (b)) represents the first experiment, and the bottom ((c) and (d)) the second experiment. Both were performed at 600 °C with an initial flow rate of 250 Nml/min. The component flows can be seen in Table 3.3.

equivalent exposures has an effect. The correlations to activity are presented in section 4.2.

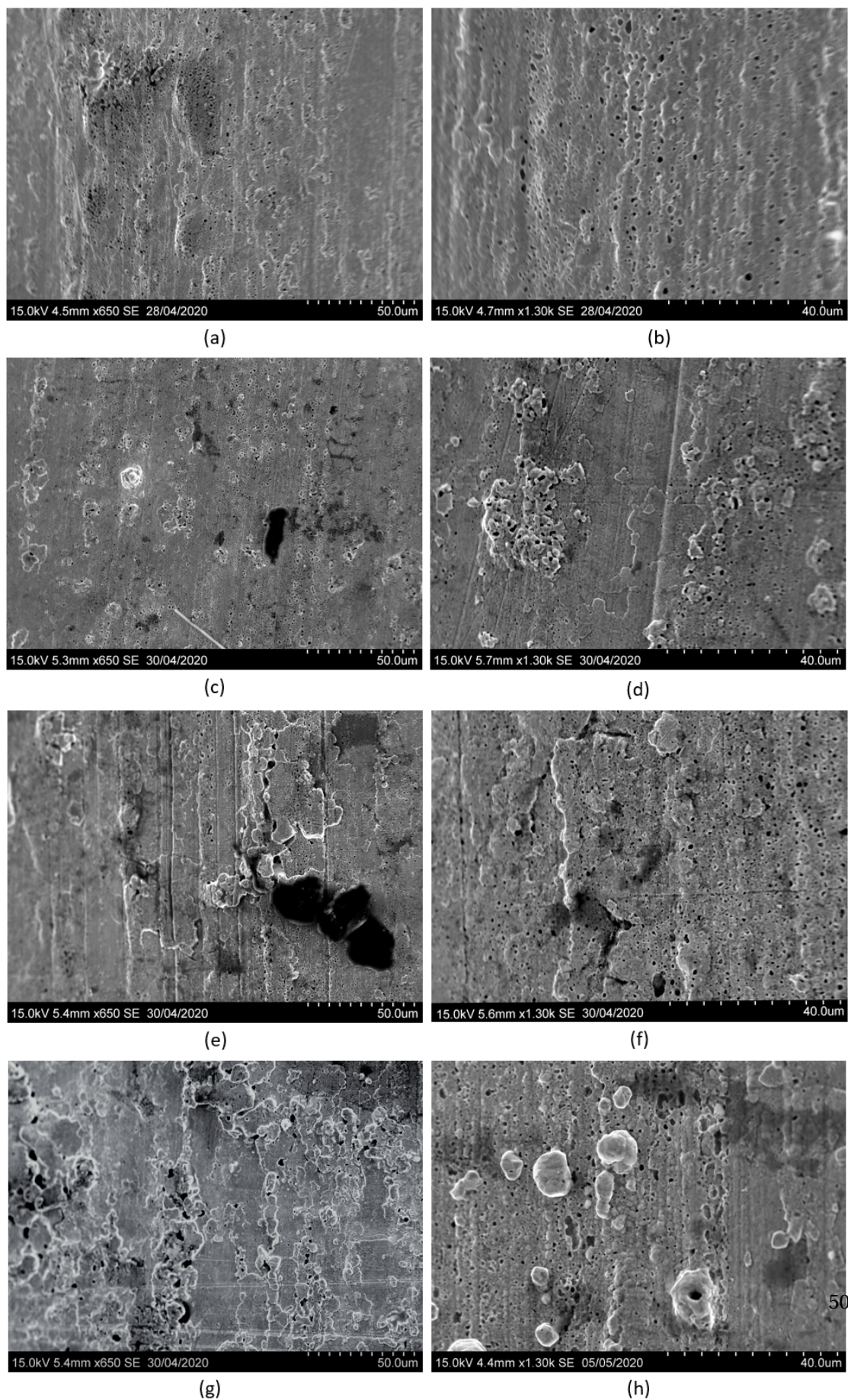


Figure 4.18: SEM images of annular silver after methanol oxidation in nitrogen at 540 °C ((a) and (b)), 560 °C ((c) and (d)), 580 °C ((e) and (f)) and 600 °C ((g) and (h)).

## 4.2. Catalytic Activity

Two methanol oxidation experiments were performed with a goal of determining if the MTF reaction is limited by external mass transfer limitation. The plan was to perform two identical experiments in different inert gases; helium and nitrogen. During the first experiment, problems with the LabView software caused half of the results to be based on nitrogen calibration instead of helium. This led further to higher inert concentration in the feed, and the results are thereby not comparable. It was therefore decided to conduct another experiment in helium, and compare it to co-supervisor Stine Lervold's results for an identical experiment diluted in nitrogen. A disadvantage with using helium as inert gas is that its peak in GC overlaps with hydrogen. The amount of hydrogen in the system is therefore unknown, and hydrogen and water selectivity can not be determined. This can be solved by optimizing the separation of hydrogen and helium, or by employing a different inert gas.

The conversions and selectivities from the three experiments are presented in Figure 4.19. The results from the two helium experiment are very different, showing an unexpected difficulty in reproducing experiments. There is a difference of almost 30 % between the initial methanol conversions, which increases to almost 50 % after 4 days. The catalyst bed temperatures are plotted versus TOS in Figure 4.20, where it can be seen that the second helium experiment reached higher temperatures than the first. Because of the calibration reset that occurred during the first helium experiment, the helium concentration for the last 48 h were higher than expected, and these results are therefore not comparable to the second experiment. The initial difference in conversions can be because the second helium experiment initiated faster than the first, resulting in higher temperature that further lead to quicker rearrangement of the silver surface. The rearrangement leads to a surface that is able to incorporate more oxygen and thereafter increase the conversions [2]. As this is an exothermic reaction, higher conversion leads to higher temperature, which also can be seen from Figure 4.19 and 4.20, where the conversions increase with increasing temperature. Higher temperature for methanol oxidation in helium than nitrogen has also been observed in previous experiments [18].

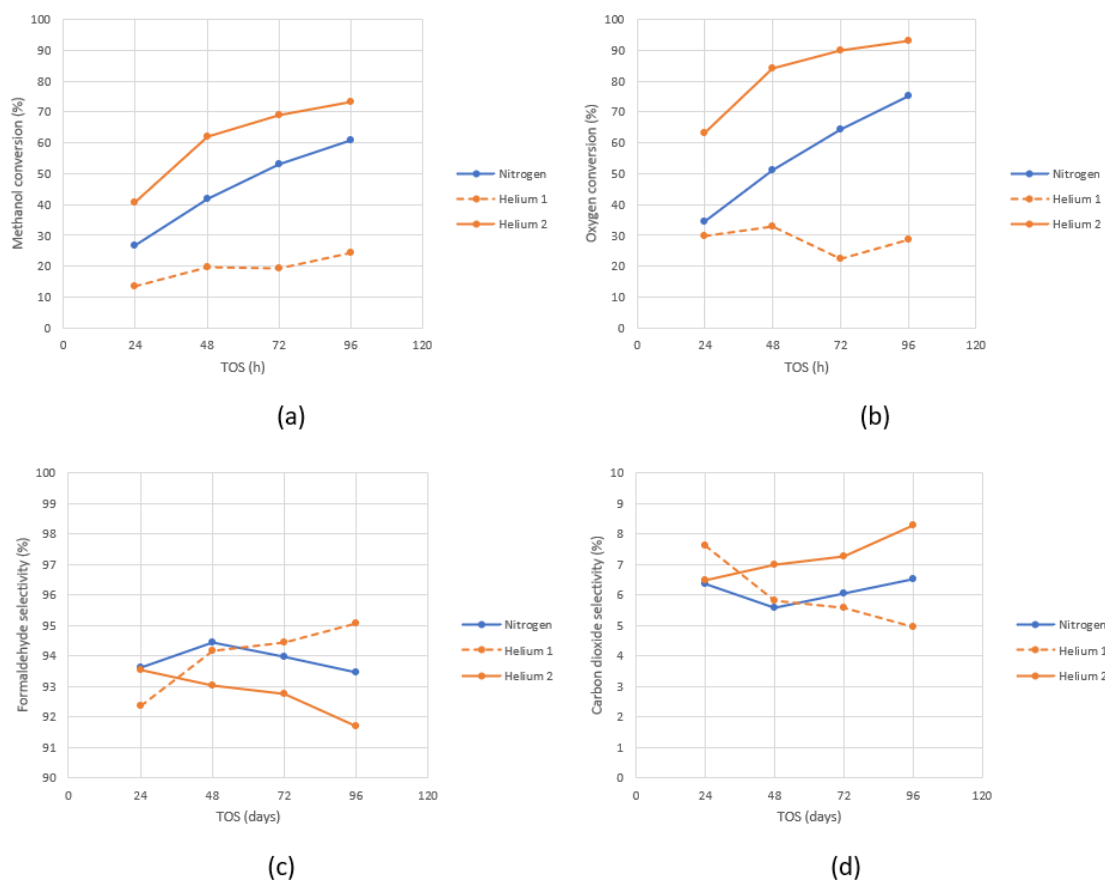


Figure 4.19: Methanol (a) and oxygen (b) conversion, and formaldehyde (c) and carbon dioxide (d) selectivity for the three methanol oxidation experiments plotted versus TOS. All experiments were performed with an inlet flow of 250 Nml/min at 600 °C and with a TOS of 4 days. Two were diluted in helium, and the last in nitrogen.

The different results for the two helium experiments are however unexpected and could have been affected by installation of the catalyst and the reactor. In addition, the methanol and water container was refilled before the second experiment, and the liquid level in the water seal was high during this experiment. Both these factors could have affected the results, and the latter could have caused some of the product to evaporate and participate in the reaction. Another way of performing these experiments could be to install a switch valve in the set-up. It would then be possible to change inert gas during the experiment, and switching when the reaction has stabilized could give more reliable results.

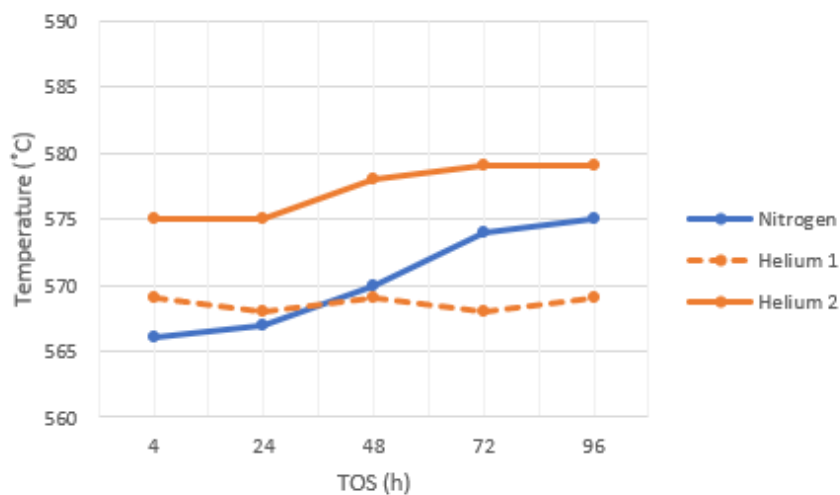


Figure 4.20: Catalyst bed temperature for the three methanol oxidation experiments plotted versus TOS. All experiments were performed with an inlet flow of 250 Nml/min at 600 °C and with a TOS of 4 days. Two were diluted in helium, and the last in nitrogen.

In the second experiment performed in helium, the conversions are observed to increase with TOS, which is as expected because of the dynamic silver surface. High oxygen conversion can however favor complete oxidation of methanol to carbon dioxide and thereby lead to a reduction of the formaldehyde selectivity. From Figure 4.19 it is seen that the selectivity towards formaldehyde, for the second helium experiment, decreases with TOS, while it increases for carbon dioxide. This is as expected, and does also comply with the literature [6] [7], and thereby indicates that the results from this experiment are reliable. More experiments should however be conducted to confirm this. The first helium experiment has the highest formaldehyde selectivity, showing that lower oxygen conversion is more favourable in this system.

The results from the nitrogen experiment differs from both the helium experiments. Since oxygen diffusion could be the rate determining step, these results indicate that oxygen diffuses faster in helium, which has also been shown by modeling the diffusivities [18]. These results could indicate that there are external mass transfer limitations in the system. However, because of the difficulty of reproducing experiments this can not be determined without another experiment in helium.

From the SEM images of the annular silver after the three methanol oxidation experiments (Figure 4.17 and 4.18), it is seen that the surfaces are similar, despite their different activities. This could be because the reaction is dependent on changes occurring below the detection limit of SEM, and the images are also limited by the resolution of the instrument.

Adjustment of total flow and oxygen concentration in feed was also performed, and the results are presented in Figure 4.21. The results of the first helium experiment is presented in Appendix D, as they are not comparable to the remaining results. These results show that decreasing the total flow does not have a significant effect on the conversions, while increasing it leads to a reduction in both methanol and oxygen conversion. Since low residence time can mean that the reactants does not have enough time to react, these results are as expected. The selectivities are approximately independent on the changes in total flow, which means that the formation of one of the carbon products is not dependent on the formation of the other. When the oxygen content in the feed was reduced, the methanol conversion was also reduced and the formaldehyde selectivity increased. Increasing the oxygen content had the inverse effect, with increased methanol conversion and carbon dioxide selectivity and reduced oxygen conversion and formaldehyde selectivity. This does again show that too high oxygen concentration will favor complete oxidation to carbon dioxide [6] [12]. The results from the nitrogen and the second helium experiment also deviate from each other, and thereby indicates, again, that external mass transfer limit the reactions.

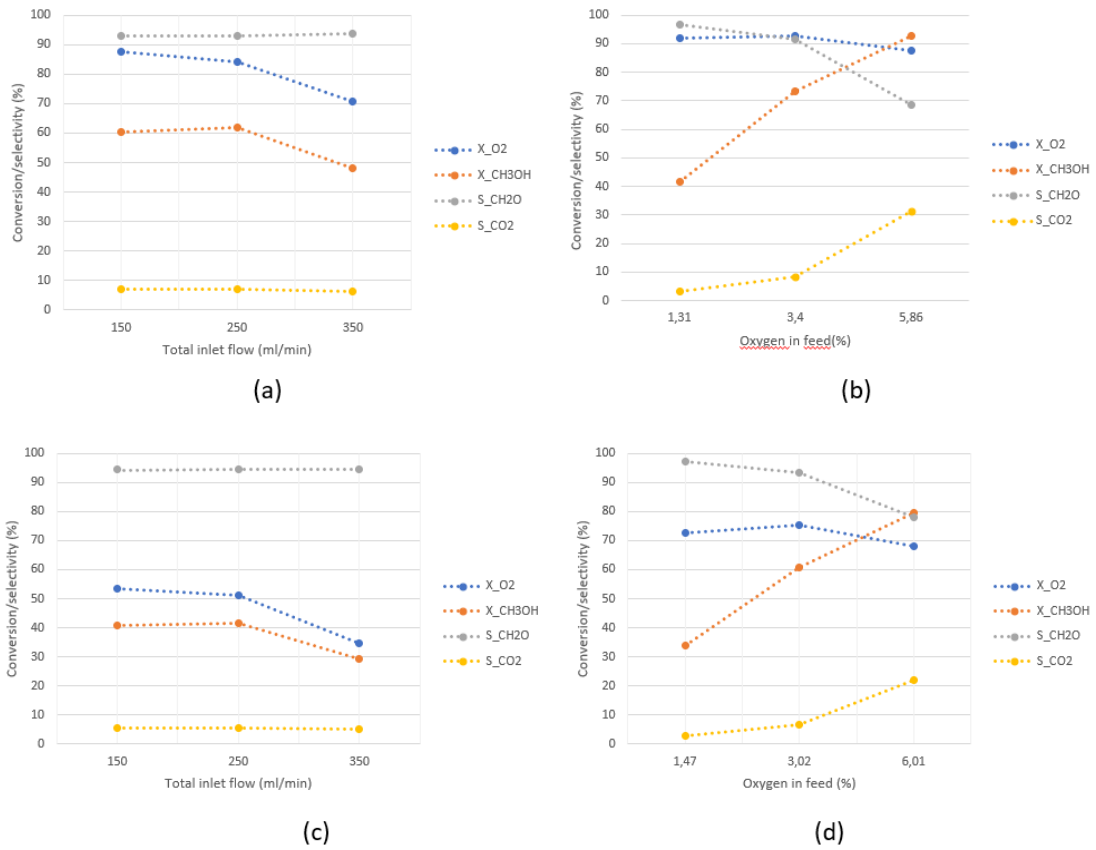


Figure 4.21: Conversion and selectivity results for adjustment of total flow and oxygen concentration in feed, for the second helium ((a) and (b)) and the nitrogen ((c) and (d)) experiment.



To validate the mass balance, the carbon error from the experiments were calculated. In Figure 4.22 the average error is plotted versus methanol conversion for all three methanol oxidation experiments. The negative number implies that the GC underestimates the amount of carbon out of the system. From the figure it is seen that the error is above 5 % for both helium experiment, and it increases with methanol conversion. This affects the activity calculations, and the selectivities that were presented in this section were therefore calculated by employing Equation 2.21.

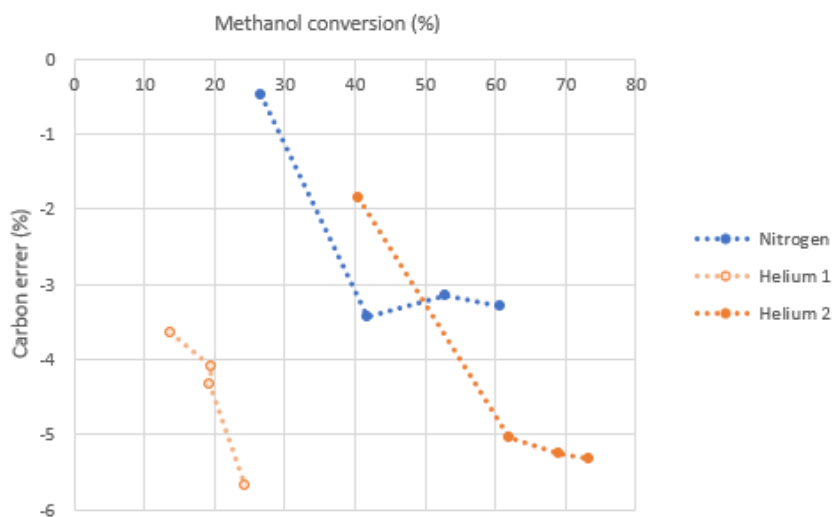


Figure 4.22: Carbon error plotted versus methanol conversion for the three methanol oxidation experiments.

The results from the four methanol oxidation experiments performed by co-supervisor are presented in Figure 4.23. These figures show that the different temperatures does have an effect on the system, and results in different activities. Three of the experiments, 560, 580 and 600 °C, have methanol conversions that follows the same trend, where it increases with increasing TOS. The experiment performed at the lowest temperature, did however result in a methanol conversion that remained unchanged with increasing TOS. From the SEM images in Figure 4.18 it was also observed that this sample has less defects than the remaining. This means that methanol oxidation at a reaction temperature of 540 °C does not activate silver for a restructuring that increases the oxygen incorporation. The conversions will thereby remain unchanged, leading to high formaldehyde selectivity. It could also be possible that another reaction mechanism is involved at this temperature. Further, it is seen that the conversions of the remaining experiments increases with increasing reaction temperature. This does also comply with the SEM images in Figure 4.18 where a difference in restructuring of the surface is observed.

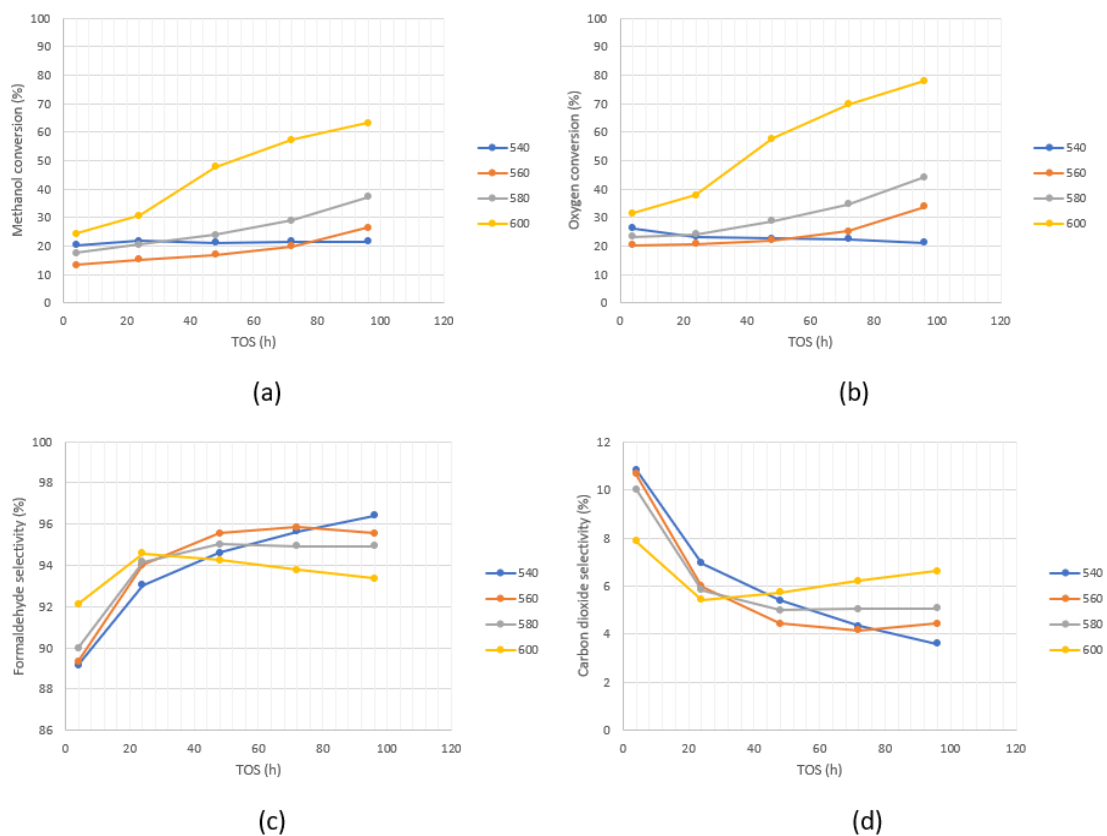


Figure 4.23: Catalytic activity for the four annular silver samples used for formaldehyde synthesis in nitrogen. All samples were exposed to a TOS of 96 h and total inlet flow of 250 Nml/min. The temperatures were 540, 560, 580 and 600 °C.

## 5. Conclusion

The MTF reaction has become an important process due to the versatile applications of formaldehyde. The silver catalyst has a dynamic surface that restructures under the industrial conditions, which also affect its catalytic activity. Three silver catalysts were studied in this thesis; particles, net and annular. Their morphological differences were characterized, before and after exposure in conditions relevant to the MTF reaction, and eventual mass transfer limitations during reaction were investigated. The motivation was to contribute to a better understanding of the MTF system and the silver interactions in these conditions.

The silver morphology were characterized in SEM, EBSD and XRD. The latter confirmed highly crystalline fcc silver, and showed that the annular silver were more crystalline than the particles and net. The EBSD results did also comply with this, as Kikuchi bands were visible for the annular sample and not the particles. A crystal orientation map of the annular silver were not constructed due to scratches on the surface. The goal of developing a grinding and polishing approach for EBSD was thereby not achieved. More optimization is required, and vibration polishing or ion milling are possible solutions. XRD were further used to measure the crystallite sizes of the samples, through both the Scherrer equation and the Rietveld refinement. The results from the latter was considered more reliable, and the difference profile plot and R-values support reliable results. However, TEM showed that the unused particles are single crystals, and that they have defects that destroys the lattice coherence and leads to incorrect measurement of the crystallite size. The changes in crystallite sizes for the particles could therefore not be observed. TEM does however suggest that these defects are destroyed when the particles are used, and that the sizes then represents the particles. Comparison of the used silver particles could therefore be performed, but the sizes are treated as indications. XRD characterization employing a more advanced instrument should be performed for more accurate results.

The catalysts were exposed to conditions with different TOS, temperature and atmospheres, and were compared to samples used by previous students. In general, the changes in crystallite sizes for the particles and annular silver when exposed to these conditions were small, and are concluded not to change. For the former, this can be because the time of exposure were not long enough for the silver bulk to be affected, and the latter could have higher mechanical stability as a result of its structural difference from the particles. The change in crystallite size is larger for the net, which can be due to structural differences leading to the bulk being more easily affected by the conditions. XRD is also mainly used for powdered samples, meaning that it could not be an optimal characterization technique for the net and annular silver.

Extensive restructuring of the surface is seen on samples calcined in air, and used for formaldehyde synthesis. The changes complies with the literature and are a result of oxygen incorporation followed by restructuring to attain a thermodynamically favored structure. On the particles and annular silver, pinholes have also been formed. These were not observed on the net, which is another indication that there are structural differences between the samples. On

the oxygen calcined particles, the amount of pinholes are observed to increase with increasing TOS. Characterization in TEM did further show that the particles used for formaldehyde synthesis, both in lab and industry, had oxidized to unknown oxides, and that their crystallite sizes complied with the ones measured in XRD. The surfaces of particles exposed to hydrogen, nitrogen and methanol and water atmospheres are relatively similar to unused particles. This indicates that, at these conditions, they acts as inerts towards silver and that atomic oxygen is needed for severe restructuring to occur.

Two methanol oxidation experiments, over annular silver, were performed in helium and compared to an identical experiment in nitrogen. The results of the two helium experiments were very different, and both differed from the nitrogen experiment. This could indicate that there are mass transfer limitation in the system, but because of the difficulty of reproducing results, another experiment diluted in helium should be conducted. SEM showed that the surfaces of all three samples are similar, with extensive restructuring and protruding defects. By characterizing annular silver used for formaldehyde synthesis at different temperatures, in nitrogen, it was observed that the restructuring increases with temperature. As expected, the reaction at the highest temperature also had the highest catalytic activity.

## References

- [1] G. J. Millar, M. Collins (2017), "Industrial Production of Formaldehyde Using Polycrystalline Silver Catalyst", *Industrial and Engineering Chemistry Research*, vol 56, no. 33 pp. 9247-9265
- [2] A. Nagy, G. Mestl (1999), "High temperature partial oxidation reactions over silver catalysts", *Applied Catalysis A: General* 188.
- [3] A. W. Franz, H. Kronemayer, D. Pfeiffer, R. D. Pilz, G. Reuss, W. Disteldorf, A. O. Gamer, A. Hilt (2016), "Ullmann's encyclopedia of industrial chemistry, formaldehyde".
- [4] J. A. Moulijn, M. Makkee, A. E. Van Diepen (2013), "Chemical Process Technology", WILEY, Second Edition.
- [5] S. Lervold, K. Arnesen, N. Beck, R. Lødeng, J. Yang, K. Bingen, J. Skjelstad, H. J. Venvik (2019), "Morphology and Activity of Electrolytic Silver Catalyst for Partial Oxidation of Methanol to Formaldehyde Under Different Exposures and Oxidation Reactions", Springer, <https://doi.org/10.1007/s11244-019-01159-0>.
- [6] M. Qian, M. A. Liauw, G. Emig (2003), "Formaldehyde synthesis from methanol over silver catalysts", *Applied catalysis A: General* 238.
- [7] G. I. N. Waterhouse, G. A. Bowmaker, J. B. Metson (2004), "Mechanism and active sites for the partial oxidation of methanol to formaldehyde over an electrolytic silver catalyst", *Applied catalysis A: General* 265.
- [8] I. Chorkendorff, J. W. Niemantsverdriet (2013), "Concepts of Modern Catalysis and Kinetics", WILEY, Third Edition.
- [9] K. K. Kolasinski (2012), "Surface Science: Foundations of Catalysis and Nanoscience", John Wiley & Sons.
- [10] G. I. N. Waterhouse, G. A. Bowmaker, J. B. Metson (2003), "Oxygen chemisorption on an electrolytic silver catalyst: a combined TPD and Raman spectroscopic study", *Applied Surface Science* 214.
- [11] A. Nagy, G. Mestl, T. Rühle, G. Weinberg, R. Schlögl (1998), "The dynamic restructuring of electrolytic silver during the formaldehyde synthesis reaction", *Journal of Catalysis*, vol. 179(2), pp. 548-559
- [12] X. Bao, M. Muhler, B. Pettinger, Y. Uchida, G. Lehmpfuhl, R. Schlögl, G. Ertl (1995), "The effect of water on the formation of strongly bound oxygen on silver surfaces", *Catalysis Letters*, vol. 32, no. 1.
- [13] I. E. Wachs, R. Madix (1978), "The oxidation of methanol on a silver (110) catalyst", *Surf Sci* 76(2):531-558.
- [14] A. Andreasen, H. Lynggaard, C. Stegelmann, P. Stoltze (2005), "Simplified kinetic models of methanol oxidation on silver", *Appl Catal A* 289(2):267-273.
- [15] H. Aljama, J. S. Yoo, J. K. Nørskov, F. Abdil-Pedersen, F. Studt (2016), "Methanol partial oxidation on Ag (111) from first principles.", *ChemCatChem* 8(23):3621-3625.

- [16] F. Hayer, H. Bakhary-Davijany, R. Myrstad, A. Holmen, P. Pfeifer, H. J. Venvik (2013), "Characteristics of integrated micro packed bed reactor-heat exchanger configurations in the direct synthesis of dimethyl ether", *Chemical Engineering and Processing* 70: 77-85.
- [17] H. Bakhary-Davijany, F. Dadgar, F. Hayer, X. K. Phan, R. Myrstad, H. J. Venvik, P. Pfeifer, A. Holmen (2012), "Analysis of External and Internal Mass Transfer at Low Reynolds Number in a Multiple-Slit Packed Bed Microstructured Reactor for Synthesis of Methanol from Syngas", *Industrial & Engineering Chemistry Research*.
- [18] A. Beretta, P. Baiardi, D. Prina, P. Forzatti (1999), "Analysis of a catalytic annular reactor for very short contact times", *Chemical Engineering Science* 54: 765-773.
- [19] J. W. Niemantsverdriet (2007), "Spectroscopy in Catalysis", Wiley, Third edition.
- [20] Bruker AXS GmbH, "TOPAS 5 Technical Reference", DIFFRAC.SUITE, 2014
- [21] R. E. Dinnebier, A. Leineweber, J. S.O. Evan (2018), "Rietveld Refinement: Practical Powder Diffraction Pattern Analysis using TOPAS", De Gruyter, DOI: <https://doi.org/10.1515/9783110461381>
- [22] D. L. Bish, S. A. Howard (1988), "Quantitative Phase Analysis Using the Rietveld Method", *J. Appl. Cryst.*, 21.
- [23] L. B. McCusker, R. B. Von Dreele, D. E. Cox, D. Louer, P. Scardi (1999), "Rietveld refinement guidelines", *J. Appl. Cryst.*, 32.
- [24] K. H. Wells (2020), "XRD and structure analysis with Topas; Background and introduction to XRD", unpublished material, Institute for Material Technology, the Norwegian University for Science and Technology.
- [25] K. H. Wells (2020), "XRD and structure analysis with Topas; Data fitting, methods and where to find information", unpublished material, Institute for Material Technology, the Norwegian University of Science and Technology.
- [26] R. A. Schwartz, D. P. Field, B. L. Adams, M. Kumar, A. J. Schwartz (2009) "Present State of Electron Backscatter Diffraction and Prospective Developments" In: Schwartz A., Kumar M., Adams B., Field D. (eds) *Electron Backscatter Diffraction in Materials Science*. Springer, Boston, MA
- [27] D. J. Dingley, D. P. Field (1997), "Electron backscatter diffraction and orientation imaging microscopy", *Materials Science and Technology*, 13:1, 69-78, DOI: 10.1179/mst.1997.13.1.69
- [28] J. H. Holgate, J. Webb (2003), "MICROSCOPY| Light Microscopy and Histochemical Methods", *Encyclopedia of Food Sciences and Nutrition*, second edition: 3917-3922.
- [29] T. Greibrokk, E. Lundanes, K. E. Rasmussen (1994), "Kromatografi: separasjon og deteksjon", 3rd ed., Oslo: Universitetsforlaget.
- [30] J. T. Richardson (1989), "Principles of catalyst development; Fundamental and applied catalysis". New York: Plenum Press.
- [31] J. Stewart, G. V. Voort (2020, 20 June). "Metallography of precious metals for Jewelry",

Available from: [https://www.buehler.com/assets/solutions/technotes/vol2\\_issue5.pdf](https://www.buehler.com/assets/solutions/technotes/vol2_issue5.pdf)

- [32] K. Arnesen (2018), "Oxidation of methanol to formaldehyde over Ag catalyst; A study of reaction pathways and Ag catalyst restructuring during MMTF", Master thesis, NTNU Department of Chemical Engineering.
- [33] N. Beck (2017), "Oxidation of methanol to formaldehyde over Ag catalysts", Master thesis, Karlsruhe Institute of Technology; Institute of Micro Process Engineering and the Norwegian University of Science and Technology; Department of Chemical Engineering.

# Appendices

## A. Reactor Details

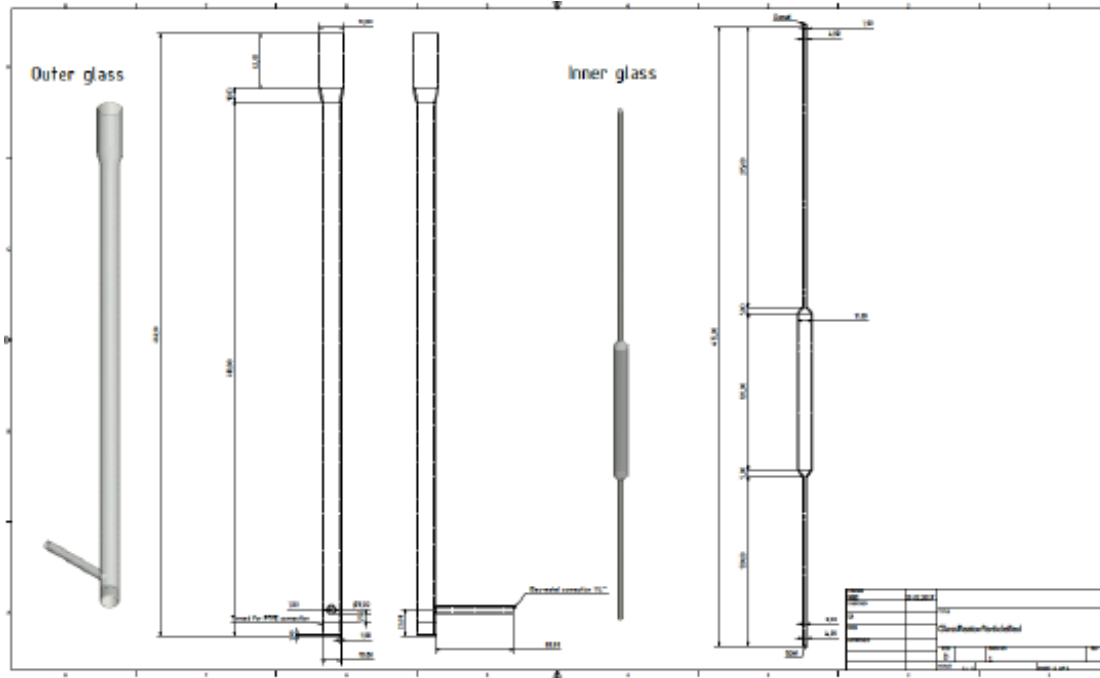


Figure A.1: Details for the reactor employed when performing methanol oxidation experiments in the MTF set-up.



## B. X-Ray Diffraction

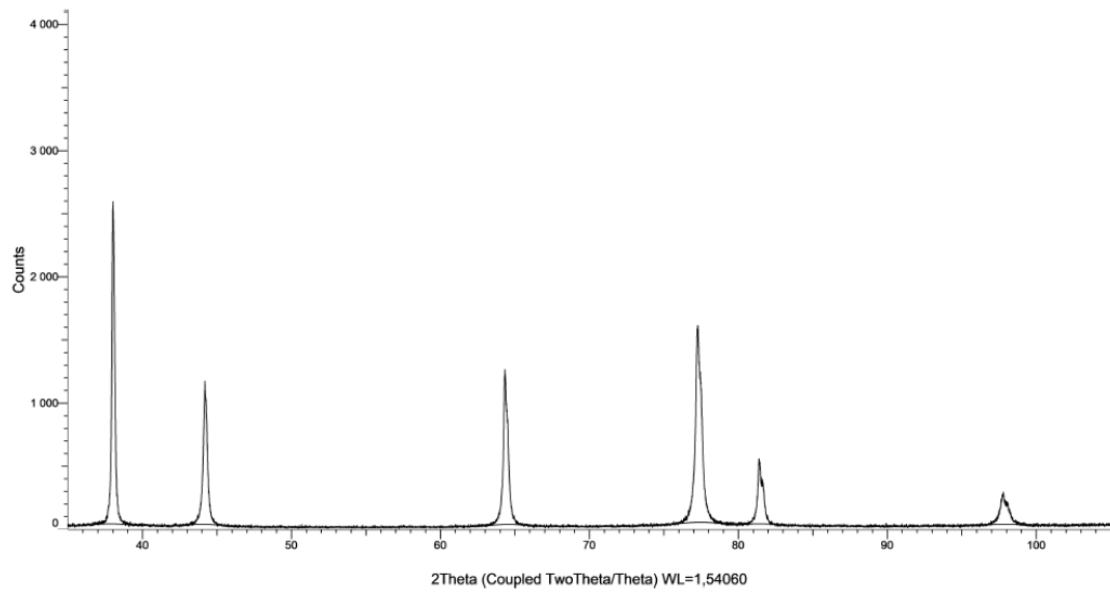


Figure B.1: X-ray diffractogram of unused particles from autumn 2019.

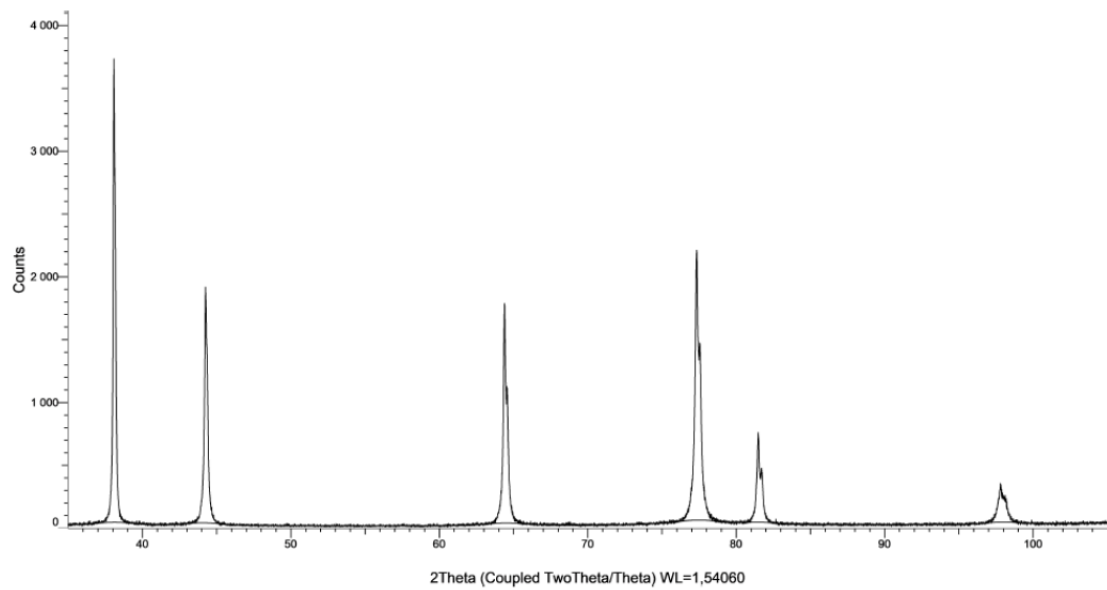


Figure B.2: X-ray diffractogram of particles calcined in air for 5 h, from autumn 2019.

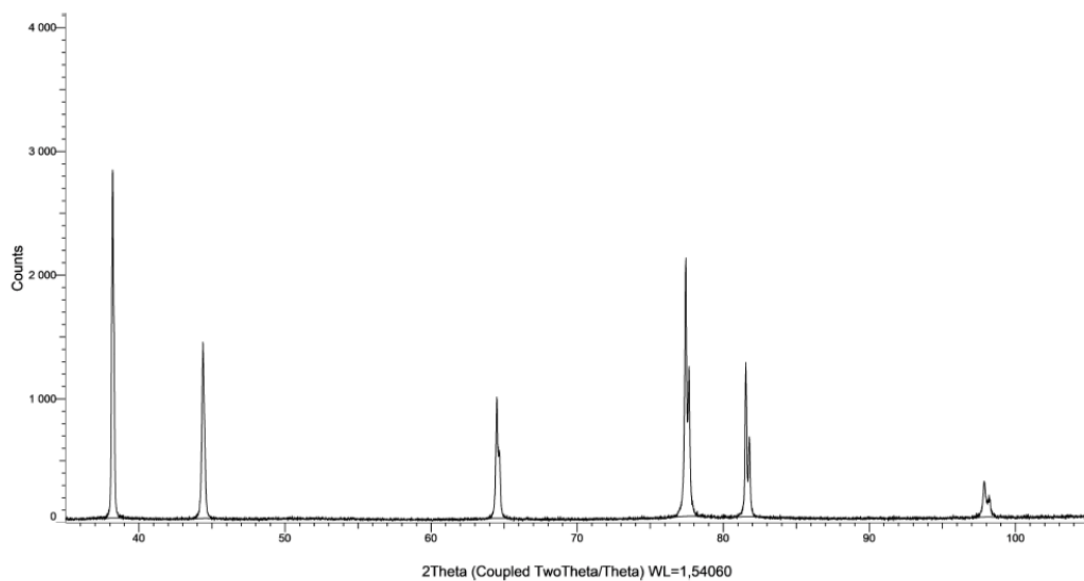


Figure B.3: X-ray diffractogram of particles calcined in air for 5 h by previous student, from autumn 2019.

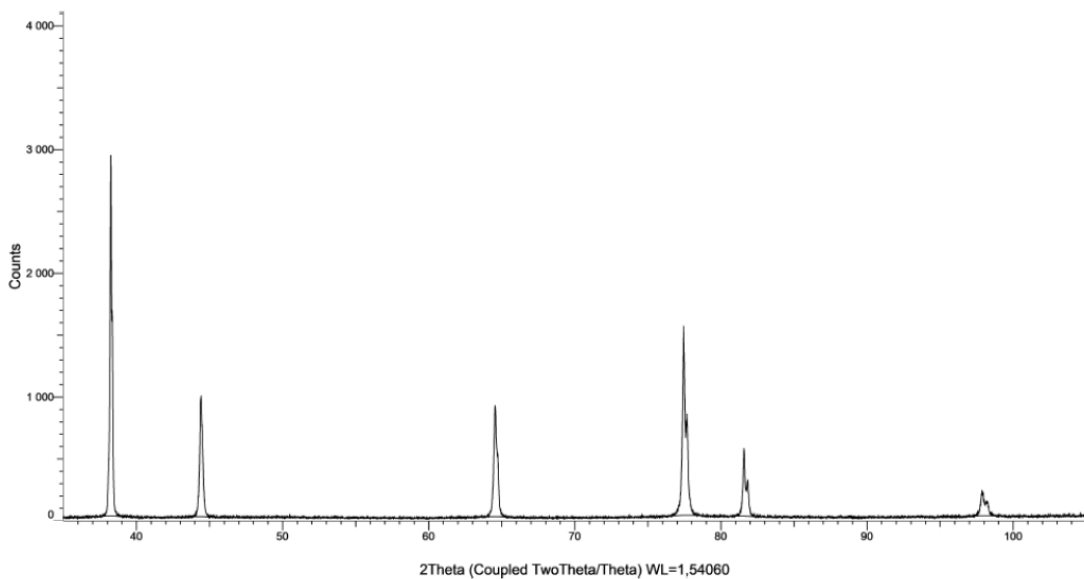


Figure B.4: X-ray diffractogram of particles calcined in air for 24 h by previous student, from autumn 2019.

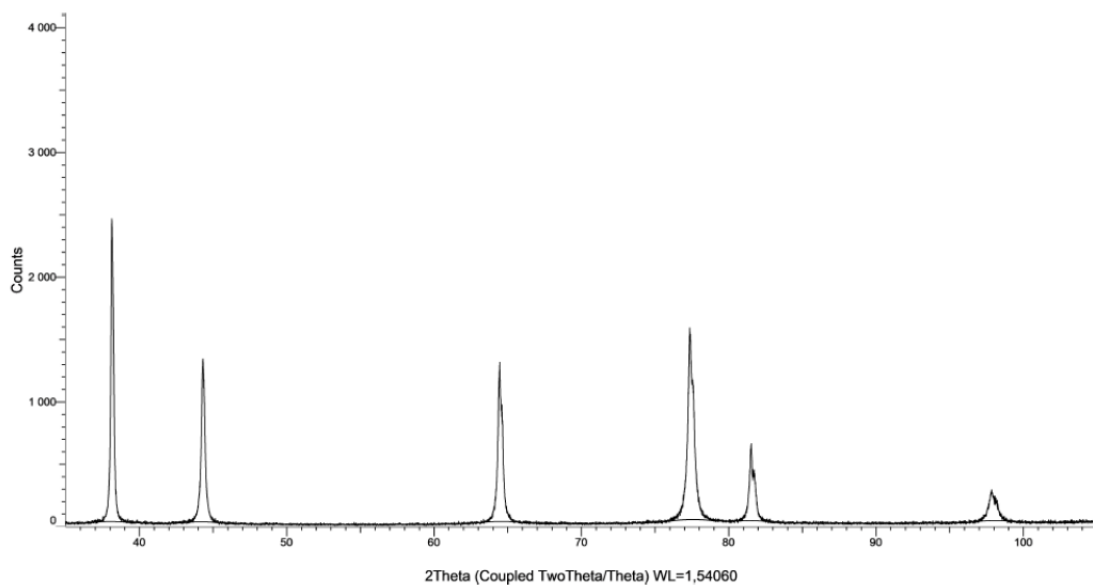


Figure B.5: X-ray diffractogram of particles calcined in air for 45 h, from autumn 2019.

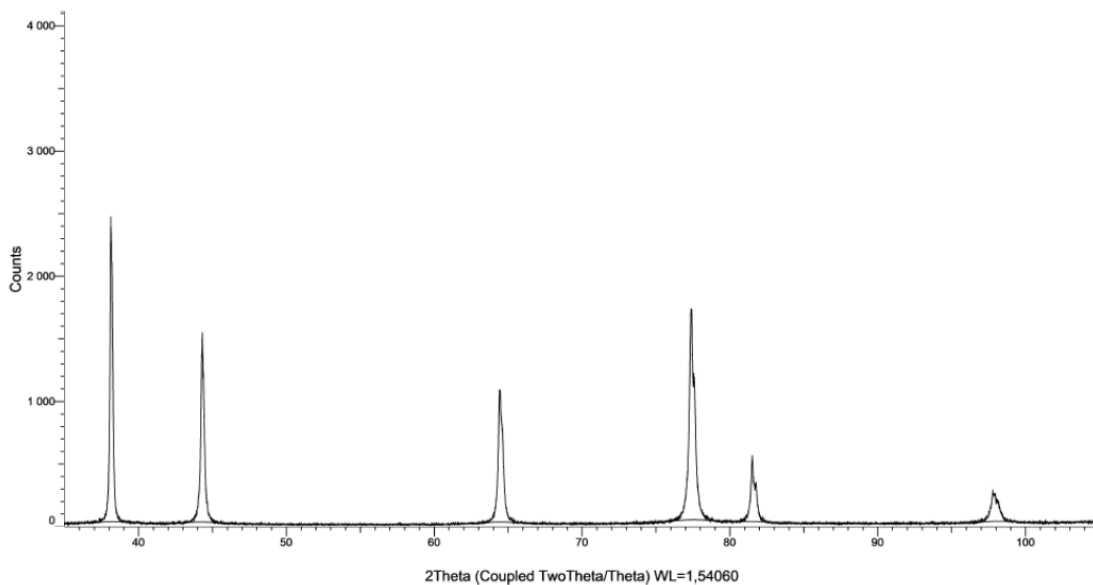


Figure B.6: X-ray diffractogram of particles calcined in hydrogen (2 %) and argon for 19 h, from autumn 2019.

## C. Scanning Electron Microscopy

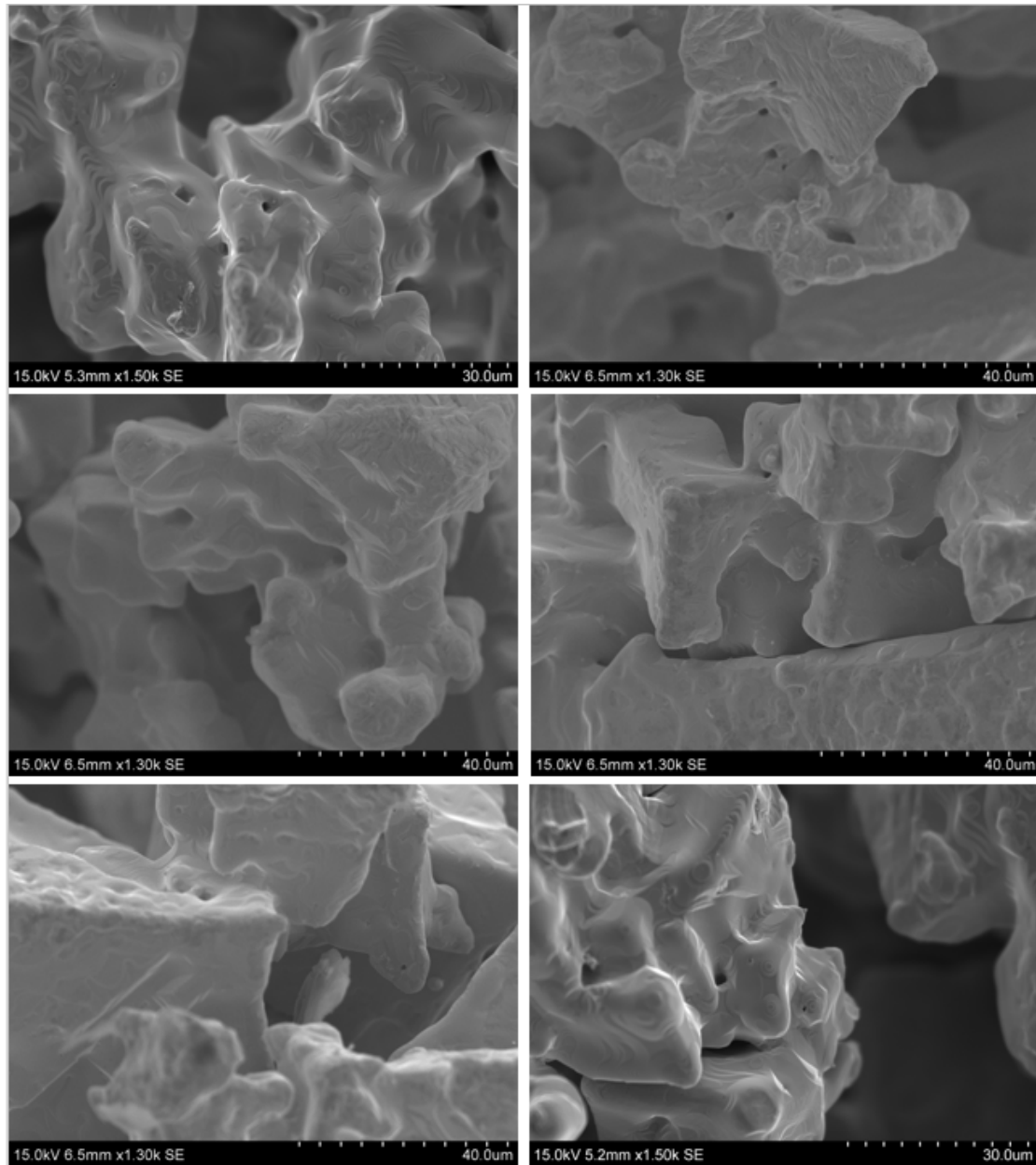


Figure C.1: SEM images of particles after 5 h calcination in air at 650 °C.

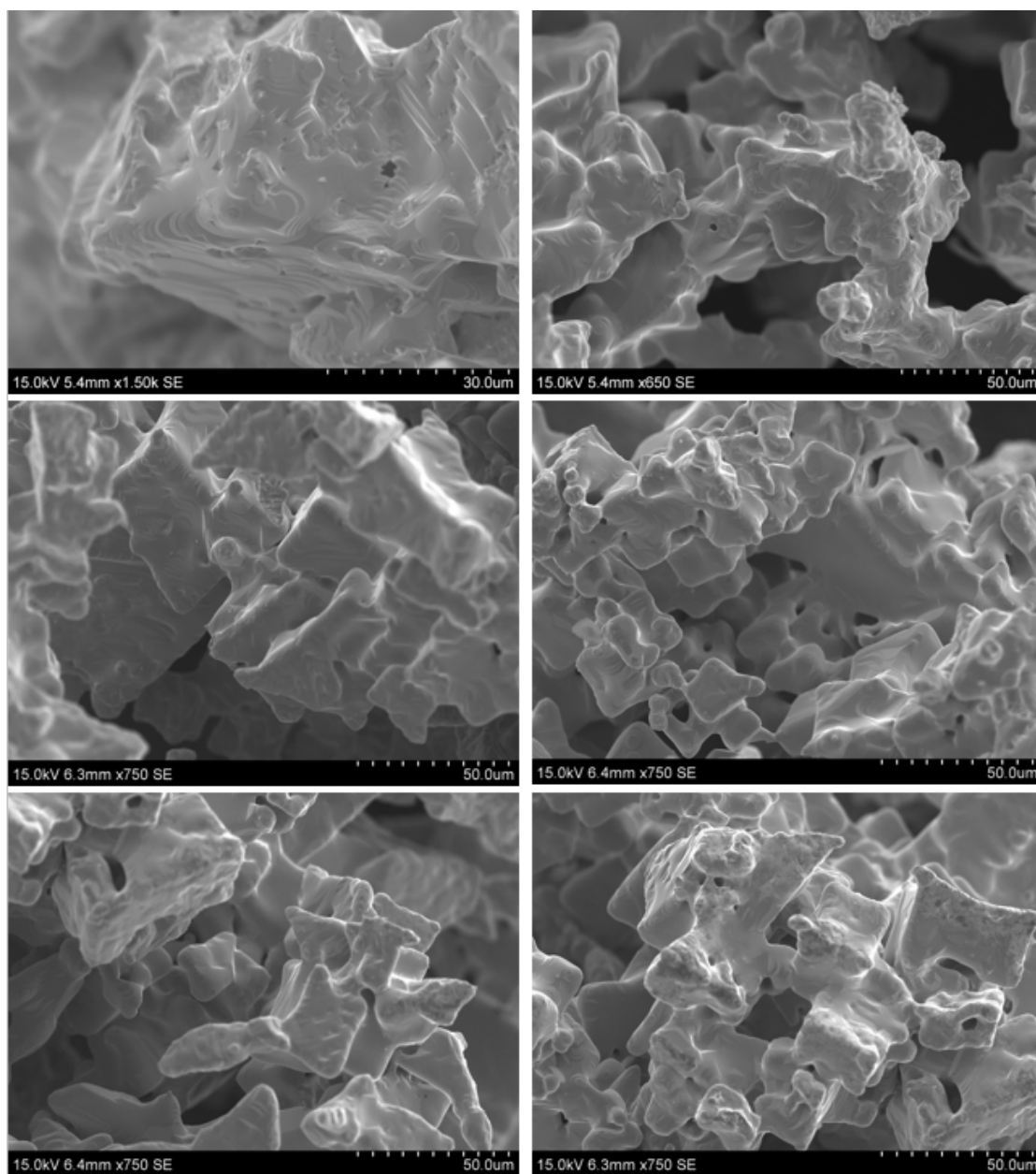


Figure C.2: SEM images of particles after 24 h calcination in air at 650 °C.

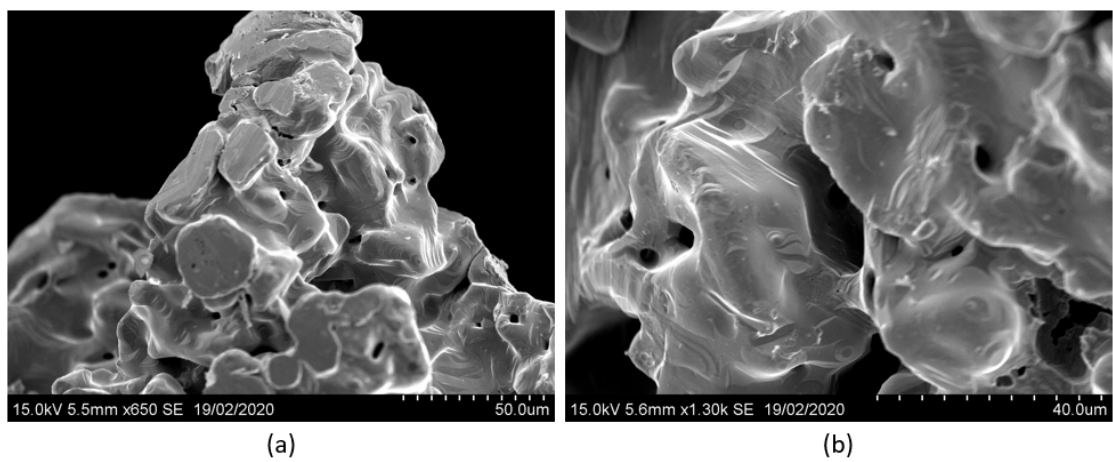


Figure C.3: SEM images of particles after 24 h calcination in air at 650 °C.

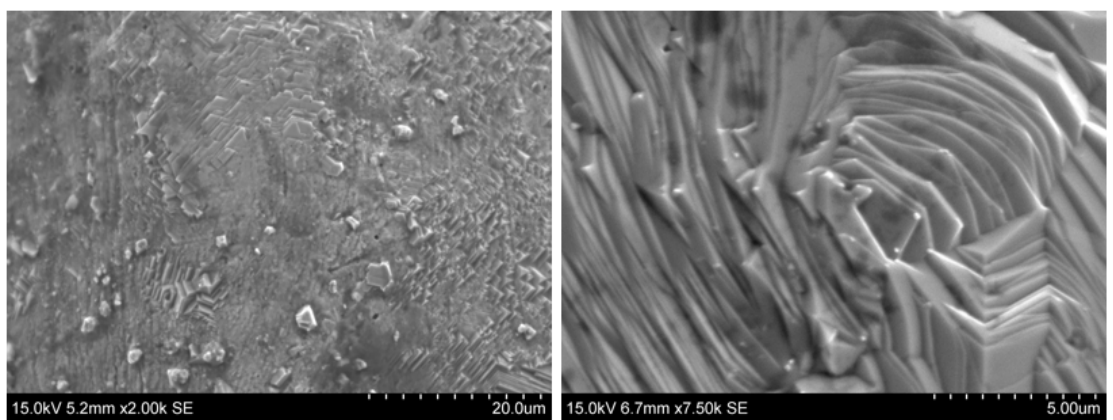


Figure C.4: SEM images of net after 45 h calcination in air at 650 °C.

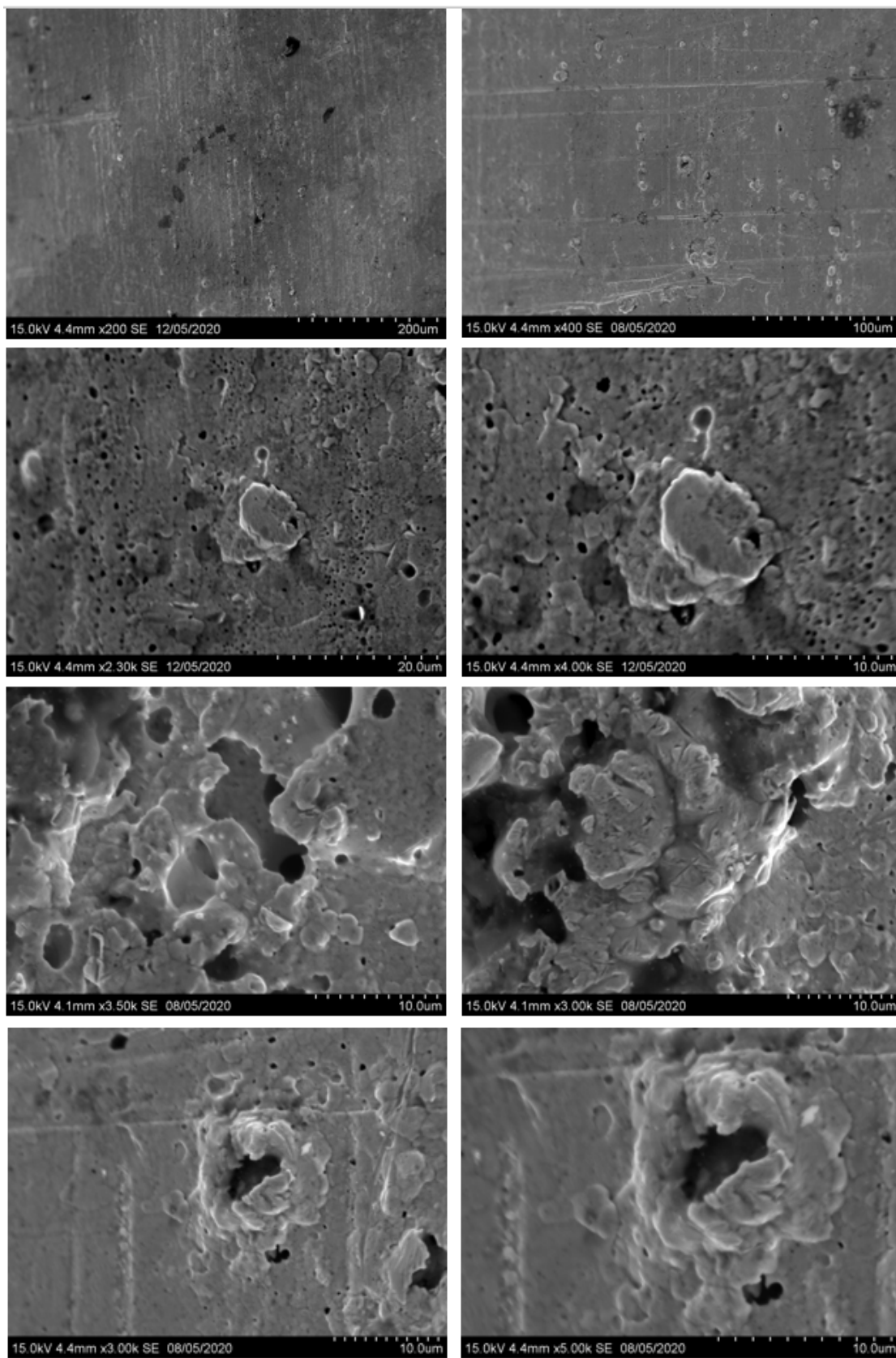


Figure C.5: SEM images of annular used in methanol oxidation in nitrogen at 600 °C, TOS of 4 days. VIII

## D. Activity Calculations

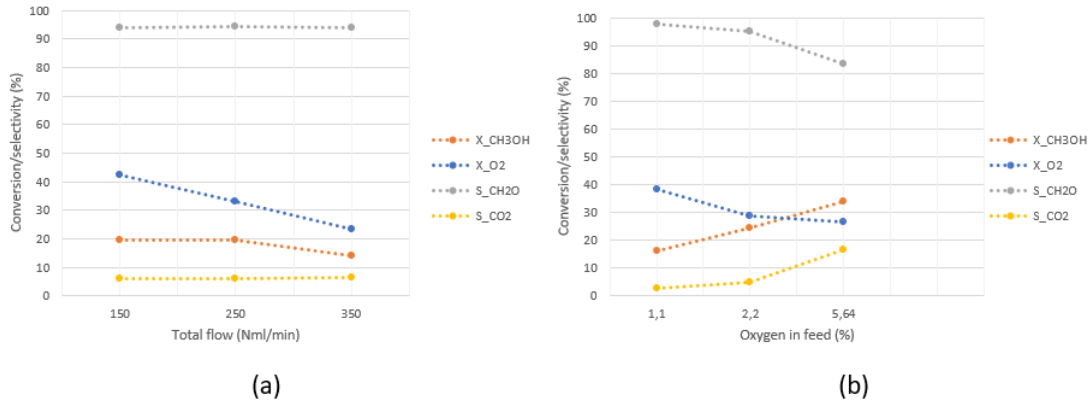


Figure D.1: Catalytic activity for the first helium experiment, with changes in linear gas velocity (a) and oxygen concentration in feed (b).

Table D.1: Feed analysis for the first methanol oxidation experiment performed in helium.

	250 ml/min (standard)	150 ml/min	350 ml/min	250 ml/min, double oxy- gen concen- tration	250 ml/min, halved oxy- gen concen- tration
Helium	65.58	65.18	65.90	58.41	78.18
Oxygen	3.318	3.521	3.402	5.639	1.095
Nitrogen	11.52	12.33	11.84	20.73	5.124
Air/H <sub>2</sub> /CO	15.02	15.94	15.35	26.99	6.457
Water	12.09	11.89	11.87	9.816	9.278
Methanol	7.634	7.772	7.577	6.469	5.976



Table D.2: Feed analysis for the second methanol oxidation experiment performed in helium.

	250 ml/min (standard)	150 ml/min	350 ml/min	250 ml/min, double oxy- gen concen- tration	250 ml/min, halved oxygen iconcentra- tion
Helium	65.68	63.23	65.76	53.15	72.81
Oxygen	3.402	3.795	3.438	5.860	1.309
Nitrogen	11.88	13.46	12.01	22.08	5.898
Air/H <sub>2</sub> /CO	15.34	17.32	15.49	28.83	7.458
Water	11.61	11.74	11.51	11.66	11.21
Methanol	7.491	7.637	7.321	7.434	7.411

Table D.3: Feed analysis for the methanol oxidation experiment performed in nitrogen.

	250 ml/min (standard)	150 ml/min	350 ml/min	250 ml/min, double oxy- gen concen- tration	250 ml/min, halved oxy- gen concen- tration
Oxygen	3.018	2.994	3.020	6.009	1.469
Nitrogen	78.64	77.48	78.52	75.26	79.42
Air/H <sub>2</sub> /CO	86.01	84.81	85.91	85.48	85.33
Water	11.67	12.18	11.80	11.66	11.76
Methanol	7.648	7.949	7.431	7.600	7.627

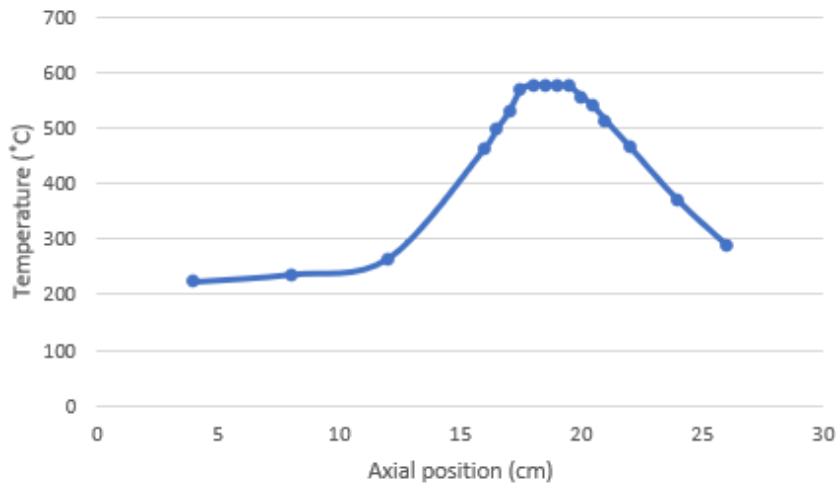


Figure D.2: Temperature profile through the reactor, measured during experiment.

Calculation example for methanol conversion and formaldehyde selectivity for the first methanol oxidation experiment in helium:

$$X_{CH_3OH} = 1 - \frac{6.255 \times 65.58}{7.634 \times 65.36} \times 100\% = 17.80\% \quad (D.1)$$

$$S_{CH_2O} = \frac{0.852}{0.852 + 0.041} = 95.41\% \quad (D.2)$$

The following calculation example is for calculation of formaldehyde selectivity with Equation 2.20, and shows the effect of high carbon error.

$$S_{CH_2O} = \frac{249.2 \times 0.852}{250 \times 7.634 - 249.2 \times 6.244} = 60.23\% \quad (D.3)$$

## E. Risk Assessment



<b>ID</b>	34535	<b>Status</b>	<b>Dato</b>
<b>Risikoområde</b>	Risikovurdering: Helse, miljø og sikkerhet (HMS)	Opprettet	05.09.2019
<b>Opprettet av</b>	Susanne Klungland Stokkevåg	Vurdering startet	09.09.2019
<b>Ansvarlig</b>	Hilde Johnsen Venvik	Tiltak besluttet	
		Avsluttet	

**Risikovurdering:****Cat\_Master Student\_2020\_Susanne Stokkevåg****Gyldig i perioden:**

9/5/2019 - 9/5/2022

**Sted:**

Trondheim

**Mål / hensikt**

Formaldehyde is an important industrial chemical. In this thesis formaldehyde production from methanol will be performed, using a silver catalyst. The synthesis will be performed on both silver particles and silver net with a goal of testing the catalytic activity of silver in industrial conditions. X-ray diffraction (XRD), scanning electron microscopy (SEM) and electron backscatter diffraction (EBSD) will be used to characterize the catalysts. In addition, experiments testing the mass transfer limitations in the methanol oxidation will be performed. Two reactions will be performed, and diluted in two different inert gases; helium or nitrogen, to observe if mass transfer limits the reaction.

**Bakgrunn**

By studying the interactions between the catalyst and various gases at industrial conditions, the most optimal configuration for a selective MTF synthesis and a better understanding of the reaction mechanism can be achieved. The project is given by the catalysis group at the department of chemical engineering at NTNU, and is in cooperation with Dynea and K. A. Rasmussen.

**Beskrivelse og avgrensninger**

The experiments will be performed in the methanol to formaldehyde setup (rig 1.3 in Kjemihall D). In the experiments, silver particles with size fraction from 0.25-0.50 mm will be used. Hydrogen, nitrogen, synthetic air, carbon monoxide, helium, nitrogen and methanol gases will be employed, and the temperature will range between 200-700 degrees celcius. Experiment durations will be from 5-96 hours. The main risks connected to the experiments are the explosive and toxic gases at high temperatures. As the setup contains safety valves and controllers as well as proper ventilation, the risks are acceptable. Proper routines will also be applied, as leak testing, use of hydrogen and carbon monoxide detectors and sufficient protective gear. The amount of carbon monoxide that is used/produced is also very small and diluted.

March-April 2020 - In the event of lab closure as preventive measure to spread of covid19 infection:

- 1) Switch off procedure for SET-UP 1.3 Chem Hall
  - Turn GC and GC computer (PC to the right) OFF.
  - Close valves on gas cylinders surrounding setup (except N2) and MeOH container (inside setup, turn valve to center position).
  - If possible, keep a small flow of N2 (20 ml/min, controlled by LabNet) and evaporator CEM ON.
  - All lines should stay heated to avoid any polymerization or condensation of products still left in pipelines.
- 2) Risk related to shortage of personnel in the labs:
  - All the lab activities can continue regularly but taking extra-safety measures (work alone alarm, avoid handling of toxic/flammable gases outside of working hours)
- 3) Safety measures related to spread of covid19 infection:
  - Avoid touching the face
  - Keep 2 m distance from colleagues
  - Use nitrile gloves when touching shared lab set-ups and equipment
  - Disinfection before and after, with ethanol, on all common equipment (door knob - card reader with code panel - balance in chem hall - lab area - XRD sample holder - keyboard, mouse)
  - Wash hands as often as possible

**Forutsetninger, antakelser og forenklinger**

[Ingen registreringer]



### Vedlegg

AppCard\_20.doc  
Ddatasheet CH2O.pdf  
Ddatasheet CO2.pdf  
Ddatasheet N2.pdf  
Ddatasheet CH3OH.pdf  
Ddatasheet O2.pdf  
Ddatasheet H2.pdf  
Ddatasheet Ag.pdf  
PolyFast.pdf  
Epofix resin.pdf  
Epofix hardener.pdf  
Ddatasheet He.pdf

### Referanser

[Ingen registreringer]

## Oppsummering, resultat og endelig vurdering

I oppsummeringen presenteres en oversikt over farer og uønskede hendelser, samt resultat for det enkelte konsekvensområdet.

**Farekilde:** XRD

**Uønsket hendelse:** X-ray radiation

**Konsekvensområde:** Helse

Risiko før tiltak: Risiko etter tiltak:

**Farekilde:** Chemicals

**Uønsket hendelse:** Silver spillage

**Konsekvensområde:** Helse

Risiko før tiltak: Risiko etter tiltak:

**Uønsket hendelse:** Methanol spillage

**Konsekvensområde:** Helse

Risiko før tiltak: Risiko etter tiltak:

**Uønsket hendelse:** Formaldehyde spillage

**Konsekvensområde:** Helse

Risiko før tiltak: Risiko etter tiltak:

**Uønsket hendelse:** Nitrogen leakage

**Konsekvensområde:** Helse

Risiko før tiltak: Risiko etter tiltak:

**Uønsket hendelse:** Hydrogen leakage

**Konsekvensområde:** Helse

Risiko før tiltak: Risiko etter tiltak:

**Uønsket hendelse:** Oxygen leakage

**Konsekvensområde:** Helse

Risiko før tiltak: Risiko etter tiltak:

**Uønsket hendelse:** Leakage from other experiments

**Konsekvensområde:** Helse

Risiko før tiltak: Risiko etter tiltak:



**Farekilde:** Chemicals

---

**Uønsket hendelse:** Carbon monoxide leakage

**Konsekvensområde:** Helse

Risiko før tiltak: Risiko etter tiltak:

**Uønsket hendelse:** Carbon dioxide leakage

**Konsekvensområde:** Helse

Risiko før tiltak: Risiko etter tiltak:

**Uønsket hendelse:** Helium leakage

**Konsekvensområde:** Helse

Risiko før tiltak: Risiko etter tiltak:

**Farekilde:** SEM

---

**Uønsket hendelse:** x-ray radiation

**Konsekvensområde:** Helse

Risiko før tiltak: Risiko etter tiltak:

**Farekilde:** Calcination

---

**Uønsket hendelse:** High temperature

**Konsekvensområde:** Helse

Risiko før tiltak: Risiko etter tiltak:

**Farekilde:** Compressed gases

---

**Uønsket hendelse:** Explosion

**Konsekvensområde:** Helse

Risiko før tiltak: Risiko etter tiltak:

**Farekilde:** Temperature

---

**Uønsket hendelse:** Fire

**Konsekvensområde:** Helse

Risiko før tiltak: Risiko etter tiltak:





**Farekilde:** Temperature

---

**Uønsket hendelse:** Explosion

**Konsekvensområde:** Helse

Risiko før tiltak:  Risiko etter tiltak: 

**Farekilde:** EBSD

---

**Uønsket hendelse:** X-ray radiation

**Konsekvensområde:** Helse

Risiko før tiltak:  Risiko etter tiltak: 

**Uønsket hendelse:** Molding

**Konsekvensområde:** Helse

Risiko før tiltak:  Risiko etter tiltak: 

**Uønsket hendelse:** Grinding and polishing

**Konsekvensområde:** Helse

Risiko før tiltak:  Risiko etter tiltak: 

**Uønsket hendelse:** Cutting epoxy

**Konsekvensområde:** Helse

Risiko før tiltak:  Risiko etter tiltak: 

**Uønsket hendelse:** Light microscope

**Konsekvensområde:** Helse

Risiko før tiltak:  Risiko etter tiltak: 

**Farekilde:** Working in the lab under Covid-situation

---

**Uønsket hendelse:** Spreading of virus

**Konsekvensområde:** Helse

Risiko før tiltak:  Risiko etter tiltak: 

### Endelig vurdering



## Involverte enheter og personer

En risikovurdering kan gjelde for en, eller flere enheter i organisasjonen. Denne oversikten presenterer involverte enheter og personell for gjeldende risikovurdering.

### Enhet /-er risikovurderingen omfatter

- Institutt for kjemisk prosessteknologi

### Deltakere

#### Lesere

Stine Lervold

Estelle Marie M. Vanhaecke

Anne Hoff

Karin Wiggen Dragsten

### Andre involverte/interessenter

[Ingen registreringer]

## Følgende akseptkriterier er besluttet for risikoområdet Risikovurdering: Helse, miljø og sikkerhet (HMS):

#### Helse



#### Materielle verdier



#### Omdømme



#### Ytre miljø



## Oversikt over eksisterende, relevante tiltak som er hensyntatt i risikovurderingen

I tabellen under presenteres eksisterende tiltak som er hensyntatt ved vurdering av sannsynlighet og konsekvens for aktuelle uønskede hendelser.

Farekilde	Uønsket hendelse	Tiltak hensyntatt ved vurdering
XRD	X-ray radiation	Instrument training
	X-ray radiation	Apparatus cards
Chemicals	Silver spillage	Suitable clothing
	Methanol spillage	Suitable clothing
	Methanol spillage	Safety in the setup
	Formaldehyde spillage	Suitable clothing
	Formaldehyde spillage	Safety in the setup
	Nitrogen leakage	Suitable clothing
	Nitrogen leakage	Instrument training
	Nitrogen leakage	Apparatus cards
	Nitrogen leakage	Safety in the setup
	Hydrogen leakage	Suitable clothing
	Hydrogen leakage	Instrument training
	Hydrogen leakage	Apparatus cards
	Hydrogen leakage	Alarm systems
	Hydrogen leakage	Safety in the setup
	Oxygen leakage	Suitable clothing
	Oxygen leakage	Instrument training
	Oxygen leakage	Apparatus cards
	Oxygen leakage	Alarm systems
Oxygen leakage	Safety in the setup	
Leakage from other experiments	Suitable clothing	
Leakage from other experiments	Instrument training	
Leakage from other experiments	Apparatus cards	
Leakage from other experiments	Alarm systems	
Carbon monoxide leakage	Suitable clothing	
Carbon monoxide leakage	Instrument training	
Carbon monoxide leakage	Apparatus cards	
Carbon monoxide leakage	Alarm systems	
Carbon monoxide leakage	Safety in the setup	
Carbon dioxide leakage	Suitable clothing	
Carbon dioxide leakage	Instrument training	
Carbon dioxide leakage	Apparatus cards	



Chemicals	Carbon dioxide leakage	Alarm systems
	Carbon dioxide leakage	Safety in the setup
	Helium leakage	Suitable clothing
	Helium leakage	Instrument training
	Helium leakage	Safety in the setup
SEM	x-ray radiation	Instrument training
	x-ray radiation	Apparatus cards
Calcination	High temperature	Suitable clothing
	High temperature	Instrument training
	High temperature	Apparatus cards
	High temperature	Alarm systems
Compressed gases	Explosion	Suitable clothing
	Explosion	Instrument training
	Explosion	Apparatus cards
	Explosion	Alarm systems
	Explosion	Safety in the setup
Temperature	Fire	Instrument training
	Fire	Apparatus cards
	Fire	Alarm systems
	Explosion	Instrument training
	Explosion	Apparatus cards
	Explosion	Alarm systems
EBSD	X-ray radiation	Instrument training
	X-ray radiation	Apparatus cards
	Molding	Suitable clothing
	Molding	Instrument training
	Molding	Safety in the setup
	Grinding and polishing	Suitable clothing
	Grinding and polishing	Instrument training
	Grinding and polishing	Apparatus cards
	Cutting epoxy	Instrument training
	Cutting epoxy	Apparatus cards
	Light microscope	Instrument training
Working in the lab under Covid-situation	Spreading of virus	

**Eksisterende og relevante tiltak med beskrivelse:****Suitable clothing**

To reduce contact between skin, eyes and the chemicals at the lab, suitable clothing are used. This involves lab coat, gloves and glasses.

**Instrument training**

Training sessions are mandatory before using instruments like SEM and XRD. This leads to knowlegde about both the instruments and the risks associated with them, and can thereby decrease potential accidents.

**Apparatus cards**

Apparatus cards are placed next to instruments to make sure that the users has the apporoaches close by.

**Alarm systems**

The labs are equipped with fire alarms and an alarm system that goes off when the CO concentration in the room gets too high. This will inform everyone in the relevant area, so that they can evacuate before the conditions gets critical.

**Safety in the setup**

The methanol to formaldehyde setup contains safety valves and controllers, in addition to a proper ventilation system. This reduces the risks connected to the employed gases.

## Risikoanalyse med vurdering av sannsynlighet og konsekvens

I denne delen av rapporten presenteres detaljer dokumentasjon av de farer, uønskede hendelser og årsaker som er vurdert. Innledningsvis oppsummeres farer med tilhørende uønskede hendelser som er tatt med i vurderingen.

**Følgende farer og uønskede hendelser er vurdert i denne risikovurderingen:**

- **XRD**
  - X-ray radiation
- **Chemicals**
  - Silver spillage
  - Methanol spillage
  - Formaldehyde spillage
  - Nitrogen leakage
  - Hydrogen leakage
  - Oxygen leakage
  - Leakage from other experiments
  - Carbon monoxide leakage
  - Carbon dioxide leakage
  - Helium leakage
- **SEM**
  - x-ray radiation
- **Calcination**
  - High temperature
- **Compressed gases**
  - Explosion
- **Temperature**
  - Fire
  - Explosion
- **EBSD**
  - X-ray radiation
  - Molding
  - Grinding and polishing
  - Cutting epoxy
  - Light microscope
- **Working in the lab under Covid-situation**
  - Spreading of virus

**Detaljert oversikt over farekilder og uønskede hendelser:****Farekilde: XRD**

XRD (x-ray diffraction) will be used to examine silver's surface and structure. The instrument uses X-ray sources, which are known to cause mutation of DNA and cancer. XRD will be controlled by trained staff, and the only risk affecting me is thereby my sample.

**Uønsket hendelse: X-ray radiation**

Exposure to x-rays can lead to mutation of DNA and cancer.

*Årsak:* Lead windows break

*Beskrivelse:*

The x-ray sources are shielded with lead glass windows and lead walls. Radiation is only possible if the windows break.

*Sannsynlighet for hendelsen (felles for alle konsekvensområder):* **Svært lite sannsynlig (1)**

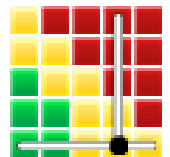
*Kommentar:*

The radiation is only possible if the instrument's lead glass windows breaks.

**Konsekvensområde: Helse**

*Vurdert konsekvens:* **Svært stor (4)**

*Kommentar:* X-rays can cause mutations of DNA and cancer, so the consequences of radiation can be large.

**Risiko:**

**Farekilde: Chemicals**

There are different risks connected to the chemicals used in this project.

**Uønsket hendelse: Silver spillage**

Silver can be spilled when being handled in the lab. For instance when preparing it for XRD or SEM.

*Årsak:* Inaccurate handling

*Sannsynlighet for hendelsen (felles for alle konsekvensområder):* **Sannsynlig (3)**

*Kommentar:*

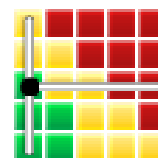
The silver particles are small, which makes it likely that some spillage might occur when handling them.

**Konsekvensområde: Helse**

*Vurdert konsekvens:* **Liten (1)**

*Kommentar:* The silver is pure (99,999 %), which means that it is not any health related consequences when it is spilled.

**Risiko:**

**Uønsket hendelse: Methanol spillage**

Methanol can be spilled at the lab when it is handled inaccurately.

*Årsak:* Inaccurate handling

*Sannsynlighet for hendelsen (felles for alle konsekvensområder):* **Lite sannsynlig (2)**

*Kommentar:*

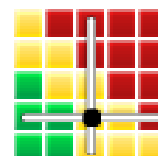
The risks connected to this chemical is known and it will be handled carefully. The probability of spillage is however still present.

**Konsekvensområde: Helse**

*Vurdert konsekvens:* **Stor (3)**

*Kommentar:* Methanol is combustible and toxic if in contact with skin, if inhaled, and if swallowed. It also causes organ damages. The consequence of spillage can thereby be large when regards to health. The chemical should be kept away from heat and appropriate protective gear should be used during experiments.

**Risiko:**



**Uønsket hendelse: Formaldehyde spillage**

---

Formaldehyde is produced in the setup and can be spilled if not handled carefully. The chemical

*Årsak:* Inaccurate handling

*Sannsynlighet for hendelsen (felles for alle konsekvensområder):*

**Lite sannsynlig (2)**

*Kommentar:*

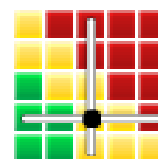
The risks connected to this chemical is known and it will be handled carefully. The probability of spillage is however still present.

**Konsekvensområde: Helse**

*Vurdert konsekvens:* **Stor (3)**

*Kommentar:* Formaldehyde is toxic when swallowed, when in contact with skin and when inhaled. It also, among others, causes corrosive damages to eyes and skin and can cause cancer. The consequences of spillage can thereby be large in regards to health

**Risiko:**

**Uønsket hendelse: Nitrogen leakage**

---

Compressed nitrogen gas will be used in parts of the experiment. Gas under pressure can explode if heated, and needs to be handled with care.

*Årsak:* Inaccurate handling

*Sannsynlighet for hendelsen (felles for alle konsekvensområder):*

**Lite sannsynlig (2)**

*Kommentar:*

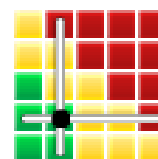
The risks connected to this chemical is known and it will be handled carefully, instruments will also be checked for leakage before use. The probability of leakage is however still present.

**Konsekvensområde: Helse**

*Vurdert konsekvens:* **Middels (2)**

*Kommentar:* The nitrogen gas is compressed and can explode when heated, it is also stifling at high concentrations. It should be stored in a ventilated place. The consequences of nitrogen leakage are thereby medium in regards to health.

**Risiko:**





**Uønsket hendelse: Hydrogen leakage**

---

Compressed hydrogen gas will be used in parts of the experiment. Gas under pressure can explode if heated, and needs to be handled with care.

*Årsak:* Inaccurate handling

*Sannsynlighet for hendelsen (felles for alle konsekvensområder):* **Lite sannsynlig (2)**

*Kommentar:*

The risks connected to this chemical is known and it will be handled carefully, instruments will also be checked for leakage before use. The probability of leakage is however still present.

**Konsekvensområde: Helse**

*Vurdert konsekvens:* **Stor (3)**

*Kommentar:* The hydrogen gas is compressed and can explode if heated. Additionally it is also extremely flammable. The consequences related to leakage are therefore large in regards to health.

**Risiko:**

**Uønsket hendelse: Oxygen leakage**

---

Compressed nitrogen gas will be used in parts of the experiment. Gas under pressure can explode if heated, and needs to be handled with care.

*Årsak:* Inaccurate handling

*Sannsynlighet for hendelsen (felles for alle konsekvensområder):* **Lite sannsynlig (2)**

*Kommentar:*

The risks connected to this chemical is known and it will be handled carefully, instruments will also be checked for leakage before use. The probability of leakage is however still present.

**Konsekvensområde: Helse**

*Vurdert konsekvens:* **Stor (3)**

*Kommentar:* The oxygen gas is compressed and can explode when heated. It can additionally cause or reinforce fire. The consequences related to leakage are therefore large in regards to health.

**Risiko:**



**Uønsket hendelse: Leakage from other experiments**

---

There are a lot of experiments being performed simultaneously in the lab. It is therefore important to take into account that they can also leak various chemicals that might be dangerous, like CO.

Sannsynlighet for hendelsen (felles for alle konsekvensområder):

**Lite sannsynlig (2)**

*Kommentar:*

Everyone in the lab has had training and courses related to their experiments and HSE. It is therefore trusted that everyone handle their experiments and chemicals with care. The probability of leakage is however still present.

**Konsekvensområde: Helse**

Vurdert konsekvens: **Stor (3)**

*Kommentar:* It is hard to keep track of every experiment in the lab. Some can for instance work with carbon monoxide and/or hydrogen which can lead to large consequences if leaked.

**Risiko:**

**Uønsket hendelse: Carbon monoxide leakage**

---

Compressed carbon monoxide gas will be used in parts of the experiment. Gas under pressure can explode if heated, and needs to be handled with care.

*Årsak:* Inaccurate handling

Sannsynlighet for hendelsen (felles for alle konsekvensområder):

**Lite sannsynlig (2)**

*Kommentar:*

The risks connected to this chemical is known and it will be handled carefully, instruments will also be checked for leakage before use. The probability of leakage is however still present.

**Konsekvensområde: Helse**

Vurdert konsekvens: **Stor (3)**

*Kommentar:* Carbon monoxide is an extremely flammable gas that is toxic if inhaled. It can also, among others, damage an unborn child and cause damage to organs. The consequences related to leakage can therefore be large in regards to health.

**Risiko:**



**Uønsket hendelse: Carbon dioxide leakage**

---

Carbon dioxide is one of the products in the methanol to formaldehyde synthesis. The gas is toxic at high concentrations

*Årsak:* Inaccurate handling

*Sannsynlighet for hendelsen (felles for alle konsekvensområder):* **Lite sannsynlig (2)**

*Kommentar:*

The risks connected to this chemical is known and it will be handled carefully, instruments will also be checked for leakage before use. The probability of leakage is however still present.

**Konsekvensområde: Helse**

*Vurdert konsekvens:* **Middels (2)**

*Kommentar:* Carbon dioxide at high concentrations is stifling and can explode if heated. This is a product from the methanol to formaldehyde synthesis, and it is unlikely that the concentration will get so high that these risks are relevant. The consequences of carbon dioxide leakage are therefore medium in regards to health.

**Risiko:**

**Uønsket hendelse: Helium leakage**

---

Helium will be used to dilute the methanol oxidation. This gas is compressed and can explode if heated. It must therefore be handled with care.

*Sannsynlighet for hendelsen (felles for alle konsekvensområder):* **Lite sannsynlig (2)**

*Kommentar:*

The risks connected to this chemical is known and it will be handled carefully, instruments will also be checked for leakage before use. The probability of leakage is however still present.

**Konsekvensområde: Helse**

*Vurdert konsekvens:* **Stor (3)**

*Kommentar:* The helium gas is compressed and can explode if heated. The consequences related to leakage are therefore large in regards to health.

**Risiko:**



**Farekilde: SEM**

SEM will be used to examine the surface of silver.

**Uønsket hendelse: x-ray radiation**

Exposure to x-rays can lead to mutation of DNA and cancer.

Sannsynlighet for hendelsen (felles for alle konsekvensområder): **Svært lite sannsynlig (1)**

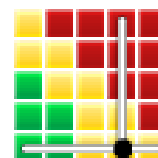
*Kommentar:*

The instrument is very safe, and exposure to X-ray radiation is highly unlikely.

**Konsekvensområde: Helse**

Vurdert konsekvens: **Svært stor (4)**

*Kommentar:* X-rays can cause mutations of DNA and cancer, so the consequences of radiation can be large.

**Risiko:**

**Farekilde: Calcination**

---

**Uønsket hendelse: High temperature**

---

In the calcination process temperatures from 500- 1150 degrees celcius is reached. This high temperatures can lead to burns and fire.

Sannsynlighet for hendelsen (felles for alle konsekvensområder): **Lite sannsynlig (2)**

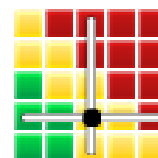
*Kommentar:*

The probability of burns and fire are small because of the instrument training, apparatus cards and alarm systems.

**Konsekvensområde: Helse**

Vurdert konsekvens: **Stor (3)**

*Kommentar:* Since the temperatures are high, physical contact can lead to third of fourth degree burns. There is also a risk of fire and mechanical hazard.

**Risiko:**

**Farekilde: Compressed gases**

---

During the project some compressed gases will be used. A risk using these is that they can explode is heated.

**Uønsket hendelse: Explosion**

---

Pressurised gases can explode if they are heated. Must therefore be handled with care and kept at safe distance from heat.

*Sannsynlighet for hendelsen (felles for alle konsekvensområder):*      **Lite sannsynlig (2)**

*Kommentar:*

The risks connected to these gases are known, and they will be handled carefully. Instruments will also be checked for leakages before use. The probability of leakage is however still present.

**Konsekvensområde: Helse**

*Vurdert konsekvens:* **Stor (3)**

*Kommentar:* If a pressurised gas explode it can lead to large consequences.

**Risiko:**

**Farekilde: Temperature**

---

The reaction in this project is endothermic, which means that it is important to supply heat. However, some reactions are exothermic, so it is important to track the temperature during the experiments.

**Uønsket hendelse: Fire**

---

Since heat is added to the reactor there is a risk of fire if something unexpected should happen.

Sannsynlighet for hendelsen (felles for alle konsekvensområder): **Lite sannsynlig (2)**

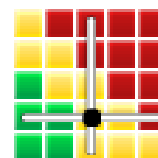
*Kommentar:*

The instruments and tubes will be checked before use, but the probability is still there.

**Konsekvensområde: Helse**

Vurdert konsekvens: **Stor (3)**

*Kommentar:* A fire in the lab could lead to large consequences as there are a lot of people and chemicals in the area.

**Risiko:****Uønsket hendelse: Explosion**

---

Heat is added to the reaction in addition to compressed gas being used. If there is a leak and explosion could happen.

Sannsynlighet for hendelsen (felles for alle konsekvensområder): **Lite sannsynlig (2)**

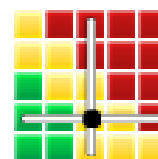
*Kommentar:*

Tubes and instruments will be checked before use.

**Konsekvensområde: Helse**

Vurdert konsekvens: **Stor (3)**

*Kommentar:* Explosion will lead to large consequences as there are a lot of people in the lab.

**Risiko:**

**Farekilde: EBSD**

Electron backscatter diffraction will be used to analyze the grain orientations of the samples.

**Uønsket hendelse: X-ray radiation**

X-rays are emitted when performing this analysis, and exposure can lead to mutation of DNA and cancer.

Sannsynlighet for hendelsen (felles for alle konsekvensområder): **Svært lite sannsynlig (1)**

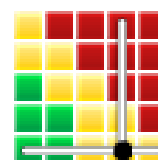
*Kommentar:*

The instrument is very safe, and exposure to X-ray radiation is highly unlikely.

**Konsekvensområde: Helse**

Vurdert konsekvens: **Svært stor (4)**

*Kommentar:* As exposure can lead to mutation of DNA and cancer, the consequence of exposure is large.

**Risiko:****Uønsket hendelse: Molding**

The samples are molded in epoxy and/or phenolic resin.

Sannsynlighet for hendelsen (felles for alle konsekvensområder): **Lite sannsynlig (2)**

*Kommentar:*

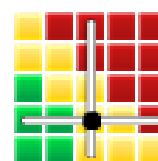
As training is required to perform the molding, it takes place in a fume hood and the risks of the chemicals are known, it is not likely that an undesired incident will occur.

**Konsekvensområde: Helse**

Vurdert konsekvens: **Stor (3)**

*Kommentar:* The epoxy is a mixture of Epofix resin and Epofix hardener. Before it hardens, it is toxic, can trigger allergic reactions and can lead to severe irritation of the eyes. The consequence of an incident can therefore be large.

The phenolic resin, PolyFast, that is used can cause an allergic reaction, and the particles can irritate airways, skin and eyes. An incident can therefore have moderate consequences.

**Risiko:**



**Uønsket hendelse: Grinding and polishing**

---

After molding, the sample is grinded and polished to obtain a flat surface.

Sannsynlighet for hendelsen (felles for alle konsekvensområder): **Lite sannsynlig (2)**

*Kommentar:*

Thorough training is performed before being allowed to use the machine. Further, a suitable disk is used and mounted precisely, loose clothing is avoided and suitable protective eyewear is used. The machine is also automatic. It is therefore not likely that an undesired incident will occur.

**Konsekvensområde: Helse**

Vurdert konsekvens: **Middels (2)**

*Kommentar:* The main risk connected to grinding and polishing is dust/particles from the disks that can be inhaled or come in contact with eyes. This can cause moderate consequences.

**Risiko:****Uønsket hendelse: Cutting epoxy**

---

A saw can be used to cut the epoxy, so that it can be placed vertically and molded again.

Sannsynlighet for hendelsen (felles for alle konsekvensområder): **Svært lite sannsynlig (1)**

*Kommentar:*

Training is performed before using the saw. In addition, cutting can not be performed before a wall, separating the saw from the user, is closed. It is therefore not likely that an undesired incident will occur.

**Konsekvensområde: Helse**

Vurdert konsekvens: **Middels (2)**

*Kommentar:* The consequence of using a saw can be large, but as the cutting proceeds under a closed wall, it is set as medium in this context.

**Risiko:**

**Uønsket hendelse: Light microscope**

---

Light microscope will be used to observe the surface of the sample after molding, grinding and polishing, to ensure that it is good enough for EBSD.

Sannsynlighet for hendelsen (felles for alle konsekvensområder):

**Svært lite sannsynlig (1)**

*Kommentar:*

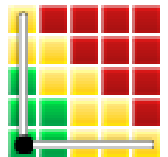
Training is required before use of the microscope. The sample is studied on a computer screen while the magnification and light is adjusted on the microscope. It is thereby a safe instrument to use, and it is unlikely that an unexpected event will occur.

**Konsekvensområde: Helse**

Vurdert konsekvens: **Liten (1)**

*Kommentar:* The consequences of an unexpected event are small, as this is a safe instrument to use. The main risk is thereby the sample, silver mounted in epoxy, which is safe to work with.

**Risiko:**



**Farekilde: Working in the lab under Covid-situation**

Lab work during the Covid-situation will bring varying risks connected to, among others, shortage of personnel and usage of common equipment.

**Uønsket hendelse: Spreading of virus**

The set-up in which the reactions will be performed is shared with a PhD-student. It is therefore important to respect the safety measurements and to keep a distance to avoid eventual spreading. The relevant characterization techniques (XRD, SEM and EBSD) are also used by several people, making it important to follow the guidelines.

Sannsynlighet for hendelsen (felles for alle konsekvensområder): **Lite sannsynlig (2)**

*Kommentar:*

It is not very likely to spread the virus as the safety measurements are known and respected. Additionally, there are restrictions regarding the number of people allowed in the labs. Personal goggles and a personal glove box will also be used.

**Konsekvensområde: Helse**

Vurdert konsekvens: **Stor (3)**

*Kommentar:* If the safety measurements are not complied, the virus can spread and lead to large consequences for the people affected by it.

**Risiko:**



## Oversikt over besluttede risikoreducerende tiltak:

Under presenteres en oversikt over risikoreducerende tiltak som skal bidra til å reduseres sannsynlighet og/eller konsekvens for uønskede hendelser.

### Detaljert oversikt over besluttede risikoreducerende tiltak med beskrivelse:



---

**Detaljert oversikt over vurdert risiko for hver farekilde/uønsket hendelse før og etter besluttede tiltak**

